The H Corona of Mars

by

Michael Scott Chaffin

B.A., Reed College, 2008

A thesis submitted to the

Faculty of the Graduate School of the

University of Colorado in partial fulfillment

of the requirements for the degree of

Doctor of Philosophy

Department of Astrophysical and Planetary Sciences

2015

This thesis entitled:
The H Corona of Mars
written by Michael Scott Chaffin
has been approved for the Department of Astrophysical and Planetary Sciences

_____

Prof. Nicholas Schneider

_____

Prof. David Brain

Date _____

The final copy of this thesis has been examined by the signatories, and we find that both the content and the form meet acceptable presentation standards of scholarly work in the above mentioned discipline.

Chaffin, Michael Scott (Ph.D., Planetary Science)

The H Corona of Mars

Thesis directed by Prof. Nicholas Schneider

The atmosphere of every planet is surrounded by a tenuous cloud of hydrogen gas, referred to as a hydrogen corona. At Mars, a substantial fraction of the H present in the corona is moving fast enough to escape the planet's gravity, permanently removing H from the Martian atmosphere. Because this H is ultimately derived from lower atmospheric water, loss of H from Mars is capable of drying and oxidizing the planet over geologic time. Understanding the processes that supply the H corona and control its escape is therefore essential for a complete understanding of the climate history of Mars and for assessing its habitability. In this thesis, I present the most complete analysis of the H corona ever attempted, surveying eight years of data gathered by the ultraviolet spectrograph SPICAM on Mars Express. Using a coupled radiative transfer and physical density model, I interpret brightness measurements of the corona in terms of escape rates of H from the planet, uncovering an order-of-magnitude variability in the H escape rate never before detected. These variations are interpreted using a completely new photochemical model of the atmosphere, demonstrating that newly discovered high altitude water vapor layers are sufficient to produce the observed variation. Finally, I present first results of the SPICAM successor instrument IUVS, an imaging ultraviolet spectrograph carried by NASA's MAVEN spacecraft. IUVS measurements are producing the most complete dataset ever gathered for the Martian H corona, enabling supply and loss processes to be assessed in more complete detail than ever before. This dataset will allow present-day loss rates to be extrapolated into the past, determining the absolute amount of water Mars has lost to space over the course of its history. Planets the size of Mars may be common throughout the universe; the work of this thesis is one step toward assessing the habitability of such planets in general.

Contents

Chapter 1

Introduction

Today the surface of Mars is extremely cold and dry, but a large and growing body of evidence indicates that the planet once had substantial liquid water at its surface. The processes that controlled the transition from a warm and wet early Mars to the planet's current state are unknown, but escape of the Martian atmosphere to space may have played a large role in driving the change.

Morphological evidence for water on early Mars is ubiquitous on the planet's surface. As early as Mariner 9 in 1972, images of sinuous channels carved into the surface hinted at the existence of flowing liquid in the planet's distant past. More recent images have revealed features similar to those deposited by terrestrial rivers, including the Eberswalde crater delta (Figure 1.1), which appears to record multiple episodes of fluvial activity, indicating that some portions of Mars had substantial flowing water at least intermittently in Martian history [Malin and Edgett, 2003].

A host of spectroscopic evidence also indicates that aqueous minerals are abundant on Mars [Ehlmann and Edwards, 2014]. Orbital infrared spectroscopy has revealed that hydrous mineral phases are prevalent on the surface (Figure 1.2). At high elevations where the atmosphere is thin and the surface free of dust, mineral phases that form in liquid water are found everywhere.

Rover-scale surface investigations performed by Spirit, Opportunity, and Curiosity also point to past aqueous environments. Spherical hematite "blueberries" indicate the action of water flowing through iron-bearing sediments (Figure 1.3). Cross-bedding found by Curiosity in outcrops at Gale crater (Figure 1.4) indicates that these rocks were deposited by ripples in a fluid. The large mineral grain sizes present in some of the layers suggest that the fluid was water.

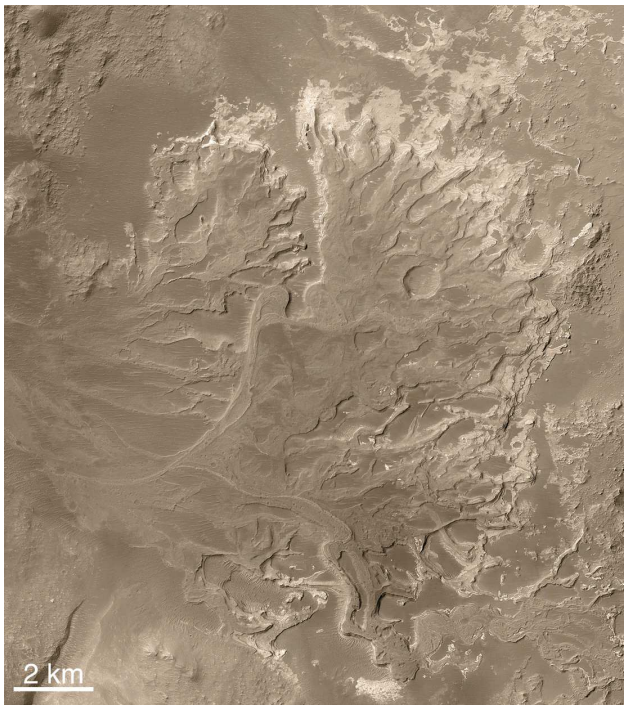

Figure 1.1: Eberswalde Crater, Mars, as imaged by Mars Global Surveyor.

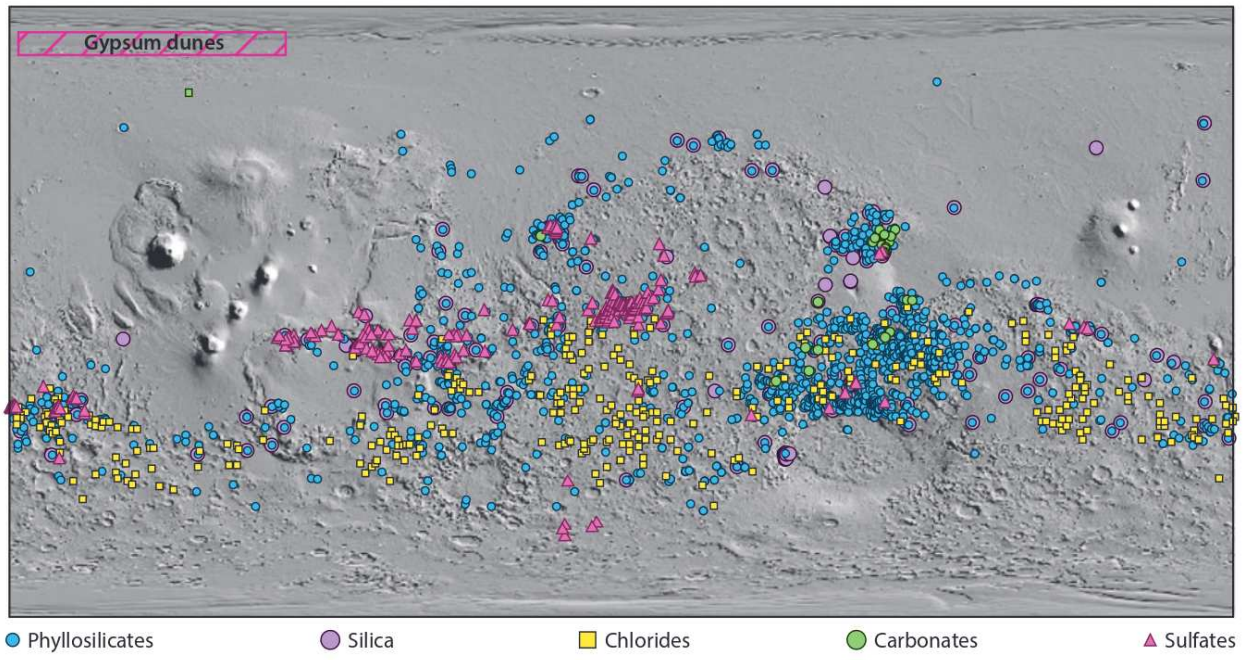

Figure 1.2: Aqueous mineral locations on the surface of Mars, from the review by Ehlmann and Edwards (2014). These minerals are identified from orbit using infrared spectroscopy. Background shows surface elevation relief map. Most identifications are at high altitudes on dust-free surfaces, where minerals are easiest to identify. This indicates that these minerals are widely distributed even where they are not detected.

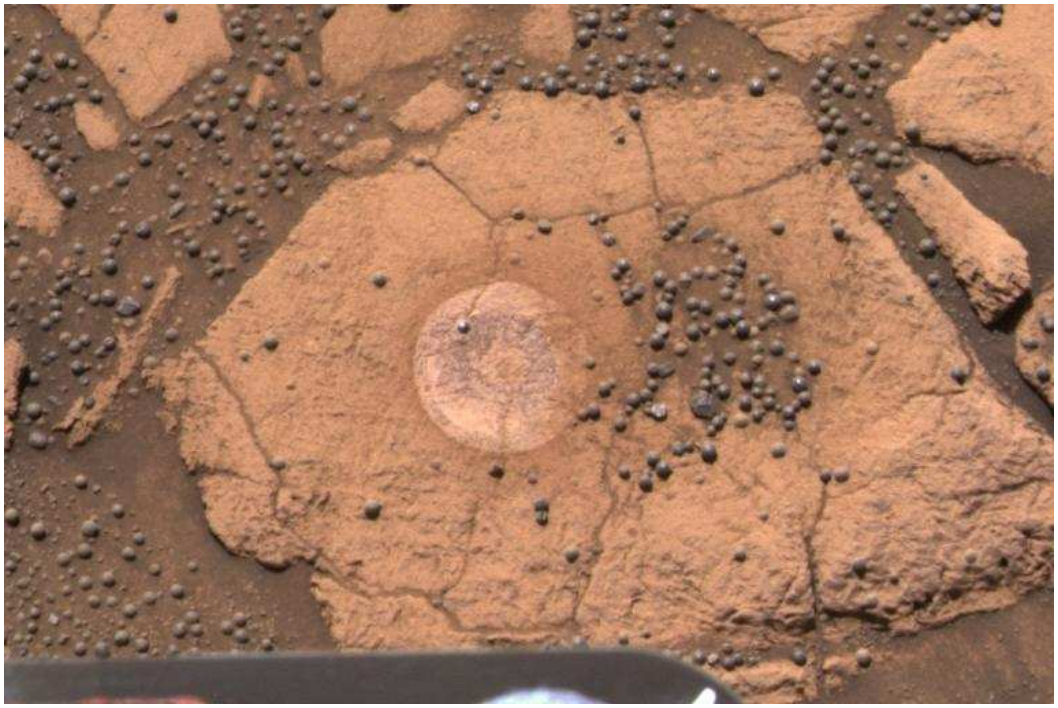

Figure 1.3: Hematite spherule "blueberries" found by the Opportunity rover. These minerals form when water flows through iron-bearing sedimentary rock.

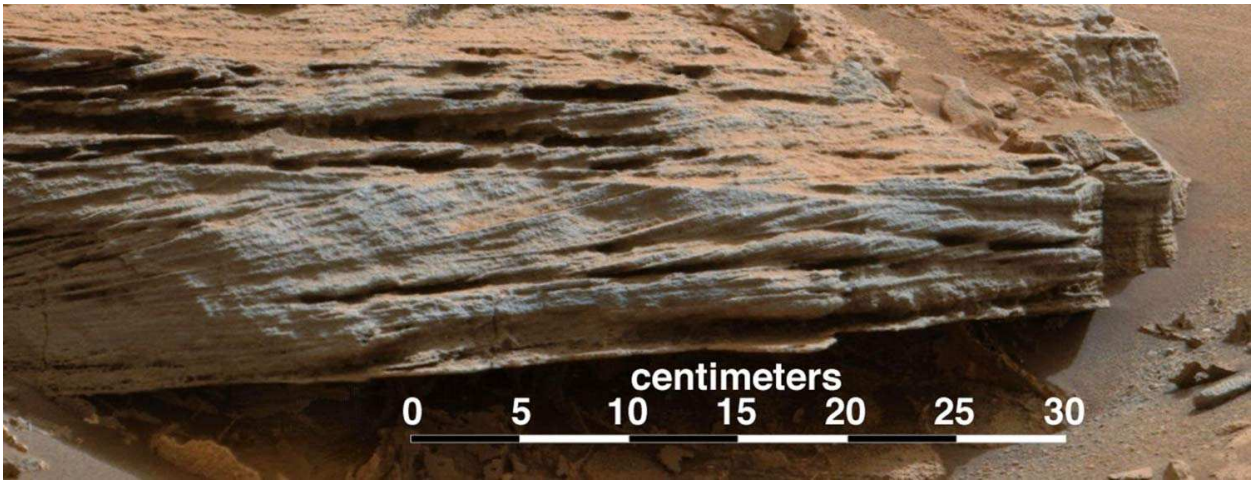

Figure 1.4: Cross-bedding in Whale Rock at Gale Crater, as imaged by the Curiousity Rover.

Evidence for surface water and near-neutral alteration conditions is almost exclusively confined to the earliest period of Martian history [Bibring et al., 2006], while today the surface is extremely arid and cold, indicating that a major change in the planet's atmosphere must have taken place (Figure 1.5). The atmospheric pressure today hovers just above the triple point of water, so that liquid is difficult to find anywhere on the planet. The thin atmosphere, composed mostly of carbon dioxide, does not provide a strong greenhouse effect, so that the average surface temperature of the planet stands nearly 60°C below zero. If the Martian atmosphere once provided sufficient pressure and warmth for liquid water to be stable at the surface, the atmosphere must have been very different in the past.

Mechanisms for so drastically changing the Martian atmosphere are debated, but fundamentally there are only two options: the early atmosphere could have been incorporated into surface minerals, or it could have left the planet altogether, escaping into interplanetary space. Potential carbonates resulting from the deposition of an early thick carbon dioxide atmosphere are difficult to inventory from orbit, because the present-day atmosphere is also made of CO_2 interfering with identification of carbonate mineral bands. While isolated carbonate features have been identified on the surface [Ehlmann et al., 2008], large deposits have eluded detection, making escape to space a plausible atmospheric sink.

The record of atmospheric loss on Mars is irrevocable: isotopic evidence gathered by landers, rovers, meteorites, and telescopic observations all indicate that the Martian atmosphere and cryosphere are enriched in the hydrogen isotope deuterium relative to the Earth and protosolar value. Some of these measurements have been compiled by Villanueva [Villanueva et al., 2015] (Figure 1.6).

The present enrichment of the heavy isotope implies that a substantial quantity of Martian hydrogen has escaped to space over the course of Martian history, differentially enriching the planet in the heavy isotope. Both the initial inventory of hydrogen and the total loss to space over Martian history are unknown.

Hydrogen lost to space is sourced from atmospheric and surface water, so that hydrogen

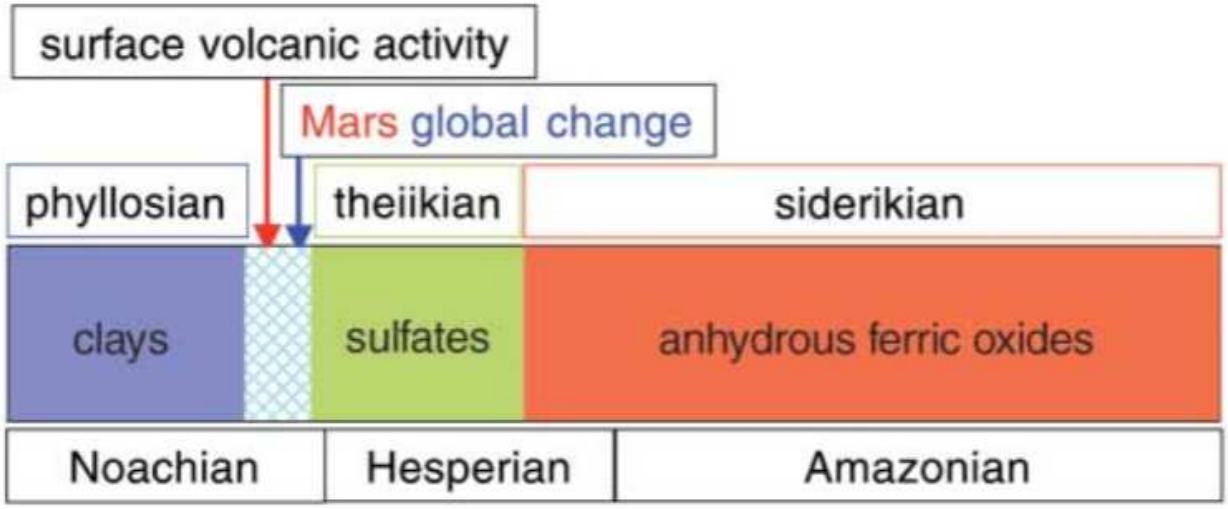

Figure 1.5: Proposed timeline of Mars surface and alteration history, from Bibring et al. (2006). Evidence for widespread surface water and mineral alteration is almost exclusively confined to the Noachian, likely more than 3.5 billion years ago. Evidence for water later in Martian history is more sporadic, indicating that a major change in the atmospheric state of the planet took place early in Martian history.

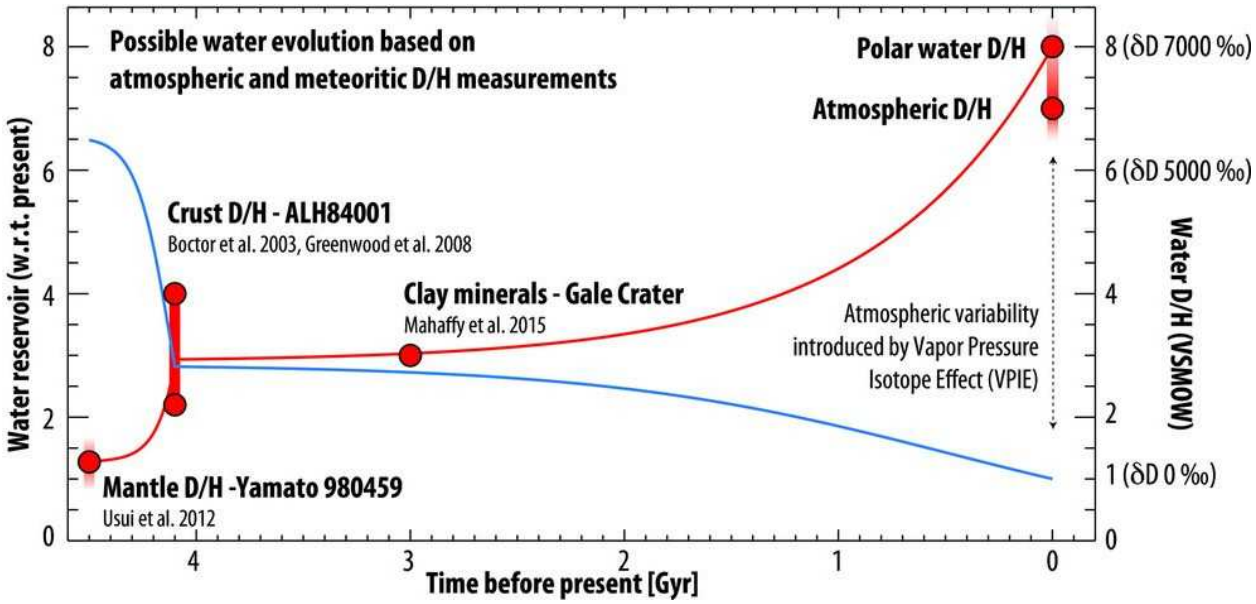

Figure 1.6: Measurements of D/H relative to Earth standard mean ocean water (VSMOW) compiled by Villanueva et al. (2015). Points indicate measured enrichment values, read on the right axis. Red curve interpolates these values, matching them to a likely history of water escape (blue curve). Monotonically increasing enrichment in the heavy isotope from the oldest samples to the present atmosphere indicates that escape of hydrogen has been significant and active throughout Martian history. This loss of H depletes the surface of water over geologic time.

escape depletes the water inventory of the planet as time passes. Despite measured isotope ratios in atmospheric water, a lack of knowledge about exchange processes between atmospheric and surface reservoirs makes the exact inventory of water on the surface of Mars today and in the past is difficult to catalog. An effort by Carr and Head [Carr and Head, 2015] using observations of current landforms and contemporary processes suggests that simultaneous O and H escape is capable of removing a large fraction of the water inventory expected to have been present on Mars at one time (Figure 1.7).

The amount of water lost to space is uncertain by at least an order of magnitude. Planetary water inventories are often measured in terms of a global equivalent layer (GEL), the depth of a liquid ocean if water were distributed evenly everywhere on the planet. Reconstructions by Villanueva et al. (2015) claim over 100 meters of loss, compared to only 4 m as a result of water loss computed in some photochemical models tuned to match observations [Yung and DeMore, 1998]. To understand the water loss history of Mars, more precise estimates of contemporary loss rates are required, coupled to a better understanding of the processes by which hydrogen is removed from the Martian atmosphere.

The work of this thesis is concerned with improving our understanding of Martian H loss, analyzing data from and constructing models of the Mars H corona, an enormous and tenuous cloud of hydrogen gas that completely envelops the planet. In the corona, where atoms experience collisions only rarely, atoms traveling with escape velocity leave the planet behind forever. H atoms reach the corona from below, where a complicated series of mechanisms active at all altitudes strips them out of water and transports them upward. Each of these mechanisms plays a role in controlling the amount of water Mars is losing via H escape today, and each may have behaved differently in the past. A better understanding of the entire chain of events leading from water to escape is required to estimate the total amount of water Mars has lost over its history.

The document is arranged as follows: First, I present a review of previous measurements of planetary H coronae, including the Mars corona and the lower atmospheric processes that are thought to control H escape. I then review the coupled physical and radiative transfer model used

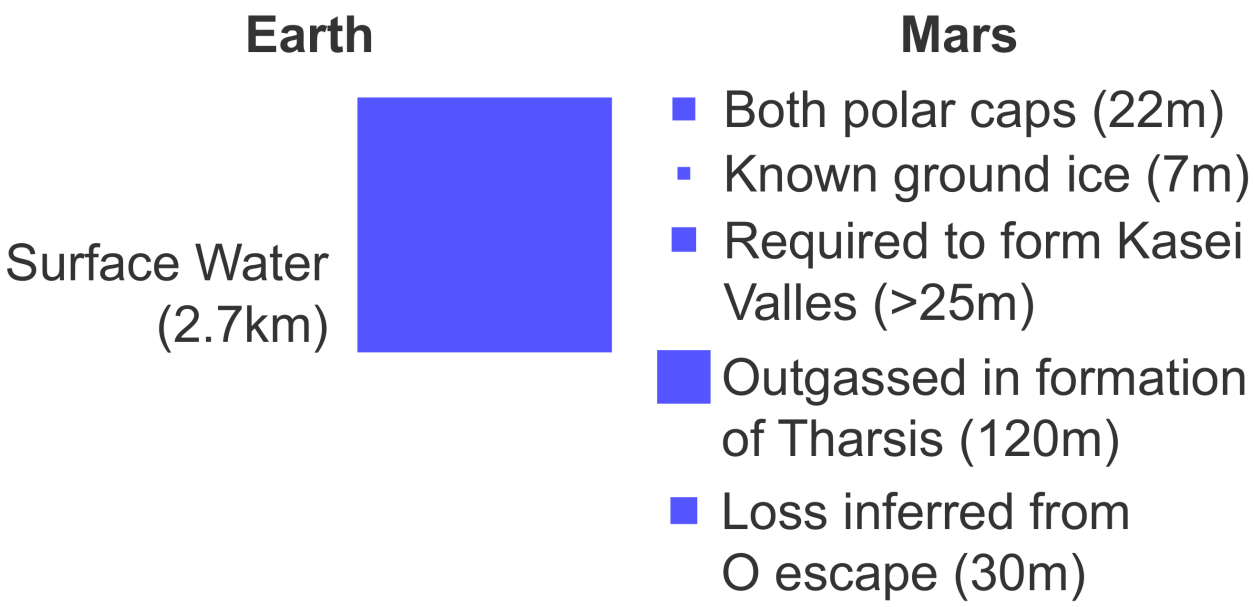

Figure 1.7: Some estimates of water inventories on Mars, relative to the Earth, from Carr and Head (2015). All values given in terms of global equivalent layer, the depth of water that would be produced if the reservoir were spread out evenly on the planet's surface.

to interpret measurements of the H corona made by spacecraft orbiting Mars. Third, I present data gathered by the Mars Express ultraviolet spectrometer SPICAM, summarizing an analysis already published of data gathered in 2007 [Chaffin et al., 2014] and analyzing data gathered over an additional four Earth years of observations, the complete usable SPICAM dataset. This analysis resulted in the discovery of an unexpected variation of coronal brightness, demonstrating that the corona and the escape rate of hydrogen is more variable than predicted. In chapter four, this variation is interpreted using a completely new photochemical model of the Mars atmosphere built for this thesis, demonstrating that recently discovered high-altitude water vapor layers can produce the escape rate variations. Finally, I present initial results from the SPICAM successor instrument IUVS, whose observations over the first four months of MAVEN's primary mission have already demonstrated that new and more sophisticated models are required to understand the H corona and Martian H escape.

Chapter 2

Background

A large portion of this thesis involves interpretation of 121.6 nm Lyman alpha sunlight scattered by hydrogen atoms in the upper atmosphere of Mars, called the corona. Ultraviolet light at this wavelength is absorbed and emitted by the most fundamental electronic transition in nature: the $2 \rightarrow 1$ jump of an electron in a hydrogen atom (Figure 2.1). Hydrogen is abundant in interplanetary space and in planetary upper atmospheres; it absorbs sunlight and re-emits it in all directions, filling the sky with a diffuse Lyman alpha glow. Around planets, H is more concentrated, creating bright coronae that decrease in intensity with altitude as hydrogen becomes less concentrated. Observing this intensity decrease provides a probe of coronal structure.

Observations of a planetary H corona can be made with telescopes positioned far from the planet or with instruments carried through the corona on orbiting spacecraft. When observing with a telescope, special filters can be constructed that pass almost exclusively Lyman alpha light, permitting a direct image of planetary emission to be made. On orbiting spacecraft, most Lyman alpha sensitive instruments are ultraviolet spectrometers, which observe a spectrum of multiple wavelengths including Lyman alpha. Many of these instruments are not equipped with imaging capability, but the orbit of the spacecraft around a planet offers an opportunity for even a point spectrometer to observe a range of altitudes over the course of a spacecraft orbit (Figure 2.2). This type of observation, called a **limb scan** or **coronal scan**, accounts for most of the data gathered about planetary coronae beyond Earth.

Typically, the term corona is intended to mean the collisionless region of a planet's extended

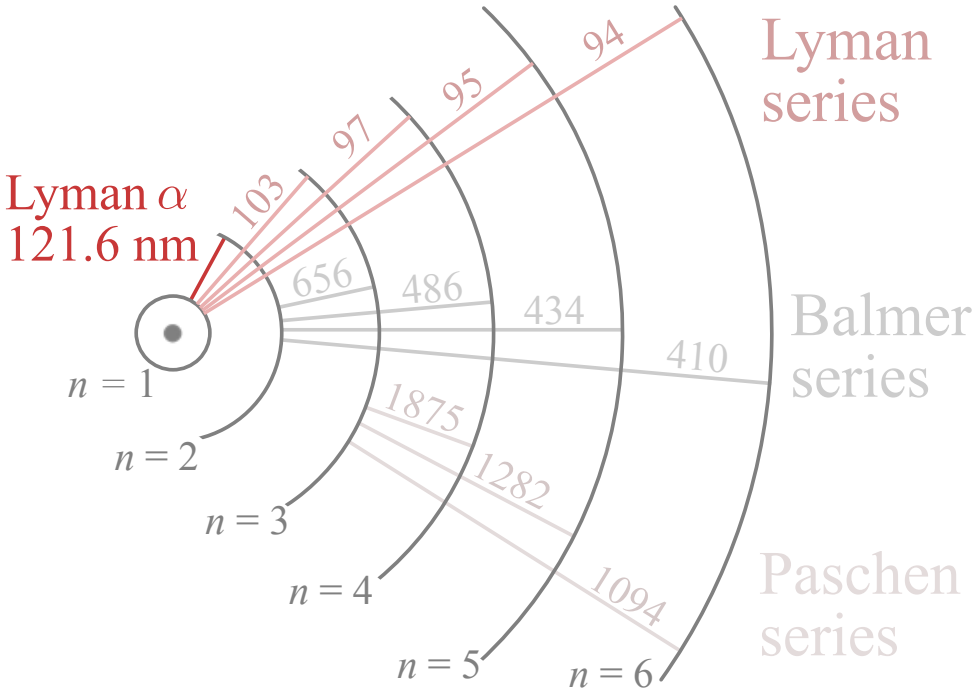

Figure 2.1: Electron transitions of the hydrogen atom, listed by wavelength in nanometers.

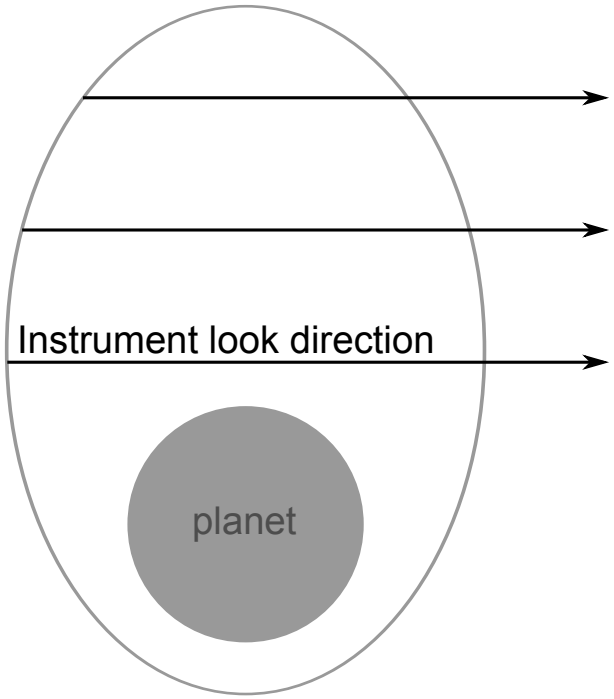

Figure 2.2: Geometry of a limb scan. An orbiting spacecraft points the instrument along a fixed direction, usually across the spacecraft orbit. Spacecraft motion carries the line of sight across a range of altitudes.

outer atmosphere, or **exosphere**, where the atmospheric density is extremely low. Particles in this region travel on ballistic trajectories, with the density structure of the corona determined by the underlying collisional atmosphere. The transition from collisional to collisionless is often approximated by introducing a fictional **exobase**, an altitude at which the atmosphere instantly transitions form completely collisional to collisionless (Figure 2.3). If we further assume that the particles at the exobase have a fixed density and Maxwellian temperature, the density of the corona and the escape flux of hydrogen being lost from the atmosphere can be analytically computed. A major portion of this thesis involves retrieving these parameters, which summarize the state of the corona, from the density and brightness profiles they produce.

The brightness of emission lines (such as Lyman alpha) in planetary atmospheres is typically measured in Rayleighs:

$$1\ \mathrm{R} = \frac{10^6}{4\pi}\frac{\mathrm{photons}}{\mathrm{cm}^2\ \mathrm{s\ sr}}.$$

The Rayleigh is a unit designed to ease conversion between intensities observed along a line of sight and omnidirectional photon emission rates from molecules or atoms in a planetary atmosphere. For emissions where scattering along the line of sight between the emitting species and the observer can be neglected, the emission is said to be **optically thin**, and the Rayleigh gives the true photon emission rate. For Lyman alpha in planetary atmospheres, scattering cannot usually be neglected; the corona is **optically thick** and the Rayleigh is a measure of apparent brighness only. Methods to deal with atmospheric scattering and retrieve densities exist: one method is detailed in Chapter 3 and used to analyze coronal brightness measurements in the remainder of the thesis.

In this chapter I present the context in which H escape at Mars is studied. I review of the discovery of planetary coronae, which begins with the first measurements gathered at Earth. I discuss the history of H corona measurements at Mars, including a summary of the processes thought to control H escape today; these processes operate in the collisional atmosphere of the planet. While it was once thought that these processes were well understood, some of the work of this thesis has called into question the canonical view of H escape at Mars. I conclude by addressing

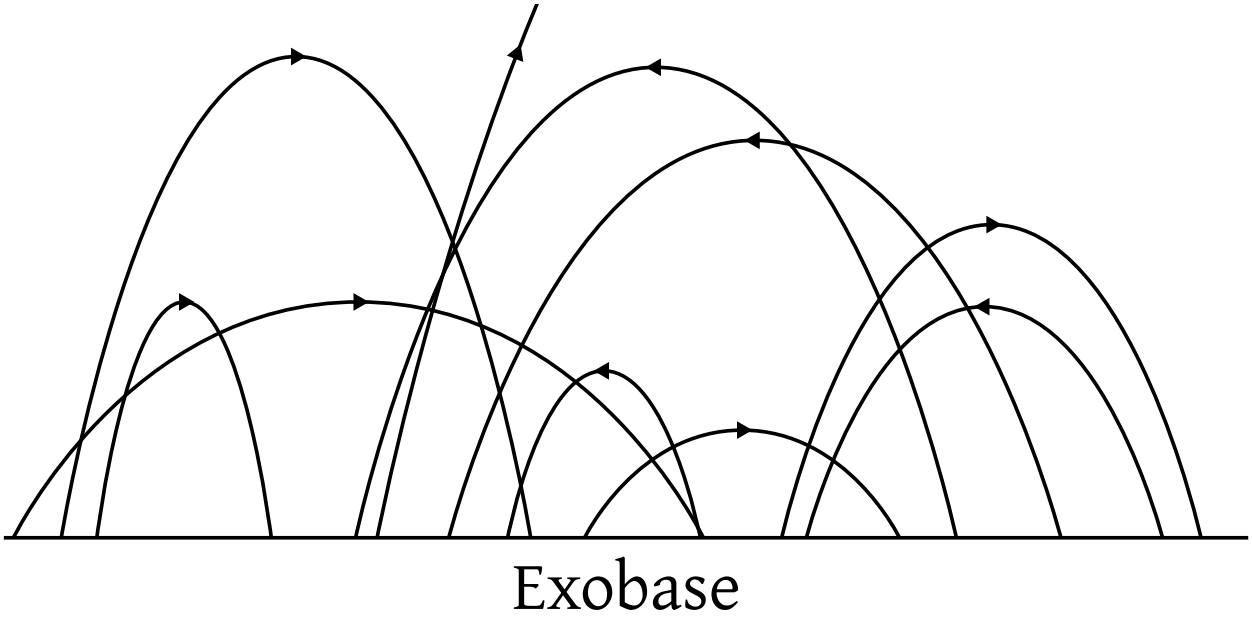

Figure 2.3: Particles departing from a fictional exobase. Above the exobase the atmosphere is assumed collisionless and particles travel along ballistic trajectories.

coronal measurements made at other terrestrial planets. H escape may operate differently at Mars than at Earth or Venus, but the situation remains unclear.

2.1 Geocoronal and interplanetary hydrogen

Diffuse light scattered by hydrogen in the Earth's upper atmosphere and interstellar medium was discovered with rocket flights in the 1950s designed to detect emission from distant stars (Figure 2.4) [Kupperian et al., 1959]. While point sources were eventually discovered in longer wavelength bands around 130 nm, sky glow at Lyman alpha prevented direct detection of starlight at 121.6 nm. The intense Lyman alpha light observed across the night sky was proposed to be due to scattering of sunlight by the extended upper atomsphere of the Earth (the geocorona) or by H atoms in the interstellar medium. Ultimately, both were determined to contribute, with the geocorona dominating the observed brightness.

Many subsequent observations of the geocorona were made, with a formal procedure for comparing these observations with modeled sky intensities developed by Thomas [Thomas, 1963]. Observations of the geocorona in scattered light were augmented by dedicated mapping missions, many of which carried cells containing a tenuous gas of hydrogen or deuterium that could be heated to differentially absorb coronal light from the core of the line outward, obtaining a measurement of coronal temperature [Fahr and Shizgal, 1983]. Perhaps the most spectacular data resulting from these investigations are images of the geocorona gathered by lunar telescopes carried on Apollo 16 (Figure 2.5) [Carruthers et al., 1976].

More recently, the hydrogen distribution in the geocorona has been measured by dual photometers on the TWINS mission [Bailey and Gruntman, 2011]. TWINS (Two Wide-angle Imaging Neutral-atom Spectrometers) studies hot populations of heavy atoms in the Earth's corona, which are typically created when an ion accelerated by electromagnetic fields collides with a hydrogen atom, resulting in a high-speed neutral atom and a proton. Both TWINS packages carry two Lyman alpha photometers. With these instruments, Zoennchen et al. have had great success in measuring the three-dimensional distribution of hydrogen in the extended outer corona more than

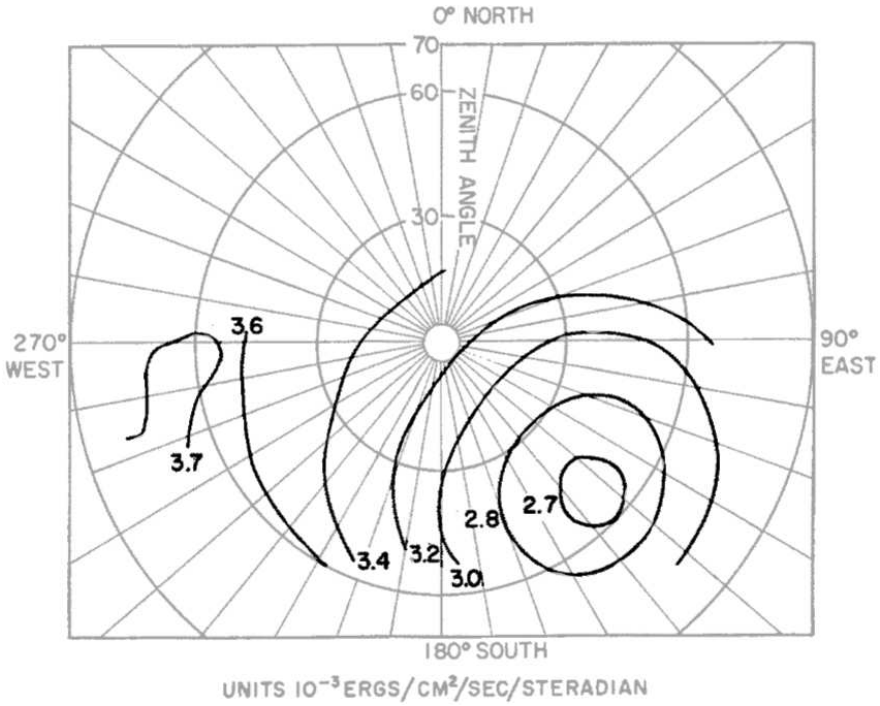

Figure 2.4: First published map of Lyman alpha sky glow, by Kupperian et al. (1959). Minimum intensity corresponds to anti-sunward direction.

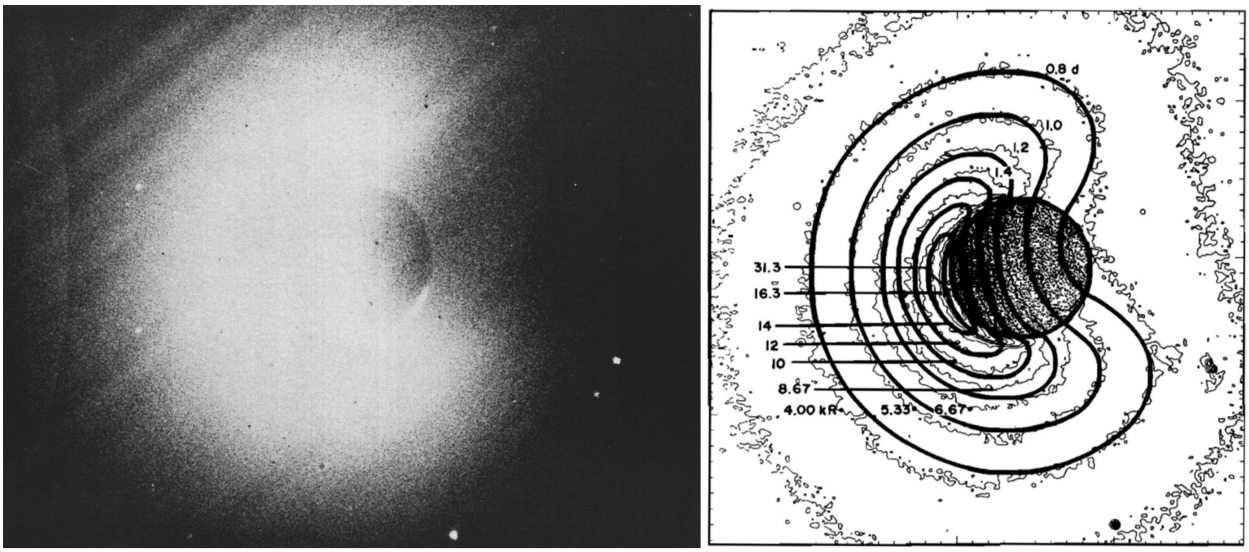

Figure 2.5: Observations of the geocorona from the moon, by Carruthers et al. (1976). (left) Unprocessed image of the geocorona in Lyman alpha light. (right) Data and model intensity isophotes (kR), including indications of film exposure density (upper right).

three Earth radii from the center of the planet, where the brightness of the corona is proportional to its density [Zoennchen et al., 2013].

Beyond the Earth's atmosphere, the entire solar system is filled with neutral hydrogen originating in the interstellar medium [Izmodenov et al., 2013]. Compared to the geocorona at > 10 kR, the interplanetary hydrogen (IPH) signal is weak (< 1 kR), but must be understood because it is always present in the background of coronal observations. Interplanetary hydrogen passes through the solar system as a result of the Sun's velocity relative to the interstellar medium, originating as a collimated flow near 253° RA, 8.7° Dec with a heliocentric velocity of ≈ 20 km s^{-1}. On their way through the solar system, these H atoms are only slightly deflected by the Sun's gravity, because solar radiation pressure at Lyman alpha almost perfectly cancels the gravitational attraction. H atoms occasionally collide with solar wind protons, resulting in ionization and a depletion in sky intensities on the downwind side of the flow.

Because the interplanetary line is broad and can be Doppler shifted with respect to planetary coronal lines, it is inevitably observed as a background in observations of the H corona. To determine the brightness of the corona and properties of the planet rather than the IPH, this background must be subtracted with dedicated observations or accurate models. Since its discovery the IPH has been well-studied, with comprehensive maps provided by the Solar Wind Anisotropy (SWAN) instrument on NASA's Solar and Heliophysics Observatory (SOHO) [Bertaux et al., 1995]. In addition, the MESSENGER spacecraft observed the entire sky on its cruise to Mercury [Pryor et al., 2013], enabling the production of an all-sky maps (Figure 2.6).

Such detailed observations have enabled the development of robust models for the IPH intensity as observed along an arbitrary line of sight. One such model is used for subtracting the IPH underlying measurements analyzed in this thesis, as described in Chapter 3.

2.2 Historical measurements of Mars H escape

The story at Mars begins with measurements by Mariner 6 and 7, which made the first ultraviolet observations of the Martian upper atmosphere [Barth et al., 1971]. These observations

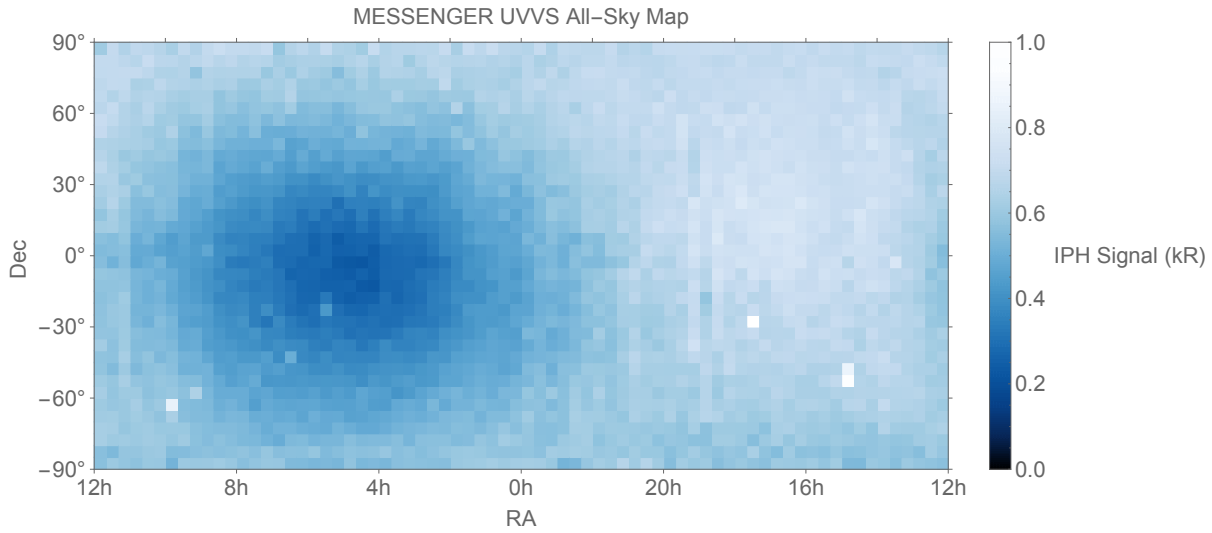

Figure 2.6: All-sky map from MESSENGER Data, using data reported in Pryor et al. (2013). The IPH is brightest in the upwind direction, and diminishes uniformly toward the opposite side of the sky. Point sources visible in this image are mostly UV-bright stars aligned with the galactic plane.

revealed the now well known ionospheric spectrum of this CO_2-dominated atmosphere (Figure 2.7), including the signature of H in the ionosphere and corona resulting from the breakdown of more complex hydrogen-bearing species.

Mariner 6 and 7 were flybys, so thet data from each mission was limited to a single coronal profile. These observations detected the H corona to planetocentric distances of 30,000 km and gathering Lyman alpha data from the IPH to distances of 60,000 km (Figure 2.8). Analysis of these two profiles [Anderson and Hord, 1971, 1972] retrieved an exobase density at 250 km of $3 \pm 1 \times 10^4$ cm^{-3} and a temperature of 350 ± 100 K, implying an exobase escape flux of 1.8×10^8 cm^{-2} s^{-1}.

The Mariner 9 orbiter returned much more data on the corona, but analysis of the 121.6 nm data by Anderson [Anderson, 1974] focused on constraining the H population in the region below 250 km altitude, often called the **thermosphere**. This analysis did not replicate or extend the earlier work on H escape for the entire Mariner 9 dataset, perhaps owing to early suggestions that the Lyman alpha brightness at Mars was more constant than expected [Barth et al., 1972]. However, in Mariner 9 measurements coronal brightness varies by more than 25% (Figure 2.9).

The optically thick nature of the H corona implies that these variations in brightness are linked to much larger variations in the exospheric H inventory, but no detailed analysis of these variations has ever been performed. One reason for this omission may be theoretical work nearly simultaneous with the observations, explaining the low abundance of CO and O_2 in the Martian atmosphere. These models of Martian photochemistry predicted that the source of coronal H was long-lived molecular hydrogen, and that large variations on a seasonal timescale were unlikely [McElroy, 1972, Parkinson and Hunten, 1972]. This robust theoretical result may have biased observers away from searches for time-variability. Work performed for this thesis has demonstrated seasonal variability in the Mars corona (see Chapter 4), contradicting the model prediction.

Early soviet missions to Mars also measured H Lyman alpha. The first, Mars 3, obtained an altitude profile of Lyman alpha brightness using a multichannel photometer [Dementyeva et al., 1972]. Fixing the hydrogen temperature to that measured by Mariner, Mars 3 obtained density lower by a factor of five than that measured by the earlier mission. Initially, this was interpreted

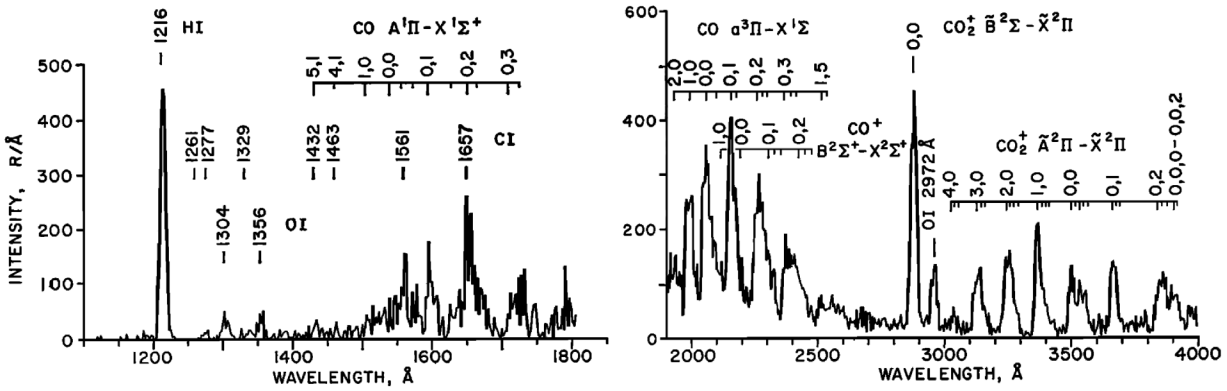

Figure 2.7: Discovery of the ultraviolet airglow of Mars, reported by Barth et al. (1971). Most of the spectrum is dominated by emissions from the breakdown products of CO_2, but in the far-ultraviolet at the shortest wavelengths hydrogen Lyman alpha is present at 121.6 nm (1216 Å).

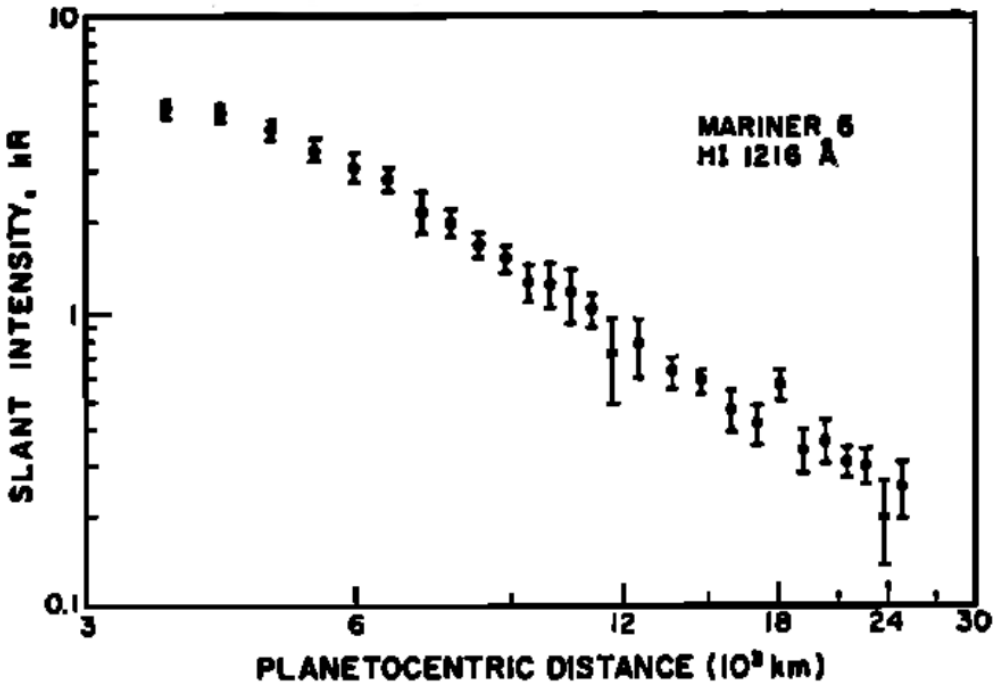

Figure 2.8: Mariner 6 altitude profile of Lyman α intensity.

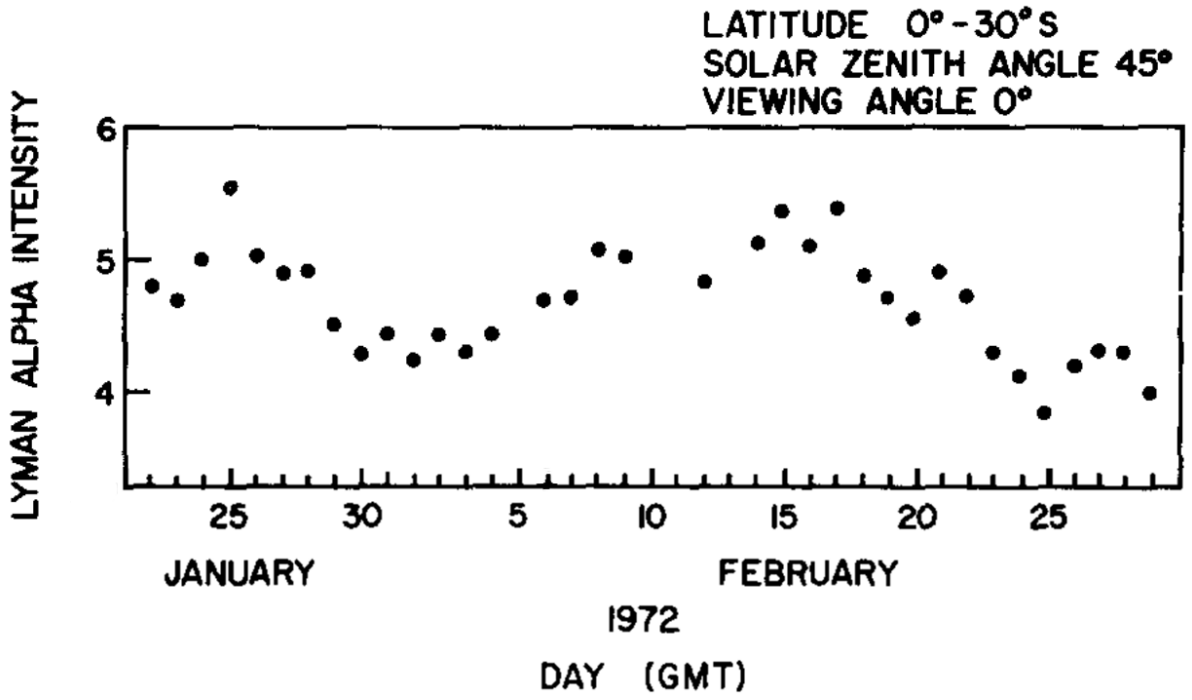

Figure 2.9: Mariner 9 variations in Lyman alpha brightness from Barth et al. (1972). The brightness of the atmosphere (measured in kR) varies by 25% over the two months of measurement.

as evidence of a drastic change in the H inventory of the exosphere, provisionally ascribed to changes in the water mixing ratio in the lower atomsphere. This interpretation was challenged by the complete dataset provided by Mariner 6, 7, and 9, which observed much smaller variation in H intensity profiles in a time interval bracketing the Mars 3 observations. A consensus emerged that a difference in the absolute calibration of the instruments was responsible for the difference in derived densities [Moroz, 1976]. Subsequent to intercalibration, an independent analysis of the Mars 2, 3, and 5 data found temperatures and densities comparable to those found by Mariner. In addition to photometers, Mars 5 and 7 carried Lyman alpha H and D absorption cells capable of measuring the width of the line and therefore the temperature of the atmosphere. The only result for Mars is a single absorption cell profile from Mars 5, published by Babichenko [Babichenko et al., 1977], who obtained an H temperature through cell absorption of the core of the Mars H line consistent with that reported by Mariner, 350 ± 20 K. The early failure of Mars 5 (possibly due to a micrometeorite impact during orbit insertion) prevented any further results from this instrument [Siddiqi and Launius, 2002].

From 1974 to 2005, no missions to Mars observed the H corona. Prior to the launch of the Hubble Space Telescope, the observational capability of Earth-orbiting ultraviolet telescopes was limited. A spatially unresolved measurement of Mars Lyman alpha was obtained with the Copernicus telescope [Levine et al., 1978], but a lack of altitude-dependent intensities forced the authors to rely on assumptions about the hydrogen temperature at Mars. Analysis of the data determined that a Viking descent temperature of 170 K and a number density of 1.8×10^5 cm^{-3} were consistent with the observations. The reported density is roughly sixty times that reported by Mariner, which the authors interpreted as a large density build-up at solar minimum conditions. Observations at solar minimum by SPICAM, discussed below, found densities and temperatures similar to Mariner observations, calling this interpretation into question.

Spatially resolved high resolution ultraviolet spectroscopy of the atmosphere of Mars was made possible when the Hubble Space Telescope (HST) came on-line in 1994. HST carries two systems especially useful for observing hydrogen at Mars: a high-resolution echelle channel that

can separate hydrogen Lyman alpha from the isotopically shifted deuterium line, and a solar-blind imaging channel with a dedicated Lyman alpha filter. HST observations of Mars sensitive to Lyman alpha were approved in Cycle 1 (GO 2393), 6 (GO 6760), 9 (GO 8658), 16 (GO 11170), 19 (GO 12538), 21 (GO/DD 13632), and 22 (GO 13794), often for the purpose of measuring Mars D/H. HST observations from 2007 (cycle 16) were gathered and later analyzed as part of an observation campaign simultaneous with observations and analysis of the corona by SPICAM (discussed in Chapter 4). These observations resulted in three images of the corona separated by two week intervals in Fall 2007 (Figure 2.10) [Clarke et al., 2014].

Three Lyman alpha profiles were extracted from these images, resulting in estimates of atmospheric escape similar to Mariner results and contemperaneous with the measurements made by SPICAM discussed in chapter 4. Data from the remaining HST cycles has not been used to produce published constraints on the Mars H corona, perhaps because observations of the Mars H corona from near Earth orbit must overcome the difficulty of observing Mars H through the geocorona.

From 2005 onward, the H corona and upper atmosphere of Mars has been investigated with the ultraviolet channel of SPICAM (Spectroscopy for the Investigation of the Characteristics of the Atmosphere of Mars), on the European Space Agency's Mars Express mission. Initial analysis of the H corona with SPICAM was performed by Chaufray [Chaufray et al., 2008], who analyzed seven coronal observations gathered across 2005 and 2006, finding results consistent with Mariner. A single profile analyzed required a two component hydrogen distribution to obtain a satisfactory fit to the data (Figure 2.11). The two components found by Chaufray include a hydrogen population assumed to be in equilibrium with the CO_2 atmosphere at 200 K and much hotter (> 500 K) nonthermal hydrogen component of unknown origin. This profile is the only one in the entire SPICAM dataset requiring a two-component model for a satisfactory fit. Expanding the seven profiles studied by Chaufray, a major portion of this thesis involves the analysis of the remaining SPICAM data, covering the period 2005-2010.

The charged particle instrument ASPERA[1], also on MEX, is senstive not only to particles

[1]ASPERA stands for Analyzer of Space Plasma and EneRgetic Atoms.

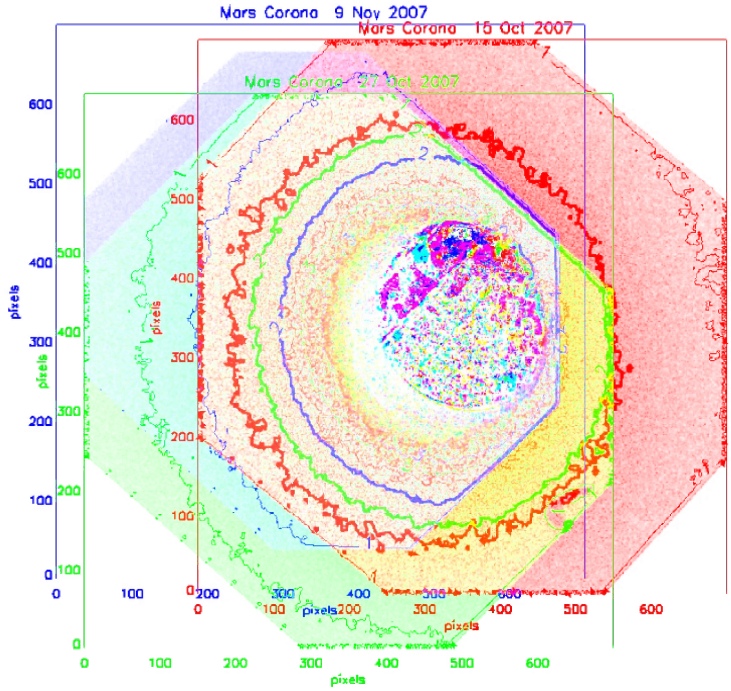

Figure 2.10: Observation of the Mars H corona using the Hubble Space Telescope on three dates in Fall 2007, reported on by Clarke et al. (2014). Each image has been colorized into three channels identified by date at the top of the figure. Contours show lines of constant brightness. The thick 2 kR contour (labeled in the blue and green channel) indicates that the corona of Mars contracted over the imaging period, a result independently indicated by SPICAM data gathered at Mars.

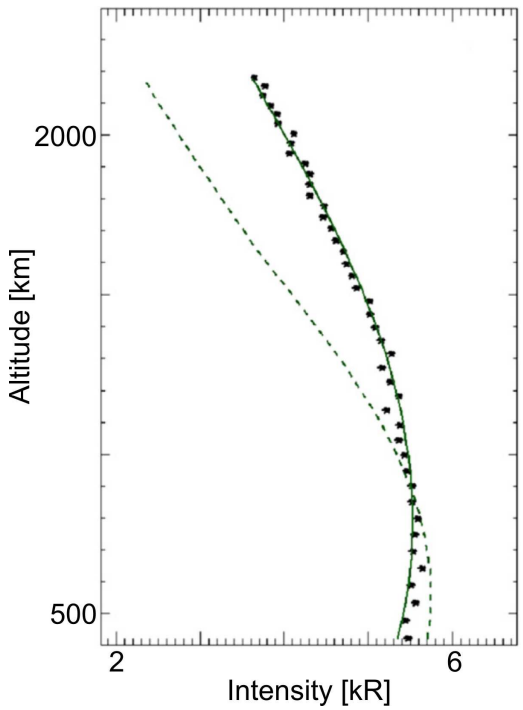

Figure 2.11: Profile requiring a two component model from Chaufray et al. (2008). The data (black points) are not well fit by a hydrogen temperature of 200 K (dashed line), preferring a population including hot hydrogen with $T > 500$ K (solid line).

but also to ultraviolet light shorter than 160 nm [Galli et al., 2006]. Ultraviolet light calibration of the instrument was performed during cruise using SWAN maps of the IPH and sky UV brightness shorter than 180 nm. On orbit around Mars, the instrument performed a coronal scan, reporting calibrated intensities a factor of 3-8 lower in brightness than all other measurements made at the altitudes observed. The 220 km exobase density and temperature resulting from the measurement and inversion are 10^4 cm^{-3} and 600 K, a departure from the Mariner values interpreted as a change in the corona. In performing their analysis, however, the authors assumed that the corona was optically thin and that multiple scattering could be ignored at their observation altitude of $>$ 2000 km. Multiple scattering at Lyman alpha is important in the Mars corona to large planetary distances, dominating the observed radiance. Large optical depths inflate intensity scale heights; ASPERA analysis assuming an optically thin profile likely resulted in an overestimate of the coronal temperature. In addition, without simultaneous observations by an instrument designed to detect ultraviolet light, it is unclear whether the instrument was improperly calibrated or the corona was really different at these times.

During its Mars flyby in 2007, Rosetta's ALICE instrument made observations of the Mars H corona (Figure 2.12) [Feldman et al., 2011]. These observations were made before closest approach using two offset pointings across the dayside limb. In contrast to Chaufray's analysis with MEX, the authors found no evidence for a hot H component in their observations. Interpretation of the measurements fixed the 200km exobase temperature to 200 K, finding that for the optically thin Lyman β line at 102.6 nm and the optically thin portion of the Lyman α are best fit by a density of 2.5×10^5 cm^{-3}, much larger than the Mariner density at a much lower temperature. The observation is notable for the low intensities observed across the dayside limb, peaking at just over 2 kR, compared with Mariner 6 values more than twice as bright. The authors note that these low intensities may result from measurements made at the minimum of the solar cycle or from difficulties in the calibration of the instrument, as Lyman alpha unintentionally fell on a boundary between the coated (i.e. signal-multiplying) and bare detector photocathode, making absolute calibration challenging.

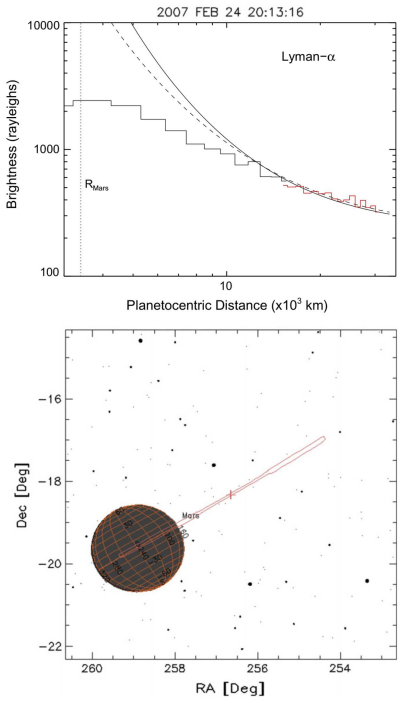

Figure 2.12: Rosetta detection of atmospheric H from Feldman et al. (2011). (top) Detected Lyman alpha intensity as a function of planetocentric distance, including a fit to the red bins at high altitude where multiple scattering is negligible. (bottom) Geometry of the observations during the Mars flyby, showing the illuminated disk (orange grid) and the location of the slit on the sky (red).

Currently operating at Mars, the Indian Space Research Organization's Mars Orbiter Mission has a Lyman alpha photometer with D and H absorption cells. No data from this instrument has been released, and the instrument status is unknown.

Given the sparse nature and systematics present in the measurements made before 2014, measurements made by MAVEN's Imaging Ultraviolet Spectrograph (IUVS), discussed in Chapter 6, have the potential to greatly increase our understanding of the processes that form the Mars H corona. Through a series of complementary and high cadence measurements of the H corona IUVS will produce a coherent dataset sampled at a sixteen hour cadence across at least one Earth year. For the first time, this extensive dataset will allow development of an understanding of the H corona beyond that provided by the existing intermittent data.

2.3 Sources of escaping H: the odd hydrogen cycle

Hydrogen in the corona of Mars has its source in lower regions of the atmosphere. A diagram illustrating some of the important processes leading to H escape is given in Figure 2.13, which serves as a guide to the discussion in this section.

The chemistry of hydrogen production at Mars begins with water near the surface. Early investigations of the chemical composition of the Mars atmosphere, reviewed by Donahue [Donahue, 1971], revealed that its oxygen abundance is much lower than expected based on the ease of CO_2 photodissociation. Further, the ratio of CO to O_2 atmospheric concentrations is 1:2, rather than the 2:1 ratio expected from stoichometric photodissociation. The explanation for these puzzling observations was provided by McElroy [McElroy, 1972], who suggested that photodissociation products of water could act as catalyts for CO_2 recombination.

The catalytic photochemistry of water dissociation products is called the odd-hydrogen cycle (Figure 2.14). Because the atmosphere of Mars is thin, UV light can penetrate to the near-surface atmosphere, splitting H_2O into H and OH. OH reacts with CO to recombine CO2 directly. In a three-body reaction, H scavenges O_2 and produces HO_2, the hydroperoxyl radical. This radical

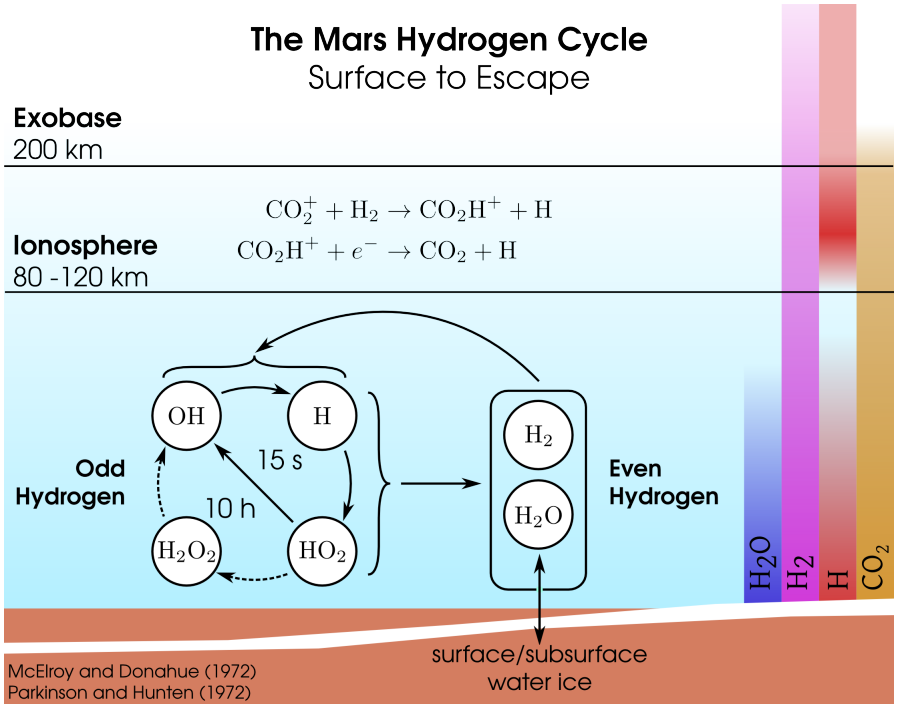

Figure 2.13: Overview of the Mars hydrogen cycle, from surface to escape. Hydrogen escape is the result of a series of processes originating near the surface and extending throughout the atmosphere.

combines with free atmospheric O, producing O_2 and OH. The net effect is:

$$\begin{aligned} CO + OH &\rightarrow CO_2 + H \\ H + O_2 + M &\rightarrow HO_2 + M \\ O + HO_2 &\rightarrow O_2 + OH \\ \hline CO + O &\rightarrow CO_2. \end{aligned}$$

The longest step in this sequence is the third, in which HO_2 is consumed. Reaction of two HO_2 molecules in the atmosphere occasionally produces peroxide, which can oxidize the surface or generate OH via photodissociation.

The atomic hydrogen produced as a result of water photodissociation is quickly consumed in the lower atmosphere. The result is that atomic H in the lower atmosphere of Mars is closely correlated with the presence of water. Low temperatures at high altitude in the atmosphere are thought to freeze out water vapor before it reaches the upper atmosphere [Clancy and Nair, 1996]; atomic H produced from water photolysis is therfore confined to the lower atmosphere. H on the escape pathway to space must reach the upper atmosphere via a species other than H_2O.

Even hydrogen species are produced via recombination of odd H, principally via the reaction of H and HO_2, which produces both water and molecular hydrogen. Photochemical models of the atmosphere result in large amounts of H_2, so that the time required to consume or produce the entire atmospheric reservoir is measured in decades or centuries. Because molecular hydrogen is both light and volatile, it is well-mixed in the atmosphere at even the highest altitudes, and is predicted to be present in abundance in the ionosphere. These model predictions have been verified exactly once, as molecular hydrogen is extremely difficult to detect spectroscopically. Krasnopolsky and Feldman [Krasnopolsky and Feldman, 2001] needed over five hours of observing time with the Far Ultraviolet Spectroscopic Explorer (effective area 20 cm^2, resolving power $\lambda/\Delta\lambda \approx 20,000$) to obtain the only detection ever made of this species in the atmosphere of Mars.

In the ionosphere, molecular hydrogen is attacked by ionospheric species, including the CO_2^+

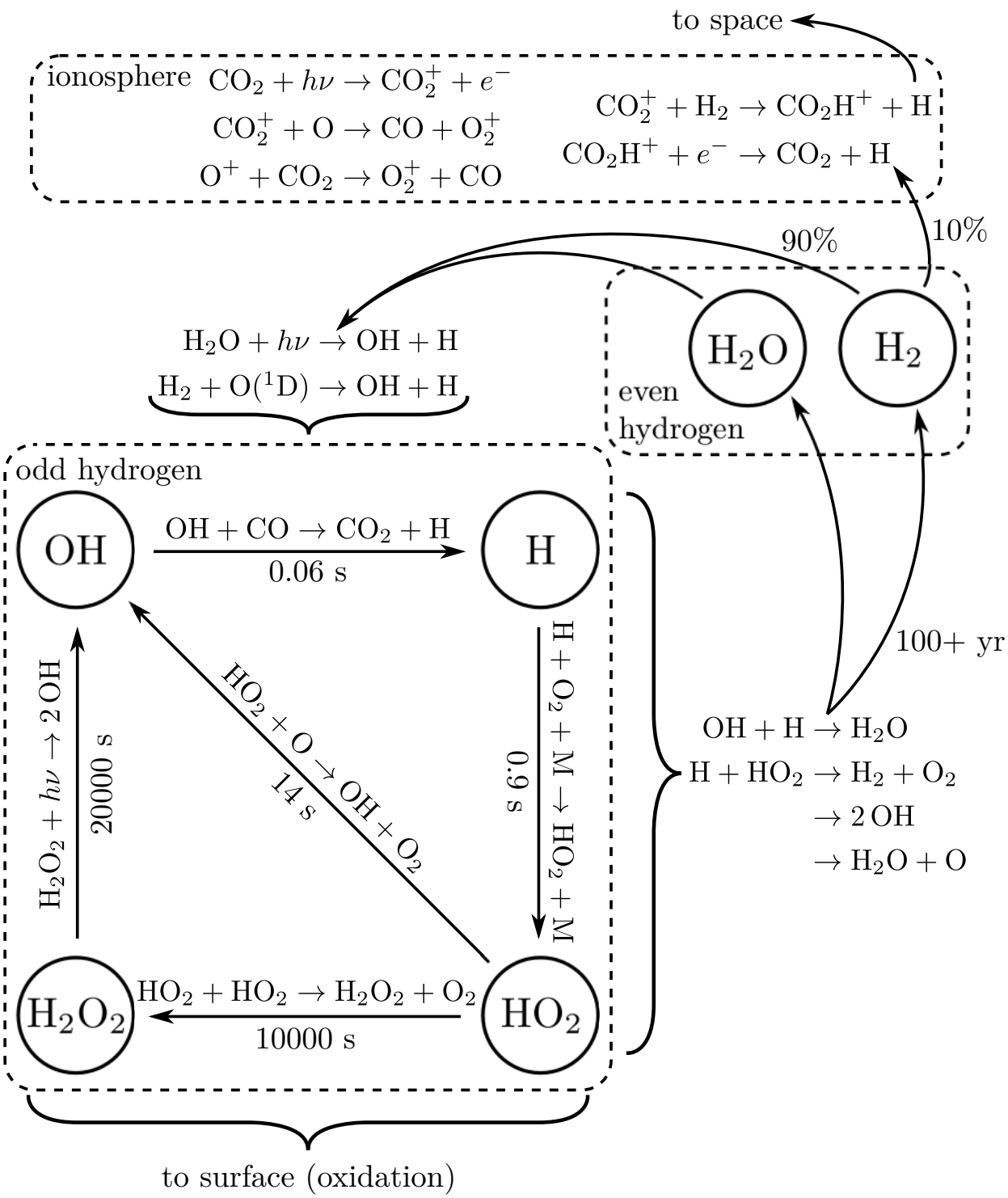

Figure 2.14: Odd-hydrogen chemistry of the Mars atmosphere.

ion and the excited O(^{1}D) state of atomic oxygen, producing atomic hydrogen in the upper atmosphere. Much of this hydrogen recombines, but some diffuses upward against the background atmosphere of carbon dioxide and oxygen until it reaches the exobase. With molecular hydrogen as a long-lived buffer on the ionospheric production of H, only upper atmospheric processes affecting the availability of CO_2^+ ions, the atomic recombination rates, and the ease of diffusion to the escape region can affect H escape rates. These parameters all vary with the thermospheric temperature, which is controlled by the ultraviolet flux of the Sun. Over the course of a Mars year, the temperature in the thermosphere can vary substantially due to the eccentricity of the planet's orbit; the effects of this have been modeled by Krasnopolsky [Krasnopolsky, 2002, 2006] and Chaufray [Chaufray et al., 2015], indicating that changes in H escape are expected to be smaller than a factor of ten.

If molecular hydrogen produced as a byproduct of the odd hydrogen cycle is the major source of escaping atomic H, its escape rate is fixed to twice the escape rate of O over geologic time, with the net result that water escapes from the atmosphere. This scheme for the self-regulated stoichiometric escape was first explored by McElroy and Donahue [McElroy and Donahue, 1972] and Parkinson and Hunten [Parkinson and Hunten, 1972], and later in greater detail by Liu and Donahue [Liu and Donahue, 1976]. H escapes from the atmosphere quickly because it is light, but O is too heavy to escape with its thermal velocity alone. Non-thermal (or "hot") O is produced in the ionosphere by the dissociative recombination reaction

$$O_2^+ + e^- \rightarrow O^* + O^*,$$

which yields energetic oxygen atoms that in some cases have sufficient energy to escape the planet.

The concentration of O_2 in the atmosphere is regulated by the differential escape of hydrogen and oxygen. Because both escaping species are sourced from water, an excess of H escape allows O to build up in the atmosphere in atomic and subsequently molecular form. In the odd-hydrogen reaction scheme, the concentration of H and thus the production rate of H_2 is controlled by the concentration of O_2 in the atmosphere. With more molecular oxygen, atomic hydrogen is more

easily converted to HO_2, with a corresponding decrease in the production of molecular hydrogen. On a timescale of 10^5 years, less H_2 is available in the atmosphere and less H escapes. The process also works in reverse, so that an excess of either H or O escape diminishes with time and H escapes at exactly twice the rate of O_2.

With H_2 as a strong molecular buffer on the escape rate of atomic H, the escape flux on short timescales is controlled by the processes that transport H to the escape region. If the processes operating to remove particles from the corona are fast relative to the transport of hydrogen into the corona, the escape rate is limited by the supply of hydrogen from below and is referred to as **diffusion-limited** [Hunten, 1973]. Escape rates in the diffusion limit are controlled solely by the availability of hydrogen bearing species in the thermosphere and the speed with which these species are transported upward by molecular diffusion. An increase in coronal temperature does not always result in increased escape rates; if the escape mechanism is already removing gas as fast as the thermosphere is supplying it, the escape rate cannot increase above the supply. If molecular hydrogen is the major bearer of H to the escape region, the limit on escape is set by the mixing ratio of H_2 at the base of the thermosphere in the well-mixed atmosphere. Using the mixing ratio measured by Krasnopolsky and Feldman, a study led by Zahnle [Zahnle et al., 2008] determined that the maximum escape flux possible from the atmosphere is 3.7×10^8 atoms cm^{-2} s^{-1} (Figure 2.15). This value is about twice the Mariner determined escape rate.

Stoichiometric diffusion limited escape is theoretically predicted but has yet to be verified with observations. The balance of escape is only maintained if molecular hydrogen is the dominant carrier of hydrogen into the upper atmosphere. In addition, measured and predicted rates of escape for H and O do not match unless there is a significant additional source of O escape, as pointed out by Fox [Fox, 1993].

The question of whether the Mars atmosphere behaves as the models predict is far from settled. The original problem the odd-hydrogen chemistry was invoked to solve was the stability of the CO_2 atmosphere, with correspondingly low abundances of CO and O_2, which have an observed 1:2 concentration ratio in the atmosphere. Models incorporating this chemistry suppress the molecular

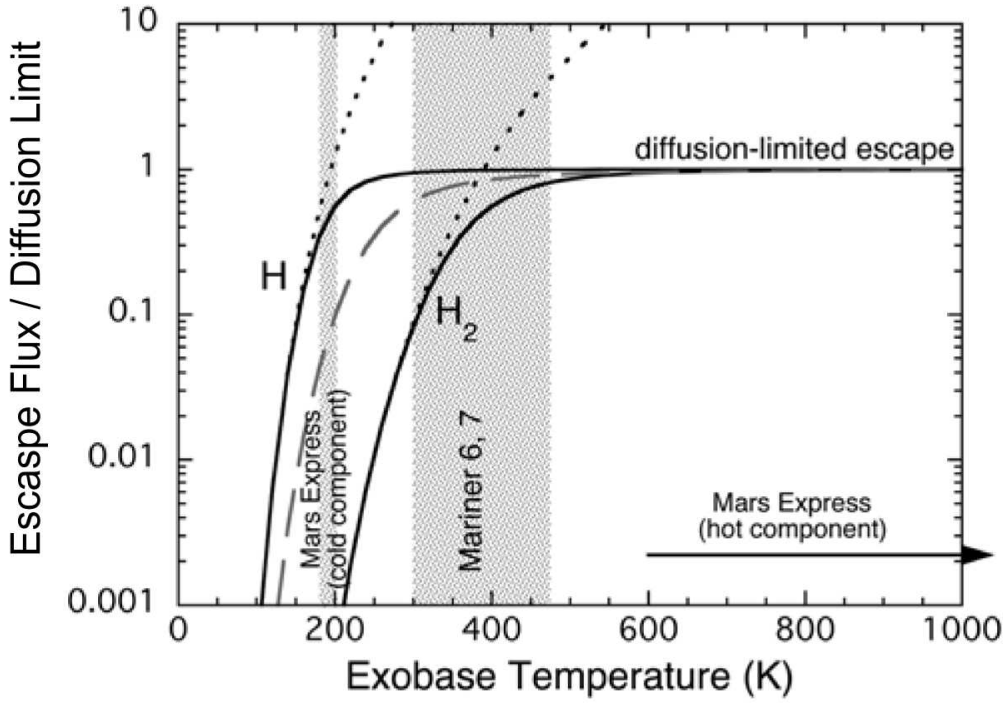

Figure 2.15: Diffusion-limited escape calculation of Zahnle et al. (2008). Solid curves indicate escape flux of H and H_2 relative to the diffusion limit, assuming that hydrogen escapes exclusively via each species. Dashed line shows an intermediate case of 50% conversion of H_2 to H in the thermosphere before escape. Dotted lines show uncorrected Jeans escape not accounting for the limited supply of H from the lower atmosphere. Shading indicates some spacecraft observations.

oxygen and carbon dioxide abundance too well, resulting in a 1:10 concentration ratio in many models. This oversuppression represents the largest unsolved problem in the photochemistry of the Mars atmosphere [Krasnopolsky, 2010].

2.4 H escape at other planets: is Mars different?

The combination of low gravity and relatively high water abundance make the Mars H corona unique among the terrestrial planets. Abundant water supplies a large amount of atomic H to the corona, where it is only weakly bound by the planet's gravity, producing an extremely extended H corona. The large extent of this corona could mask effects seen more easily at the other planets.

At Venus, analysis of the H corona using the Mariner 5 ultraviolet spectrometer revealed an H distribution with two characteristic slopes, later interpreted as a tightly bound thermal corona surrounded by an extended hot component (Figure 2.16) [Anderson, 1976].
The hot corona was interpreted as resulting from charge exchange between the solar wind and Venusian H atoms, an interpretation supported by data from subsequent missions measuring Venusian H, including Mariner 10 [Takacs et al., 1980], Venera 9 and 10 [Bertaux et al., 1978], Pioneer Venus [Cravens et al., 1980], and Venus Express [Chaufray et al., 2012]. The escape rate implied by the presence of the hot component is much greater than that from thermal escape alone, so that most H escape from Venus is nonthermal [Shizgal and Arkos, 1996].

At Earth, thermospheric and coronal temperatures are much higher than they are at Venus or Mars, but thermal H escape still accounts for only about 25% of the total [Yung et al., 1989]. The remainder is accounted for by charge exchange and polar wind acceleration of protons into the magnetotail. At high latitudes, the polar wind is more effective than charge exchange, but charge exchange makes up the majority of non-thermal escape from the Earth.

Mars may be the only terrestrial planet in the solar system at which thermal escape of H dominates losses. H temperatures at Mars retrieved from analysis of altitude-resolved H profiles typically confirm the early Mariner measurements, with few exceptions. These H temperatures, including that from the Mars 5 absorption cell derived from the width of the Lyman alpha line, are

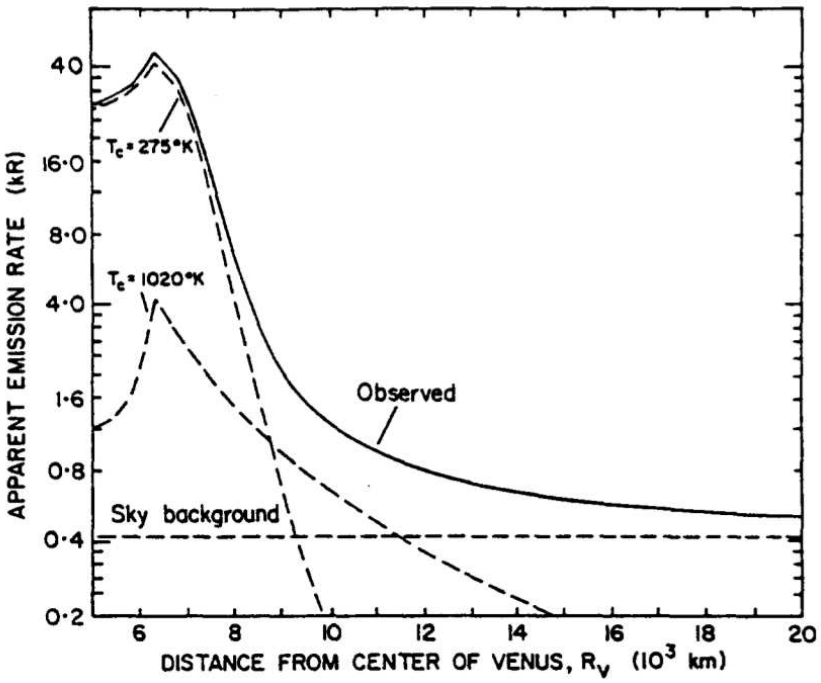

Figure 2.16: Detection of hot hydrogen in the exosphere of Venus by Anderson (1976).

typically near 350 K. The thermospheric CO_2 temperature expected from radiation balance and measured with aerobraking data is much lower, varying with season and location between 180 K and 210 K [Valeille et al., 2009, Bougher et al., 2014]. The elevated temperature of the H corona retrievals relative to the bulk atmosphere remains a mystery, but could be the signature of a hidden hot hydrogen component.

At Mars there has been no definitive detection of distinct thermal and nonthermal channels for H escape. One SPICAM profile analyzed by Chaufray cannot be fit with a single thermal population at any temperature, but this situation is unique in the SPICAM dataset. Detection of a Venus-like charge-exchanged component is much more difficult at Mars, because although the planets have similar temperatures in their upper-atmospheres (set by the physics of CO2 cooling), Martian gravity is weaker by a factor of 2.5 at the 200km level, so that the thermal H component is much less tightly bound. This loose binding leads to much larger thermal escape rates and masks any nonthermal component under a strong thermal signature. Theoretical predictions of the contribution of charge exchange and dissociative recombination to exospheric densities performed by Nagy [Nagy et al., 1990] and Lichtenegger [Lichtenegger et al., 2006] suggest that the influence of a hot component should be minimal (Figure 2.17).

Nevertheless, a hot component may exist, as suggested by several SPICAM retrievals that require a very large thermal temperature to obtain a satisfactory fit (see Chapter 4). The situation remains unclear, but may be resolved by future analysis of the distant corona where a hot population would tend to dominate the densities and intensities observed. One such observation has already been made by MAVEN (see Chapter 6), and others will be made in the future by additional spacecraft at Mars, including the Emirates Mars eXplorer.

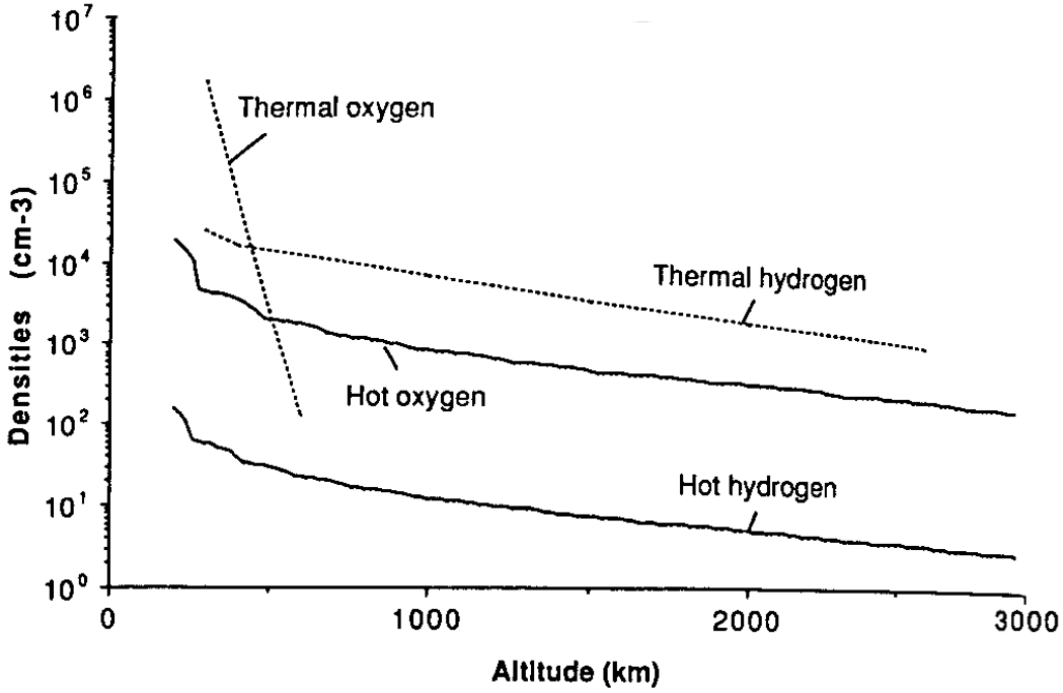

Figure 2.17: Computed altitude distributions of thermal and hot hydrogen and oxygen, from Nagy et al. (1990). While oxygen densities are affected by a substantial hot component, hydrogen densities are comparatively unaffected.

Chapter 3

H corona model

Analysis of the Mars H corona requires detailed physical and radiative transfer modeling, particulary in the inner corona (1-10r_M), for which the vast majority of data is available. Forward analysis is required because H Lyman alpha is an optically thick emission at Mars, just as it is nearly everywhere else in the universe. In order to reduce observations and retrieve information about the atmosphere, a physical model of H density is coupled to a radiative transfer model that simulates solar scattering by H atoms. For our analysis of coronal emissions, we couple a Chamberlain exosphere model to a radiative transfer model ultimately derived from the work of Thomas [Thomas, 1963], with contributions by Anderson, Bertaux, and Chaufray. More sophisticated models physical and radiative transfer models exist; two of these are discussed at the end of the chapter.

3.1 Physical model

The physics of atmospheric escape was first explored in detail by James Jeans in the course of developing the kinetic molecular theory [Jeans, 1925]. Jeans gave the first quantitative estimates of the ability of planetary atmospheres to retain their gas, explaining the lack of an atmosphere around the Moon and concluding that Mars would lose hydrogen and helium, but not heavier gases, from its atmosphere via thermal escape. These efforts were formalized by Chamberlain, who gave expressions for the radial density distribution in the upper atmosphere and the escape flux to space in terms of special functions [Chamberlain, 1963]. This simplest model of thermal atmospheric escape, often called Jeans escape, assumes an instantaneous transition from a completely collisional

to a completely collisionless atmosphere at a fixed altitude, called the exobase. The density structure of the atmosphere above the exobase is purely a function of an assumed Maxwellian density and temperature at the there, so that the escape flux and density of the atmosphere at every point can be computed analytically. Velocity distributions along an arbitrary line of sight can also be derived [Bertaux, 1978]: these distributions are useful for comparison with spectrally resolved observations of the corona, such as those made with H and D absorption cells.

The early work of Chamberlain was improved upon with the inclusion of additional effects, including a non-uniform exobase [Vidal-Madjar and Bertaux, 1972], solar radiation pressure [Bertaux and Blamont, 1973] and planetary rotation [Hartle, 1973]. More recently, complete analytic solutions to the exospheric density under the influence of radiation pressure have been obtained by Beth [Beth et al., 2015a,b]. In the current work, none of these extensions are included, as we are just beginning to have enough data to discriminate between the models.

Because Chamberlain models assume a uniform density n_{exo} and Maxwellian temperature T_{exo} at the exobase, they are typically discussed in terms of their dimensionless **escape parameter** or **Jeans parameter**, defined as the ratio of escape speed to most probable kinetic speed:

$$\lambda(r) = \frac{GMm}{kT_{\mathrm{exo}}r}; \qquad \lambda_{\mathrm{exo}} = \lambda(r_{\mathrm{exo}}).$$

In terms of this parameter, the escape flux $\mathcal{F}_{\mathrm{esc}}$ at the exobase can be computed as

$$\mathcal{F}_{\mathrm{esc}} = n_{\mathrm{exo}}\frac{v_{\mathrm{mp}}}{2\pi^{1/2}}(1+\lambda_{\mathrm{exo}})e^{-\lambda_{\mathrm{exo}}}, \qquad v_{\mathrm{mp}} = \sqrt{\frac{2kT}{m}}.$$

The factor in the escape flux multiplying the density is sometimes called the **effusion velocity**, or effective velocity of escape at the exobase. As can be seen from this formulation, Jeans escape increases rapidly with temperature and decreases exponentially with particle and planetary mass, making this escape most significant for hot, light gases on planets with low mass. The strong temperature dependence of Jeans escape is illustrated in Figure 3.1, which demonstrates the fraction of the Maxwell velocity distribution capable of escaping from a 200 km exobase at Mars.

If the exosphere is collisionless, the density at every point in the exosphere can be computed analytically using Liouville's theorem, which states that phase-space density is conserved along

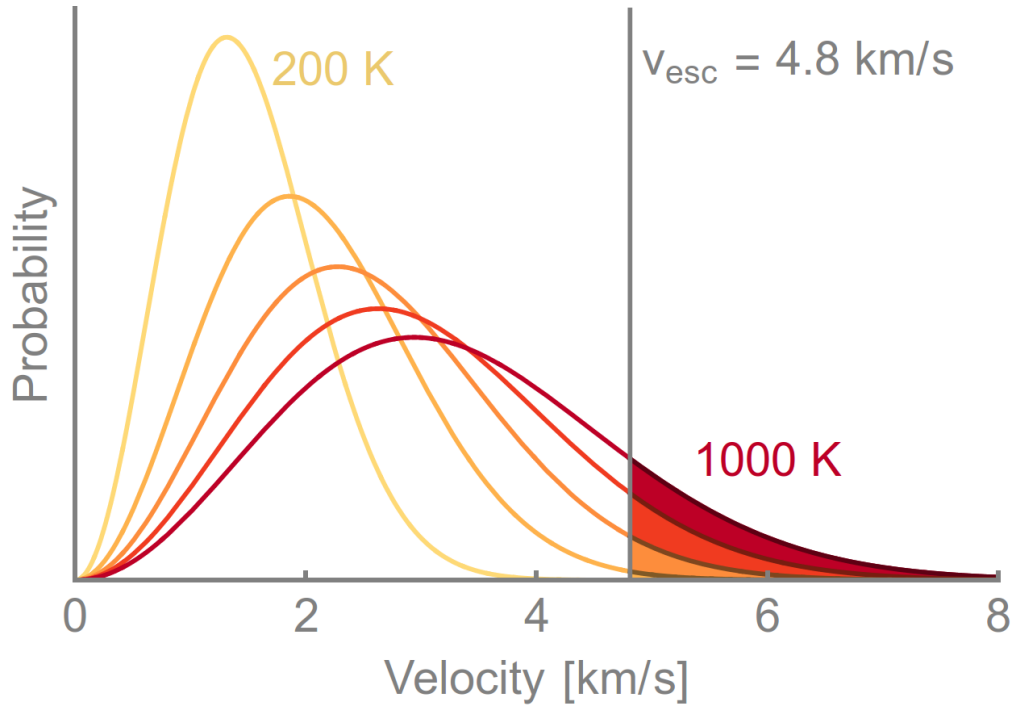

Figure 3.1: Maxwellian velocity distributions with escaping component illustrated. Temperatures are uniformly spaced in 200 K increments. Velocity shown is escape velocity from Mars at 200 km altitude.

dynamical trajectories. Computing the density at a given point in the exosphere therefore amounts to integrating over the dynamically allowed velocity space at that point under the assumptions that 1) all particles must intersect the exobase; and 2) no unbound infalling particles exist. These assumptions result in the following expression for exospheric density:

$$
\begin{aligned}
n(r) &= n_{\text{exo}} e^{-\lambda_{\text{exo}}+\lambda} \zeta(\lambda), \\
\zeta(\lambda) &= \pi^{-1/2} \left\{ \Gamma(3/2) + \gamma(3/2,\lambda) - \frac{(\lambda_{\text{exo}}^2 - \lambda^2)^{1/2}}{\lambda_{\text{exo}}} e^{-\psi} [\Gamma(3/2) + \gamma(3/2, \lambda - \psi)] \right\}, \\
\psi &= \frac{\lambda^2}{\lambda + \lambda_{\text{exo}}},
\end{aligned}
$$

where γ is the lower incomplete gamma function. Computed exospheric density distributions resulting from the above expression are shown in Figure 3.2, which also shows the vertical optical depth τ for these profiles, as defined in the next section.

Before it reaches the exobase, exospheric constituents including H must diffuse through the neutral atmosphere. In the present work, thermospheric diffusion is modeled between 120 and 200 km following Krasnopolsky [Krasnopolsky, 1993]:

$$
\Phi_H(r) = -(D+K)\frac{dn}{dr} - \left[D\left(\frac{1}{H} + \frac{1+\alpha_T}{T}\frac{dT}{dr} \right) + K\left(\frac{1}{H_a} + \frac{1}{T}\frac{dT}{dr} \right) \right] n,
$$

where $\Phi_H(r) = (r_{\text{exo}}/r)^2 \Phi_H(r_{\text{exo}})$ represents the altitude-dependent escape flux, equal to the Jeans flux at the exobase. D is the binary diffusion coefficient of hydrogen through CO_2, K the eddy diffusion coefficient, $H = kT/mg$ the hydrogen atmospheric scale height, H_a the neutral atmospheric scale height, and α_T the thermal diffusion coefficient. In the present work binary and eddy diffusion coefficients are taken from the work of Hunten [Hunten, 1973] and Krasnopolsky, respectively. Because it is a first-order differential equation, this expression can be solved analytically for the hydrogen density below the exobase using the density at the top of the atmosphere as a boundary condition.

Deep in the atmosphere, H is controlled by the mean atmospheric scale height rather than its own much larger scale height. At such low altitudes, bulk atmospheric chemistry and dynamics become important, the subject of Chapter 5. For the purposes of modeling coronal airglow, below

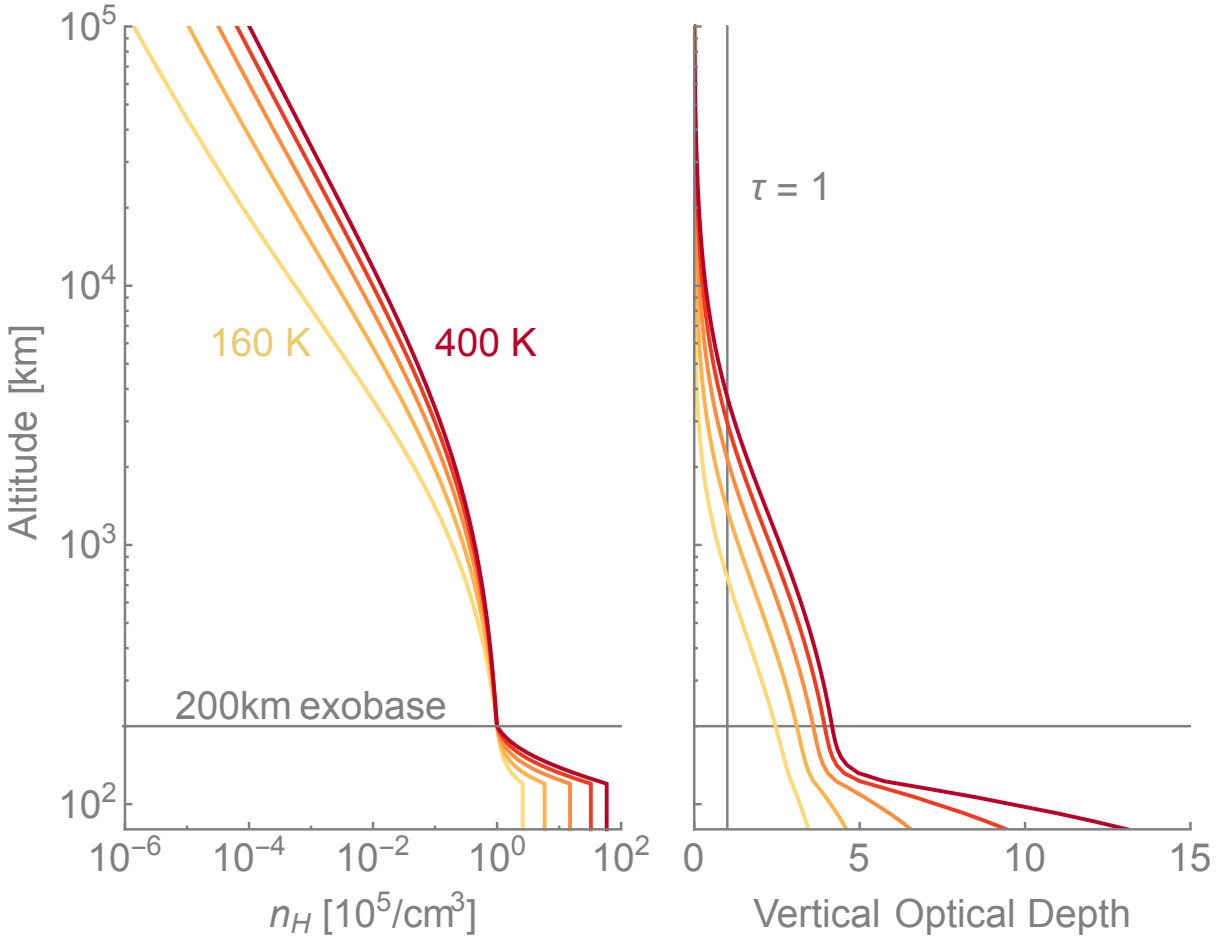

Figure 3.2: Chamberlain exosphere densities for Mars and associated optical depth. At left, densities resulting from a Chamberlain exosphere at temperatures from 160-400 K, in 60 K increments. All profiles share a density of 10^5 cm^{-3} at the 200 km exobase, a multiplicative parameter. At right, vertical optical depths calculated from infinity using the H cross section given in the text.

120 km the H density can be assumed constant with minimal effect on the airglow, due to both the large H optical depth between the corona and these altitudes and the increasing absorption of Lyman alpha by CO_2 at depth.

3.2 Radiative transfer model

The radiative transfer model computes the brightness scattered by the corona density distribution. Light scattered in the corona is absorbed and emitted by individual hydrogen atoms, whose scattering properties are defined in terms of the total cross section σ of the natural line, a function of fundamental constants and the oscillator strength f as

$$\sigma = \frac{\pi e^2}{m_e c} f.$$

For Lyman alpha $f = 0.416$. If light is scattered by atoms with a Doppler velocity distribution with Doppler width Δv_D the line center cross-section is given by

$$\sigma_0[\mathrm{cm}^2] = \frac{\sigma}{\Delta v_D \sqrt{\pi}} = 5.96 \times 10^{-12} (T[K])^{-1/2}; \qquad \Delta v_D = \frac{1}{\lambda_0}\sqrt{\frac{2kT}{m}},$$

where $\lambda_0 = 121.6$ nm. With this cross section, the line center optical depth τ_0 through the atmosphere along a specified line of sight is

$$\tau_0 = \sigma_0 \int n \, ds.$$

This expression is used to compute the vertical optical depth shown in Figure 3.2. Vertical optical depths at the Martian exobase almost always exceed unity. Scattering in the atmosphere is an important process: limb observations of the atmosphere almost always require radiative transfer modeling to be interpreted.

The major work of this thesis employs perhaps the simplest useful model of coronal radiative transfer, which nevertheless requires a significant amount of computer time to implement. The model is derived from the pioneering work of Gary Thomas [Thomas, 1963] on the hydrogen corona of the Earth; his methods have been adapted with minimal modification to the Mars corona for nearly every previous analysis of Lyman alpha airglow.

3.2.1 Thomas model

Thomas models perform frequency-integrated optically thick radiative transfer using a fixed line profile that applies everywhere in the atmosphere. The assumption of a fixed line profile allows the probability of a photon making a trip between any two points in the atmosphere to be computed using the frequency-integrated optical depth. Frequently, this probability is computed with the Holstein T function [Holstein, 1947][1]:

$$T(\tau) = \pi^{-1/2} \int_{-\infty}^{\infty} e^{-x^2} e^{-\tau e^{-x^2}} dx.$$

This expression assumes a Doppler line profile (resulting in the Gaussian shape in the exponent), and complete frequency redistribution with each scattering (so that the probability of photon transfer is independent of the original frequency of the photon).

Assuming the atmosphere has the same line shape everywhere, we can use this expression to compute atmospheric scattering. Each point in the atmosphere sees the brightness of every other point diminished by the optical depth between them. The brightness of the atmosphere at every point can therefore be expressed as the illumination of the Sun plus an integral over the brightness of every other point in atmosphere:

$$S(\mathbf{r}) = n(\mathbf{r})T(\tau_\odot) + \sigma_0 n(\mathbf{r}) \int_{4\pi} \frac{d\mathbf{\Omega}}{4\pi} \int_0^{\infty} ds\, S(\mathbf{r} + s\mathbf{\Omega})\, G(\tau_0(\mathbf{r}, \mathbf{r} + s\mathbf{\Omega})),$$
$$G(\tau) = -\frac{dT}{d\tau} = \pi^{-1/2} \int_{-\infty}^{\infty} e^{-2x^2} e^{-\tau_0 e^{-x^2}} dx,$$

where $gS = \varepsilon$, the atmospheric emissivity in photons cm^{-3} s^{-1}, and $g = F_\odot \sigma$ is the solar scattering coefficient, folding the brightness of the Sun together with the natural strength of the line of interest.[2] $\tau_\odot$ represents the line center optical depth from the atmosphere point $\mathbf{r}$ to infinity in the direction of the Sun. S is called the source function, with units of effective scatterer density. The above expression does not account for pure absorption of Lyman alpha by CO_2; this is included in the model by multiplying in $e^{-\tau_{CO_2}}$ next to every appearance of the T and G functions. In the simpler

[1] The name of this function was coined by Gary Thomas in the course of his PhD work.

[2] For Lyman alpha at Mars, g is typically $(0.5 - 1.5) \times 10^{-3}$ s^{-1}, with the smallest value at aphelion solar min and the largest at perihelion solar max.

world of optically thin radiative transfer, only the first term in the equation for the source function applies; multiple scattering makes only a negligible contribution, and we can ignore the integral over S which appears on the left side of the equation. Within the integral, G is the Holstein G function, representing the differential transmission of the atmosphere at each point. Plots of T and G are shown in Figure 3.3, demonstrating the falloff in transfer efficiency with increasing optical depth.

The integral equation for S is classified as a Fredholm equation of the second kind, and is amenable to many numerical methods of solution [Delves and Mohamed, 1985]. The integration over the atmosphere on the right-hand side is classified into two components: S, which we want to find, and the integration kernel $K(\mathbf{r}, \mathbf{r}') = \sigma_0 n(\mathbf{r}) G(\tau(\mathbf{r}, \mathbf{r}'))/4\pi$. Most methods for solving for the source function employ an discrete iterative approach, computing S on a specified atmospheric grid, usually spherical. The continuous function S is replaced by its discrete approximation $\mathbf{S}$, and the integral is replaced by a matrix multiplication:

$$\mathbf{S}_0 = n(\mathbf{r}) T(\tau_\odot)$$

$$\mathbf{S}_{i+1} = \mathbf{S}_i + \mathbb{K}\mathbf{S}_i.$$

$\mathbb{K}$ is called the influence matrix, defining the degree to which each point in the atmosphere has its radiance influenced by every other point. Computing this matrix is the major task of the radiative transfer model. In the present work, this matrix is computed by ray shooting from each point in the atmosphere. Starting with a given grid point $\mathbf{r}$, rays are traced outward on a spherical grid with a uniform spacing in optical depth. At each point $\mathbf{r}'$ on the outward ray, the kernel K is computed and assigned to the surrounding points in the atmosphere using inverse bilinear interpolation (Figure 3.4). This technique was originally developed by Bertaux as part of his PhD thesis [Bertaux, 1974], and has been used at Mars previously by Chaufray [Chaufray et al., 2008]. An alternative approach due to Anderson and Hord [Anderson and Hord, 1977] decomposes the response of the atmosphere onto a set of basis functions, whose response is easy to compute.

In the present work, we assume spherical symmetry in hydrogen density and azimuthal symmetry in the source function about the Mars-Sun line. For a specified exobase number density and tem-

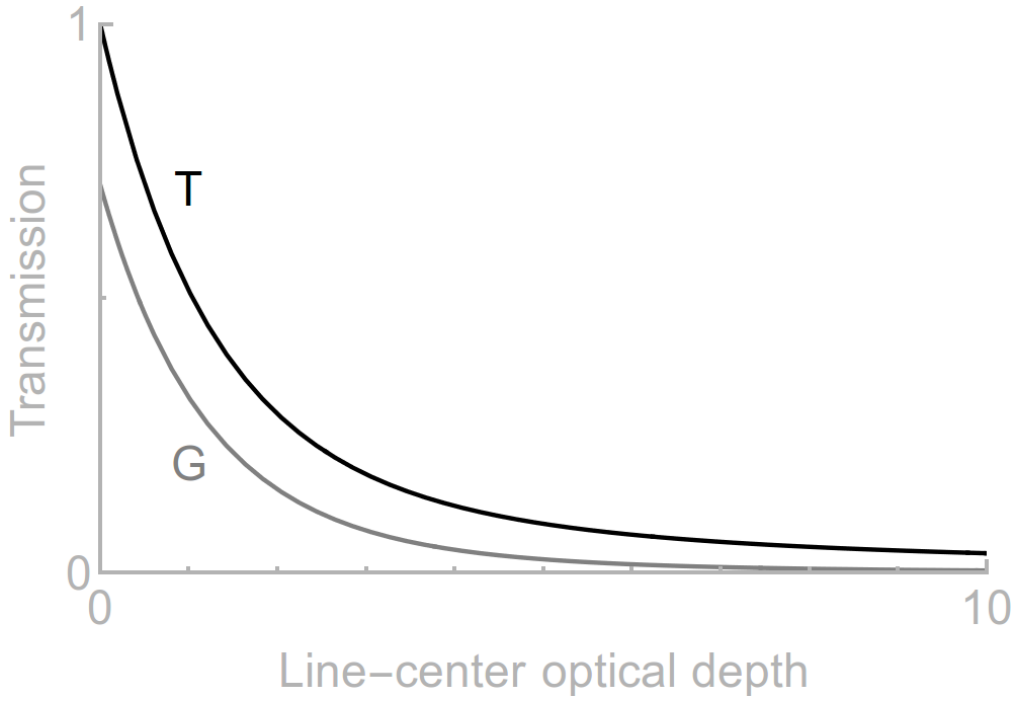

Figure 3.3: Holstein T and G functions, as defined in the text. Note that $T \sim 0.5$ when $\tau \sim 1$.

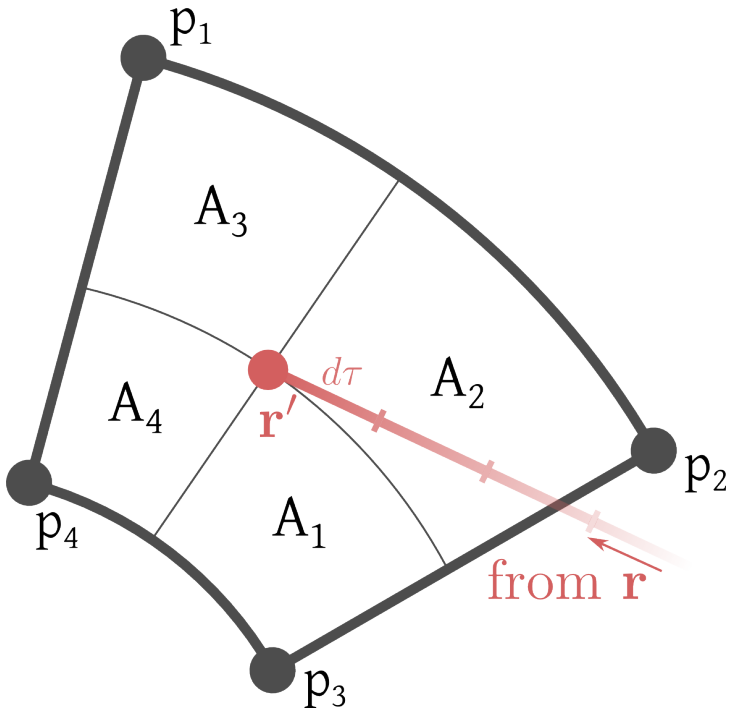

Figure 3.4: Scheme for inverse bilinear interpolation. Rays are shot out of each point in the atmosphere $\mathbf{r}$ on a spherical grid, stepping forward with radial increment $d\tau$. At each point $\mathbf{r}'$ the source function kernel is computed and assigned to surrounding points in the original grid ($\mathbf{p}_1$-$\mathbf{p}_4$) in proportion to the areas indicated. The model performs this integration in 3D.

perature, radial density profiles are calculated and used in the computation of the source function, which is stored for later integration and comparison against spacecraft data. For the work of this thesis, source functions were precomputed for exobase densities in the range $1 \times 10^4 - 7 \times 10^5$ cm^{-3} and temperatures in the range $100 - 1600$ K. An example of such a source function is shown in Figure 3.5.

Given a source function, the brightness of the atmosphere along any line of sight is computed by line integration:

$$I_{\text{obs}}(\mathbf{r}, \mathbf{\Omega}) = \frac{g}{4\pi} \int_0^\infty S(\mathbf{r} + s\mathbf{\Omega}) T(\tau_0(\mathbf{r}, \mathbf{r} + s\mathbf{\Omega})) e^{-\tau_{CO_2}} ds.$$

The geometry of this integration is defined by the observations that are being compared with the model. In each case, the instrument position and look direction relative to the atmosphere must be used to determine the initial point $\mathbf{r}$ and look direction $\mathbf{\Omega}$.

Simulated images of coronal brightness for a fictional atmosphere are shown in Figure 3.6. The asymmetric structure of the corona shown in these images results entirely from scattering in the extended H corona; the underlying density distribution is spherically symmetric.

3.3 H Lyman alpha Solar brightness and IPH

Because the H corona is observed in scattered sunlight, an accurate determination of the solar brightness at H Lyman alpha is required to convert observed brightness to coronal density. Measurements of Lyman alpha made by SORCE [Rottman et al., 2006] show that the brightness of the Sun at 121.6 nm can change by a factor of two across a solar cycle, with smaller changes due to solar rotation and occasional impulsive changes as a result of active regions and flares. When the solar flux at Lyman alpha was not available from measurements at Mars, the SORCE solar brightness measured at Earth was rotated and scaled to Mars assuming a 26 day solar rotation period, using a method established by Dave Mitchell [Mitchell et al., 2001]. The entire SORCE dataset through the end of 2013 was processed using this technique. For the H corona, we are not interested in the total brightness of the Sun at 121.6 nm, but instead in the solar brightness at

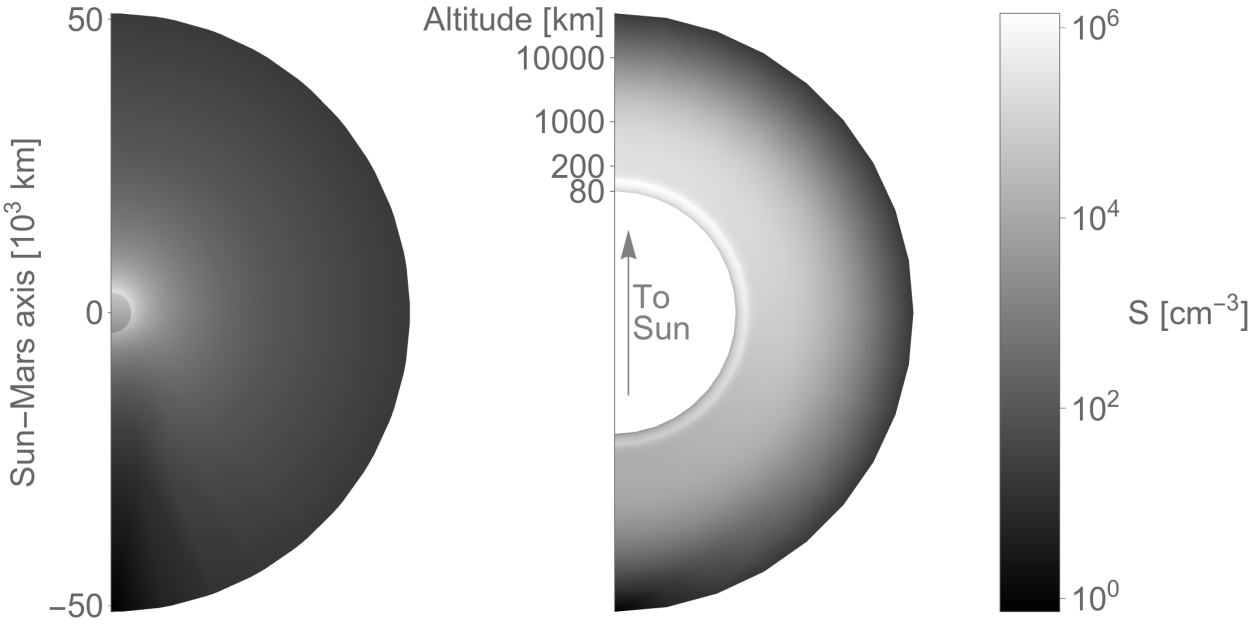

Figure 3.5: Example model source function. At left, effective scattering density of the atmosphere, with the planet at the center and sunlight entering from the top. The source function is three dimensional, with symmetry about the Mars-Sun axis. At right, the same source function plotted in logarithmic altitude space, revealing the airglow layer. Note the logarithmic intensity scale, illustrating the six order of magnitude difference in scattering density between the brightest and dimmest regions of the atmosphere.

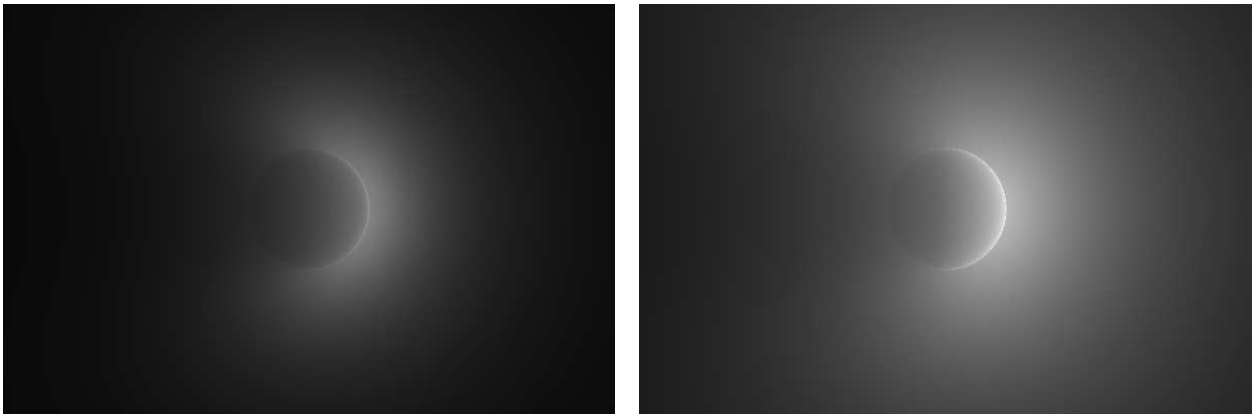

Figure 3.6: Simulated images of the model corona, observed from $10\,r_{\mathrm{Mars}}$ directly below the planet. The Sun is to the right in each image. Each model has the same exobase density of 5×10^4 cm^{-3}. (left) Modeled coronal brightness for an exobase temperature of $T = 350$ K. (right) $T = 750$ K. Both images share an identical linear scale, with black 0 kR and white 15 kR. Peak brightness of the image on the right is 9 kR.

line center, as the thermal population that makes up most of the Martian H corona has a thermal width, much smaller than the solar line (see Figure 3.7). To obtain the line center brightness from the broadband value we employ the relation of Emerich [Emerich et al., 2005]:

$$\left(\frac{I_{\text{line-center}}}{10^{11}\ \text{cm}^{-2}\ \text{s}^{-2}\ \text{nm}^{-1}}\right) = 0.64 \left(\frac{I_{121}}{10^{11}\ \text{cm}^{-2}\ \text{s}^{-2}}\right) \pm 0.08.$$

This quantity is shown for the period 2002-2014 in Figure 3.8.

Observations of the corona necessarily observe background hydrogen in the interplanetary medium (IPH). The IPH is not bright in comparison to the H corona of Mars, reaching values of 500-1000 R, while the corona is typically much brighter, ranging from 1-10 kR. At the highest altitudes, however, the IPH can contribute a large fraction of the signal observed, and exerts a substantial influence on the temperature retrieved for the H corona there, mimicking a hot population of H atoms. To remove the IPH from our measurements, we employ a radiative transfer model of Eric Quemerais, based on a hot IPH density model of Lallement [Lallement et al., 1985], which reproduces SOHO/SWAN observations of the IPH to within 10%. This model incorporates the direction of the incoming H flow, charge exchange with the solar wind, and radiation pressure effects, as well as the changing solar flux at 121.6 nm that illuminates the IPH. For each observation analyzed in the present work, the ecliptic latitude and longitude of the observation line of sight was computed and fed to the model, which together with the solar brightness at that time allowed a determination of the background contribution to the signal observed.

3.3.1 Exospheric line profiles

Most observations of the Mars H corona have not had sufficient spectral resolution to resolve the width of the planetary line. Observations of the line shape have the potential to discriminate between escaping and bound components in the exosphere, and diagnose the existence of satellite populations, as determined by Bertaux [Bertaux, 1978]. For a complete accounting of coronal extinction of the solar line and IPH, computation of line profiles is also useful.

To compute line profiles, the standard formalism for integrating over the allowed velocity space must be extended. Observations along a line of sight at a particular wavelength will capture

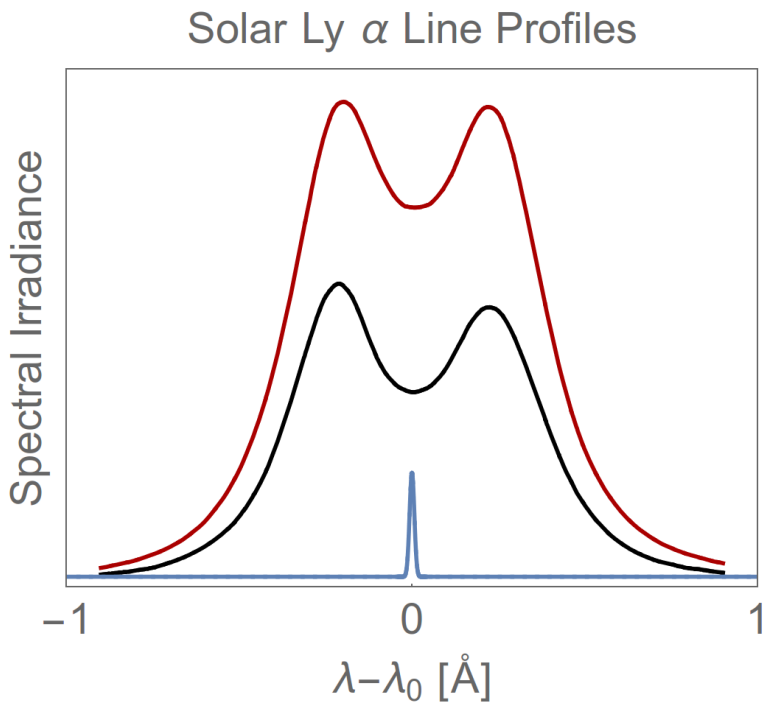

Figure 3.7: Solar and H coronal Lyman alpha line widths. Red and black show relative intensity of solar line at solar max and min, respectively. Blue shows the thermal width of the H population at Mars for $T = 350$ K.

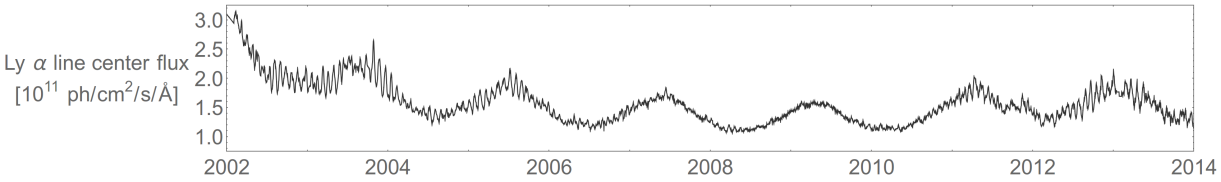

Figure 3.8: Mars Ly α flux, 2002-2014, from SORCE. Flux values have been rotated and scaled from Earth measurements to the location of Mars. Major modulations are due to the eleven-year solar cycle (minimum in 2008), the eccentricity of Mars' orbit, and solar rotation.

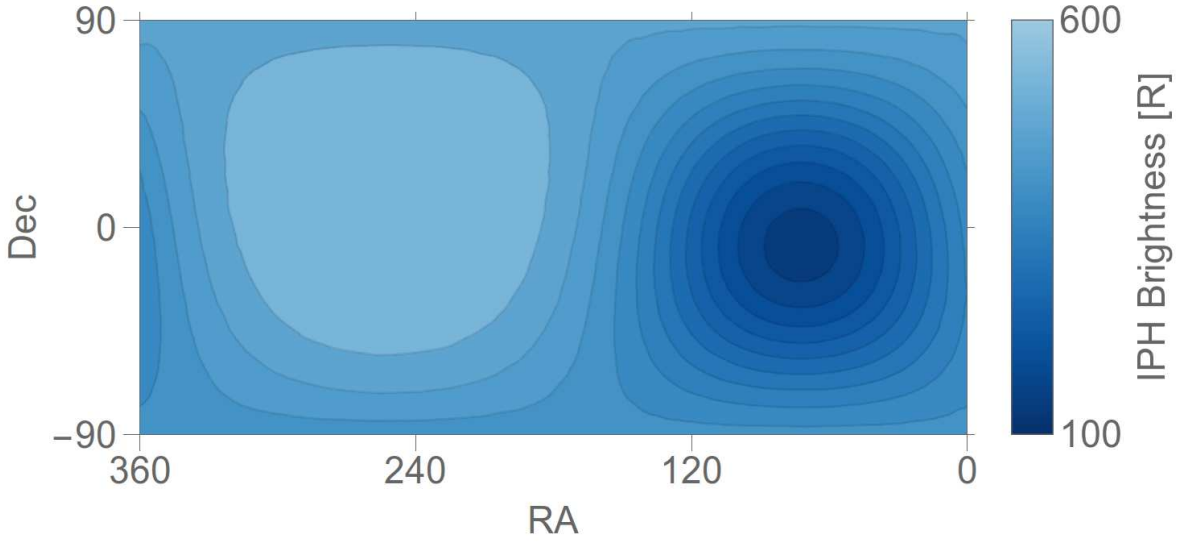

Figure 3.9: Modeled structure of the IPH from the Quemerais model. For each SPICAM observation, this model is scaled to the appropriate solar flux. The background IPH brightness is then extracted from the model using the RA/Dec look direction of the instrument.

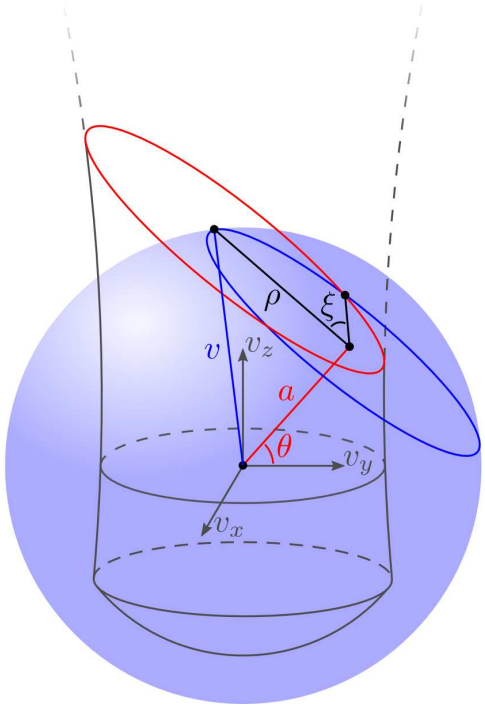

Figure 3.10: Dynamically allowed velocity space in a Chamberlain exosphere. Axes are locally tangent to the planet, with v_z pointing radially outward. At each point in the atmosphere, the restriction that all particles intersect the exobase with no infalling unbound particles results in a hyperbolic integration region capped on the radially infalling end by a sphere (gray). All particles traveling at a specified velocity a along the line of sight must be in a plane (red). The density of particles traveling at a specified velocity at a given point is the integral of the intersection region of the plane and hyperboloid. This integration is straightforward when performed in spherical coordinates (blue).

only one component of the velocity distribution at each point in the atmosphere. The geometry of the allowed velocity space is shown in Figure 3.10. This figure shows the local velocity distribution at a single point along the line of sight; we must also integrate along the line of sight, accounting for the fact that the specified line-of-sight velocity intersects a different portion of the velocity space at every point. One easy way to parameterize this is by converting from line of sight distance to planetocentric angle using the transformation $s = b \tan\theta$ (Figure 3.11).

With this transformation, the optical depth of the atmosphere along a particular line of sight at each velocity a can be expressed in the following way:

$$\begin{aligned}
\tau_\alpha &= \frac{2\sigma_0 c}{\nu_0}\frac{n_{\rm exo} b}{\pi^{3/2} v_{\rm mp}} e^{-\lambda_{\rm exo}} F(\lambda_{\rm exo}, \lambda_b, \alpha, \theta_0) \\
F &= \int_{\theta_0}^{\pi/2} e^{\lambda_b \cos\theta} \sec^2\theta \, G(\lambda_b, \alpha)\, d\theta \\
G &= \int_{\alpha}^{\sqrt{\lambda_b \cos\theta}} e^{-v^2}(\xi_+ + \xi_-) v\, dv + \int_{\sqrt{\lambda_b\cos\theta}}^{\infty} e^{-v^2}\xi_+ v\, dv \\
\cos\xi_\pm &= \frac{\pm\sqrt{v^2(1-\lambda^2/\lambda_{\rm exo}^2) - \lambda^2/\lambda_{\rm exo}(1-\lambda/\lambda_{\rm exo})} - \alpha\sin\theta}{\cos\theta\sqrt{v^2-\alpha^2}} \\
\alpha &= a/v_{\rm th} \\
\lambda &= \lambda_b \cos\theta,
\end{aligned}$$

where $\lambda_b = GMm/kTb$, the escape parameter at the closest point to the planet along the line of sight. The first integral above is along the line of sight from the observer location, the second integrates over the intersection of the specified line-of-sight velocity a with the dynamically allowed velocity space at each point. Because the orientation of the line of sight with respect to the local vertical changes with line-of-sight distance, the specified velocity a intersects a different portion of the velocity space at each point. This highly nested but analytically expressible integral is computed for every line of sight in the present model, to compute the amount of extinction the atmosphere imposes on the interplanetary hydrogen emission. The same integral can be used to compute the extinction of the solar line, useful for comparison with solar occultation measurements of the H corona. To save time, line extinction profiles are precomputed for the full range of coronal parameter space. The precomputed profiles are loaded and interpolated to compute the extinction

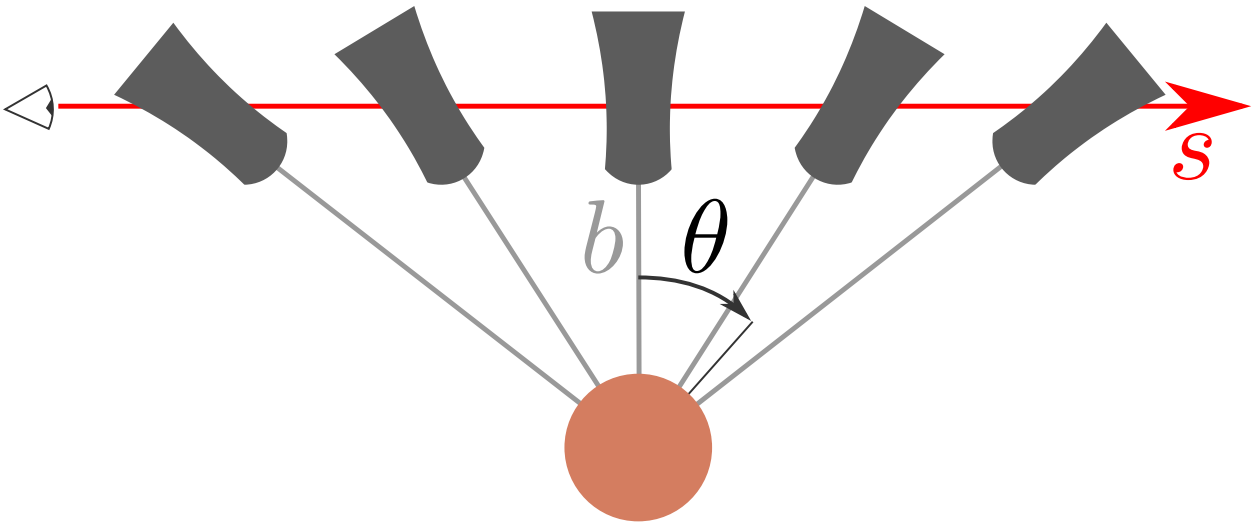

Figure 3.11: Geometry of a line of sight integration through the exosphere, illustrating the orientation of the dynamically allowed velocity space (gray sphere-capped hyperboloids) at each point.

experienced along all lines of sight through the H corona.

Figure 3.12 shows computed line optical depths and extinction resulting for observations across the corona with an exobase density and temperature as measured by Mariner, $n = 5 \times 10^4$ cm^{-3}, $T = 350$ K. The orbit shown and the altitudes of the lines of sight are chosen to match the MAVEN coronal scan observations. At the deepest lines of sight through the corona, line center optical depth approaches 10, and the optically thick portion of the line approaches 10 mÅ in width. The Doppler shift of IPH relative to Mars controls the extinction imposed by the corona, and varies in the range ± 50 km s^{-1} = ± 200 mÅ, depending on the location of Mars in its orbit and the look direction of the line of sight on the sky. At the lowest altitudes and with zero Doppler shift, up to 30% of the interplanetary hydrogen signal can be scattered out of the line of sight by the corona, as indicated in Figure 3.13, which shows IPH line profiles measured by SWAN/SOHO [Quémerais et al., 1999] extincted by modeled coronal lines.

In addition to scattering interplanetary Lyman alpha out of any given line of sight, the corona also necessarily scatters Lyman alpha out of the solar line. This makes the corona visible in absorption against the Sun at very high altitudes. Figure 3.14 shows the extinction imposed by the corona on the solar line for a MAVEN-sized orbit around Mars. Because MAVEN is always completely embedded in the H corona, extinction of the solar line approaching the percent level is almost always present for Solar Lyman alpha.

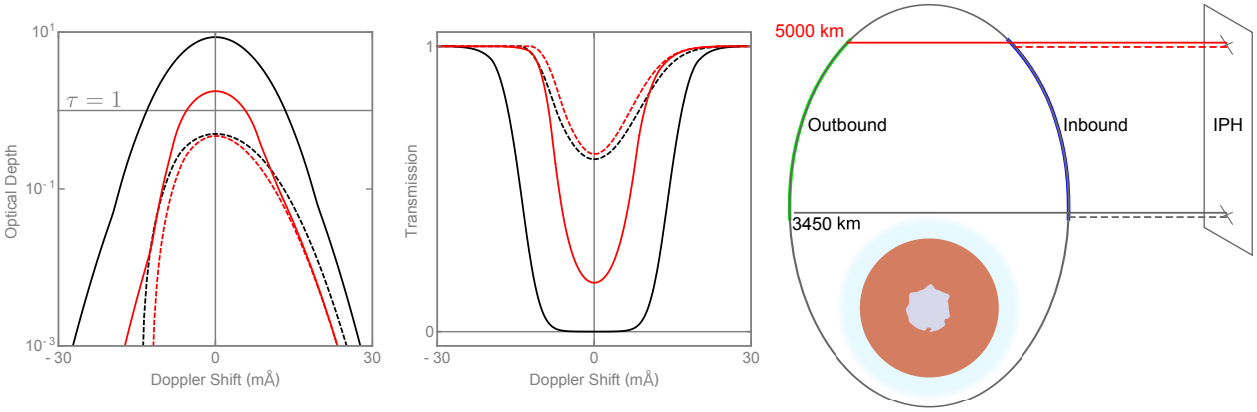

Figure 3.12: Coronal line shapes and transmission through the corona for several lines of sight. Altitudes shown are accurate for the MAVEN orbit around Mars. Dashing and colors indicate the lines of sight and profiles on each figure.

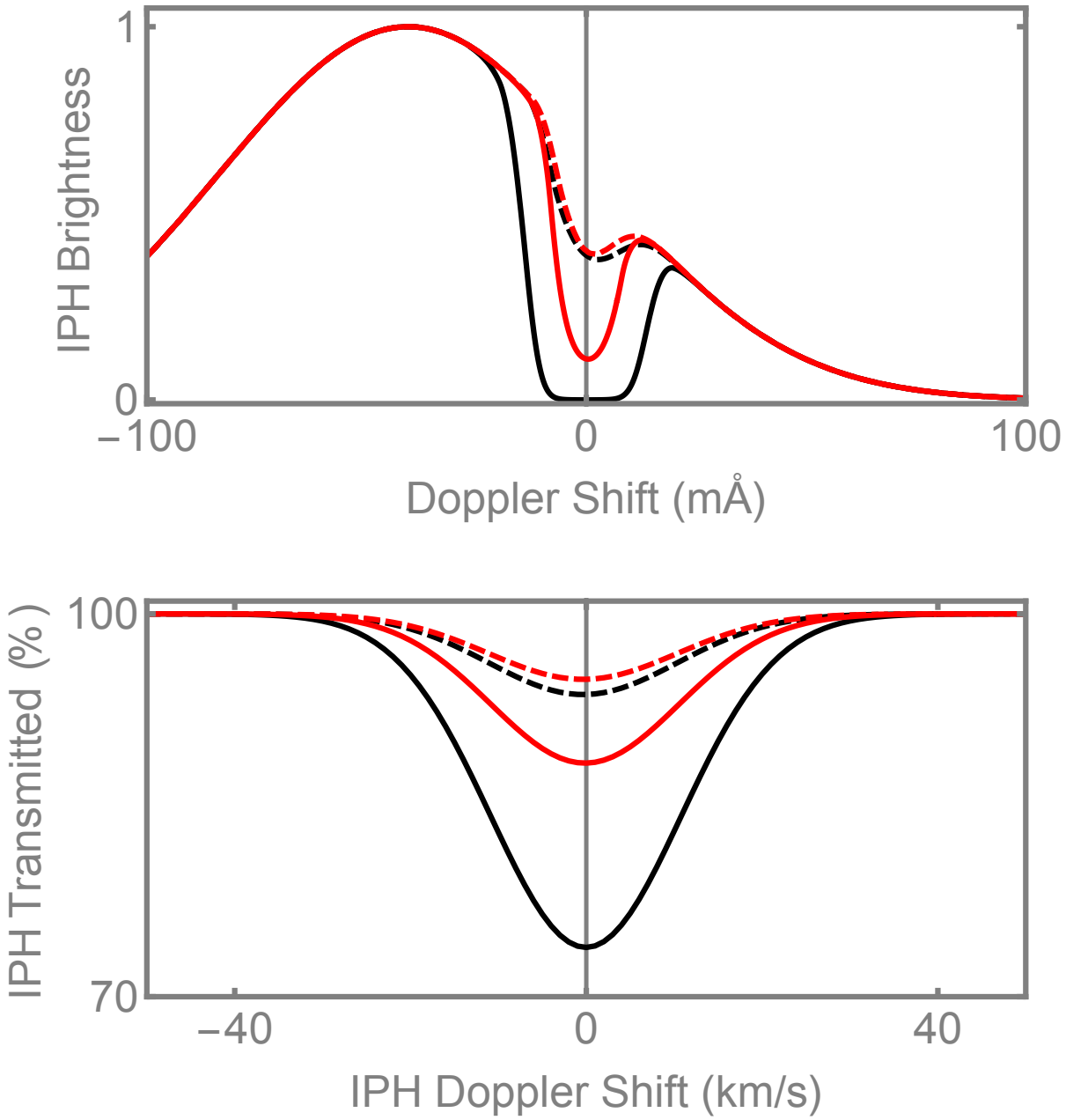

Figure 3.13: Absorption of the IPH by the H corona. Line colors and dashing are keyed to the geometry shown in Figure 3.12. (top) IPH line profiles with Mars for an arbitrary Doppler shift, with coronal extinction imposed. (bottom) Amount of IPH transmitted as a function of the IPH Doppler shift along the line of sight.

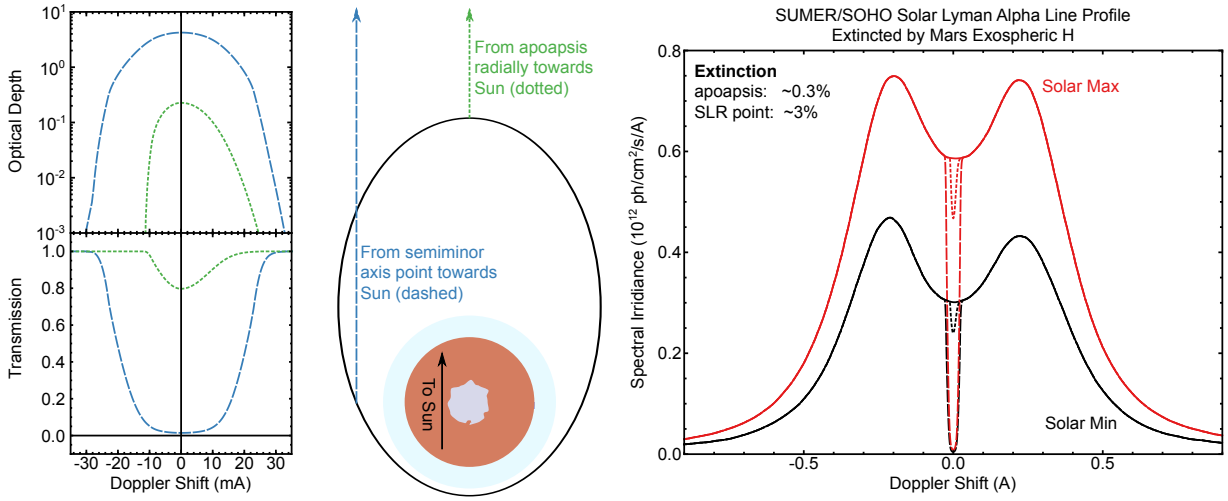

Figure 3.14: Coronal line shapes and transmission through the corona towards the Sun. Long dash blue lines show profiles and extinction from the semiminor axis point. Green short dash lines show profiles and extinction from apoapsis towards the Sun. Orbit shown is the size of the MAVEN orbit around Mars, oriented with apoapsis on the Mars-Sun line. At left, the effect of coronal absorption on the solar line profile.

3.3.2 More sophisticated models

The physical model employed in this work is the simplest useful model capable of describing the density distribution of a planetary corona, but reality is not always so simple. Many of the assumptions made to develop the Chamberlain model are artificial: the most immediately obvious are the assumption of a uniform Maxwellian temperature everywhere on the planet, a similarly uniform density, and a fixed altitude exobase where the atmosphere instantaneously transitions from collisional to collisionless. Monte Carlo models relax these assumptions through direct simulation of particle transport and collisions. Monte Carlo models are often run in one dimension, owing to the computational expense of the simulation, but can also be used to simulate spatially varying escape on planetary scales.

One recent Monte Carlo simulation by Volkov [Volkov et al., 2011] is especially relevant to the work of this thesis. Using a Monte Carlo approach, these authors directly simulated the transition between a collisional and collisionless atmosphere for a variety of atmospheric temperatures, finding that the Jeans escape formula is quantitatively accurate to within a factor of ten for tightly bound atmospheres, with $\lambda > 3$. As the atmospheric temperature increases, these authors found a rapid departure from Jeans-like escape at $\lambda = 2 - 3$, as the atmosphere begins to transition to a hydrodynamic escape regime. For the H corona, $\lambda = 1$ at an exobase temperature of 1500 K, so that for temperatures less than about 500 K, the Jeans escape rate is correct to within an order of magnitude. For lower temperatures, the performance of the Jeans escape formula improves, and is accurate to within a factor of two for temperatures lower than 300 K.

As with the physical model, the Thomas radiative transfer model used here makes many useful but strictly invalid assumptions. In particular, it assumes that line cross sections are Doppler everywhere in the atmosphere, an assumption that gets increasingly bad with altitude as the dynamically allowed velocity space shrinks. For the H corona at Mars, this assumption is not bad; deviation from a Gaussian shape occurs very slowly, noticeable as a slight deviation from a parabolic line shape in Figures 3.12 and 3.14. More serious is the contribution of the wings of the line to the coronal

brightnesses observed. If two populations of H at different temperatures contribute to the corona, the hot population will tend to lift the wings of the line scattered by the cold population. This effect will increase with altitude, and cannot be accounted for without incorporating position-dependent line shapes into the radiative transfer.

Highly detailed radiative transfer models are built to handle situations where the assumptions of the Thomas model break down. Recently, Chaufray [Chaufray and Leblanc, 2013] applied one such model to the atmosphere of Mercury, where non-Maxwellian sodium atoms populate the exosphere. The success of relatively simple Chamberlain models in fitting the same exosphere as observed by MESSENGER [Cassidy et al., 2015] argues that use of these models is not always necessary to obtain satisfactory agreement with instrument data.

Chapter 4

SPICAM Observations

SPICAM (SPectroscopy for the Investigation of the Characteristics of the Atmosphere of Mars), mounted on the Mars Express spacecraft, has been gathering data at Mars for 10 years, providing a long baseline of measurements from which to constrain the behavior of the Mars atmosphere, ionosphere, and corona [Bertaux et al., 2006]. SPICAM is a spectrograph, but the raw data are heavily binned in the along-slit direction onboard the spacecraft, so that in most observation modes it operates as a point spectrometer. These point spectra are collected as coronal scans, revealing the altitude structure of Martian airglow as a function of altitude (Figure 4.1). The high Mars Express apoapsis of over 10,000 km allows the corona to be probed to extremely high altitudes.

Through analysis of SPICAM data from Fall 2007, some of the work of this thesis produced the first detection of time-variable H escape from the atmosphere of Mars [Chaffin et al., 2014]. Encouraged by this result, a more comprehensive survey of the entire SPICAM dataset was undertaken, resulting in the work described later in this chapter. The complete SPICAM dataset mostly samples the H corona in Northern summer, as opposed to the 2007 observations made in southern summer during a dust storm. The analysis undertaken here has shown that in northern summer, the H coronal parameters and escape rates retrieved are mostly consistent with previous results. In southern summer the large escape rates observed in Fall 2007 may be a result either of the global dust storm at that time or seasonal dynamics. The SPICAM dataset provides hints that seasonal dependence may be present, but cannot unambiguously determine the cause of the 2007 variations.

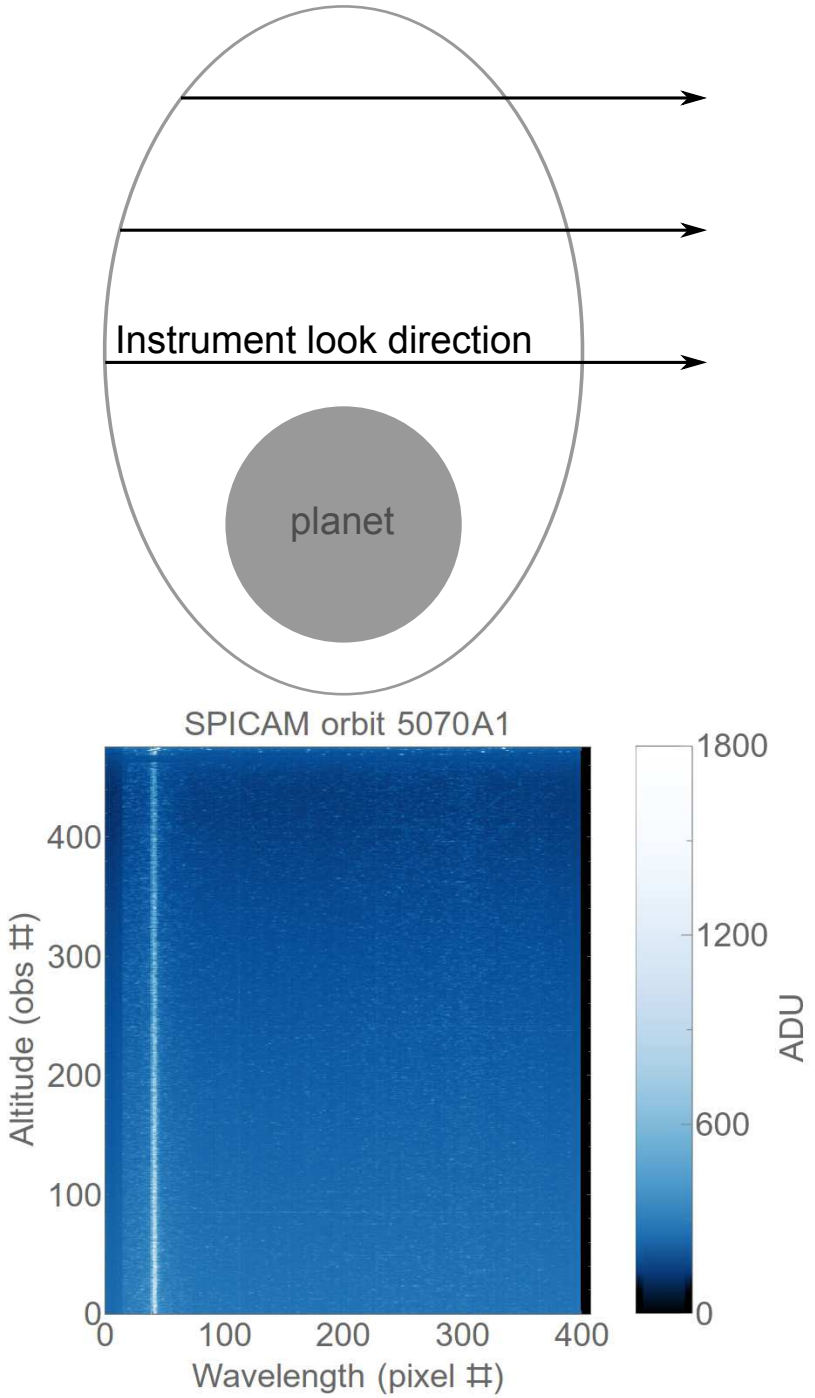

Figure 4.1: SPICAM detector response in analog-to-digital units (ADU) as a function of altitude. Lyman alpha is the conspicuous bright feature near pixel 40, diminishing in brightness with altitude as the spacecraft moves outward along its orbital track.

4.1 Results from the 2007 data

Early results studying a subset of the SPICAM data from the second half of 2007 were published in GRL in early 2013. Twenty limb scans from the Fall of 2007 were reduced for comparison with the model. This study spanning six months of SPICAM data represented the first analysis of coronal data capable of detecting time-variation in the corona on months-long timescale, as prior analysis was restricted to data sets gathered over shorter periods.

To compare observations of the corona with the model, we minimize chi-squared deviations of the data with respect to the model, using estimated instrumental uncertainties. The spacecraft location and instrument look direction are extracted from the data, and these values are used to fly the instument through the corona model in 3D, simulating the intensities the instrument would have seen. Model profiles are computed for a variety of temperatures and densities sampling the coronal parameter space; these profiles are then bilinearly interpolated in temperature and density to improve the fidelity of the sampling. Computed profiles are then compared with the data to find the best fit (Figure 4.2).

The model comparison with the data entails significant degeneracy. Typically, profiles can be well fit at a range of densities and temperatures, trading off one parameter against another to maintain roughly the same optically thick column density along the line of sight. This degeneracy can be explored in the chi-squared parameter space (Figure 4.3). A bright band indicates the range of parameters where the model approximates the observed intensities; in this space number density and temperature at the exobase are anticorrelated. A true minimum exists along this valley of acceptable parameters, but the location of the minimum is sensitive to the instrument absolute calibration. Contours of constant escape flux roughly track the anticorrelation of temperature and density, so that escape flux can be constrained better than either underlying parameter. Formal parameter uncertainties around the minimum and their correlation matrix can be found by tracing $\Delta\chi^2$ contours around the minimum; these uncertainties are then propagated forward to derived parameters, including escape rates. For most of the data analyzed for the H corona, these formal

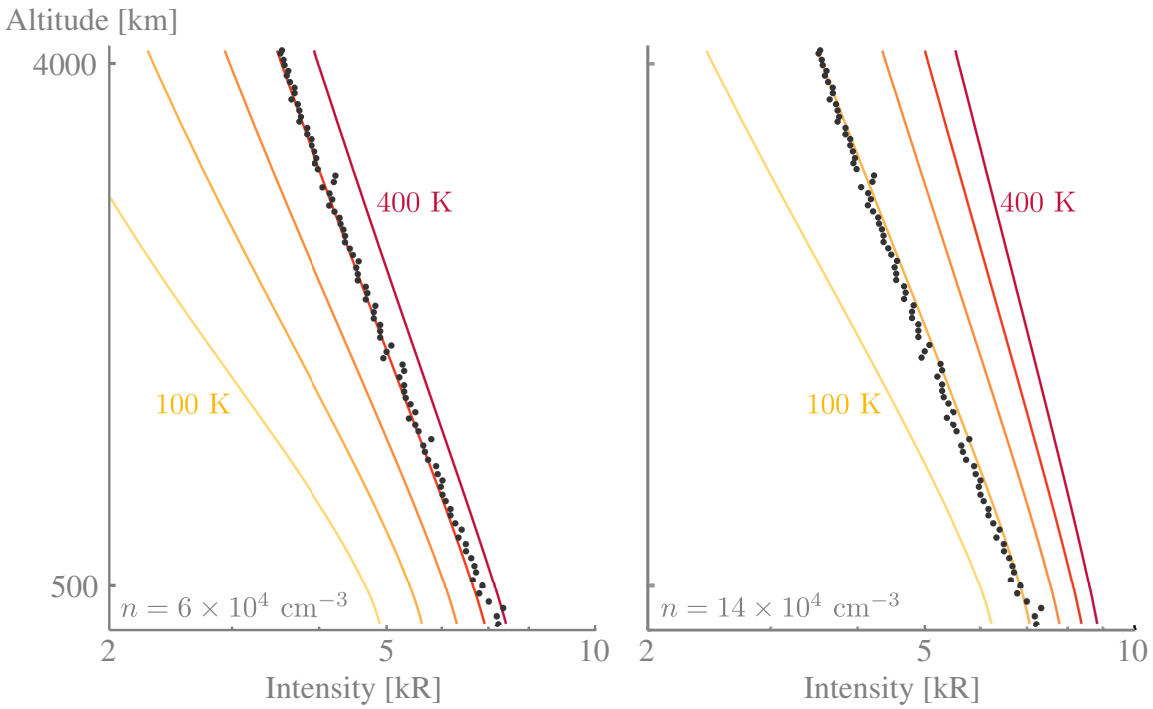

Figure 4.2: Data and model profiles compared. Black points show data as a function of altitude. Each panel shows computed profiles at a range of model temperatures for distinct exobase densities, indicated at lower left.

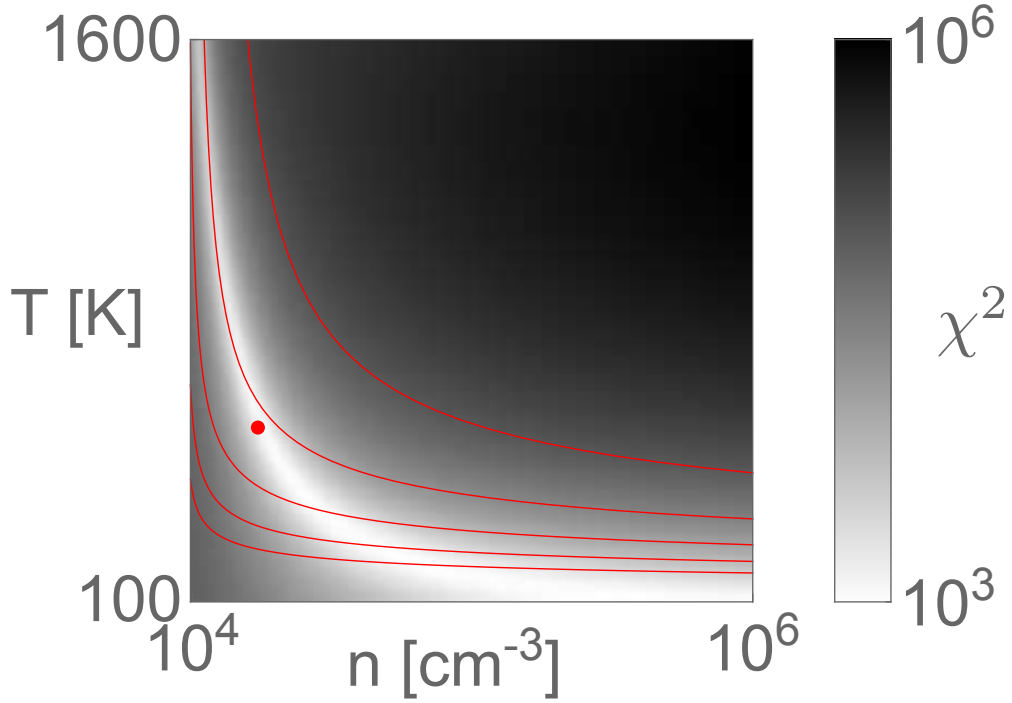

Figure 4.3: Model parameter space, including model-data chi-squared deviation (shading). Contours of constant escape rate shown in red, spaced geometrically in increments of $\sqrt{10}$. Point indicates function minimum.

uncertainties are not strictly valid, owing to the large values of the chi-squared statistic at the minimum, indicating that the uncertainties have been underestimated, the uncertainties are not Gaussian, or the model is incorrect. Given the excellent agreement of the model and the data throughout the SPICAM dataset, it is likely that the uncertainties are underestimated or non-Gaussian. While this means that the derived formal parameter uncertainties and those on derived quantities are strictly incorrect, they nevertheless serve as guidelines for the expected uncertainty. The minimum on the chi-squared surface depends only on its shape, so the best fit parameters still given the true minimum even when the uncertainties are poorly understood.

Selected profiles from the 2007 dataset and a range of model fits to the data are shown in Figure 4.4. At the time of the observations, Mars was experiencing late southern summer, moving away from perihelion on its orbital path around the Sun. Simultaneously, the lower atmosphere was experiencing the declining phase of a global dust storm. The corona experienced a uniform 50% decrease in brightness across the observations regardless of observation geometry, greatly exceeding the expected 20% decrease in coronal brightness expected from the orbital motion of Mars. This factor of two decrease in brightness from the beginning to the end of the observations indicates a substantial decrease in the inventory of hydrogen in the corona, independent of model assumptions. Because the corona is optically thick, a factor of two in brightness represents a larger change in the column density and therefore the escape rate of hydrogen.

The absolute magnitude of the change in the corona depends strongly on the exobase temperature. Because there is some controversy regarding the temperature of the H population (see Chapter 2), we fit the profiles using three temperatures: an unconstrained best fit, a constant 300 K (within the range of the Mariner temperature uncertainties), and a temperature extracted from the work of Forbes [Forbes et al., 2008], whose empirically-derived seasonally varying thermosphere temperatures track models of the upper atmosphere[1]. Unconstrained temperatures naturally do a better job of fitting the data, particularly at the beginning of the dataset when the intensities are

[1]As pointed out by Krasnopolsky (2010), the Forbes temperatures are a suspiciously good match to models, perhaps an unintentional consequence of using an atmosphere model as part of the temperature retrieval pipeline.

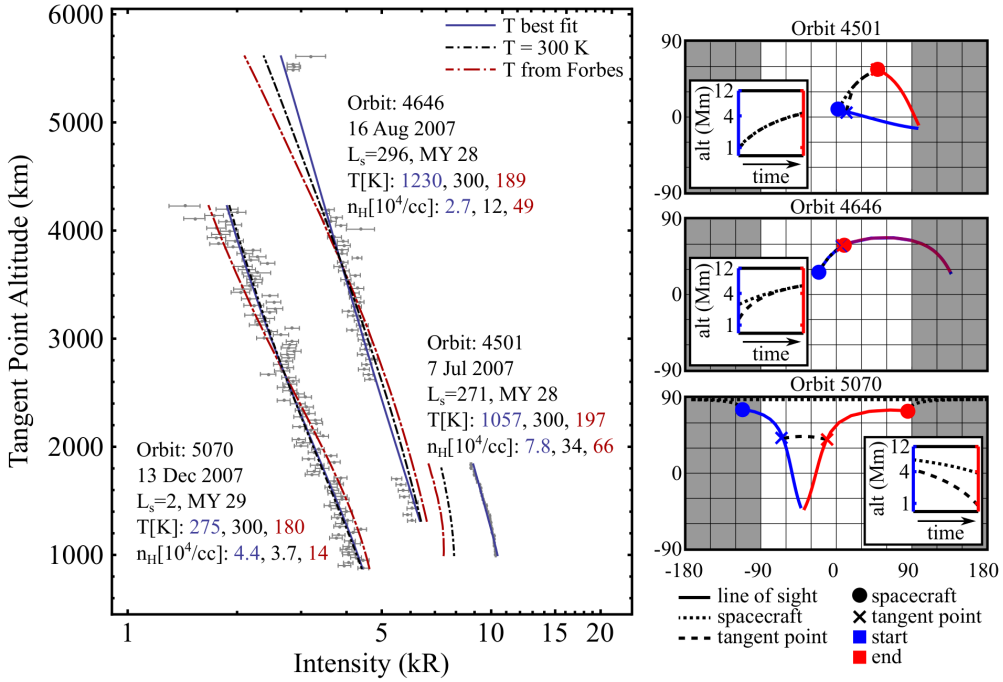

Figure 4.4: Example spacecraft data and model fits from 2007. (left) Observed brightness (gray points) and associated uncertainties for three observations. Curves represent best fit model output for three different temperature assumptions: unconstrained model temperature in the range 100-1600 K; fixed temperature of 300 K; and temperature from the empirical thermosphere model of Forbes et al. (2008). Observation metadata and best fit model parameters also indicated. Observations are in time sequence from right to left, demonstrating the decrease in hydrogen corona brightness observed in Fall 2007. (right) Geometry of each observation, including the location in solar coordinates and altitude in Mm = 10^6 m of the spacecraft (dot, dotted line) and tangent point (x, dashed line) along the line of sight as a function of time from beginning (blue) to end (red) of each observation.

higher and cannot be captured at all with the lower temperatures assumed.

Retrieved model parameters are summarized in Figure 4.5. Independent of exobase temperature, we observe a nearly uniform order of magnitude decrease in the escape flux of hydrogen at the exobase of Mars over six months in the fall of 2007. For the highest best-fit temperatures, the escape parameter λ approaches unity, so that the Jeans escape formula is not quantitatively accurate. If these temperatures indicate the true state of the atmosphere more sophisticated modeling must be undertaken to determine the absolute rate of escape.

For many of the best-fit temperature and 300 K retrievals, escape fluxes predicted by the Jeans escape are extremely high. These escape rates often exceed 3.7×10^8 atoms cm^{-2} s^{-1}, predicted by Zahnle [Zahnle et al., 2008] as the maximum possible escape rate. Zahnle's calculation assumes that escaping H is supplied to the exobase by diffusion of molecular hydrogen at the fixed mixing ratio measured by Krasnopolsky and Feldman [Krasnopolsky and Feldman, 2001]. Because the derived escape rates are so much larger than the rate of diffusive supply, the change in escape rates we observe must be due to a change in the density of hydrogen-bearing species in the thermospheric source region. This strongly suggests that either molecular hydrogen is much more concentrated in the Martian atmosphere than expected on the basis of measurements, or that a different species (e.g. water) must be capable of carrying H into the escape region.

Escape fluxes resulting from unconstrained fits indicate a factor of more than 100 decline in the escape rate of hydrogen from June to December of 2007. This decline is at least an order of magnitude, independent of assumptions made about the temperature, and well-correlated with lower atmospheric and seasonal drivers (Figure 4.6).

The change observed is well-correlated with the movement of Mars away from the Sun and with the decline in lower atmospheric dust opacity from the 2007 dust storm as measured by Smith with the Thermal Emission Imaging System on Mars Odyssey (THEMIS) [Smith, 2009]. Our escape rate variations are not correlated with fluctuations in the 10.7 cm radio flux (a solar activity proxy) or with the solar spectral irradiance measured by TIMED/SEE below 90 nm [Woods, 2005], the ionization threshold for CO_2, which is the major heat source for the thermosphere.

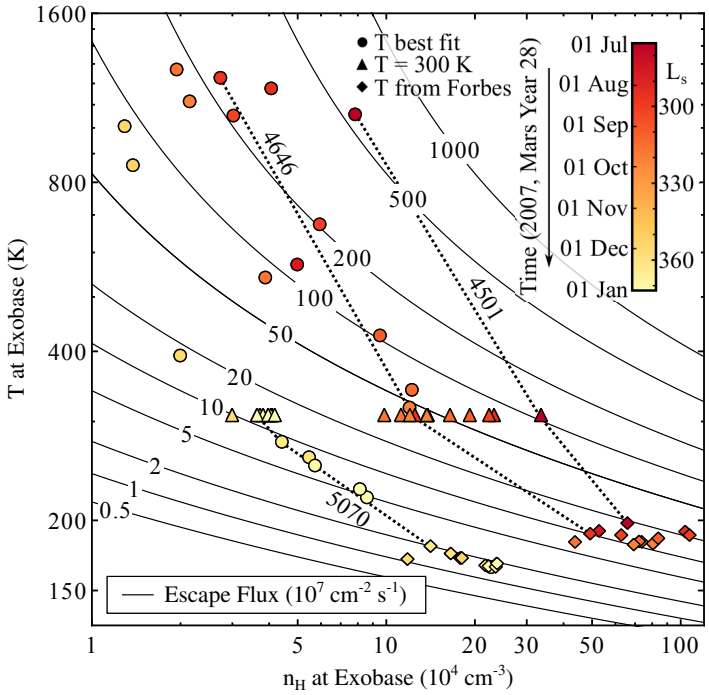

Figure 4.5: Best-fit temperature and density for 2007 observations. Parameters are shown for all twenty observations analyzed using three temperature assumptions, and are colored by time of observation. Contours give Jeans escape flux of hydrogen at the exobase. Dotted lines connect parameters fit to observations shown in Figure 4.4 for each temperature assumption, identified by orbit number. These lines demonstrate the anticorrelation of model fitted temperature and density.

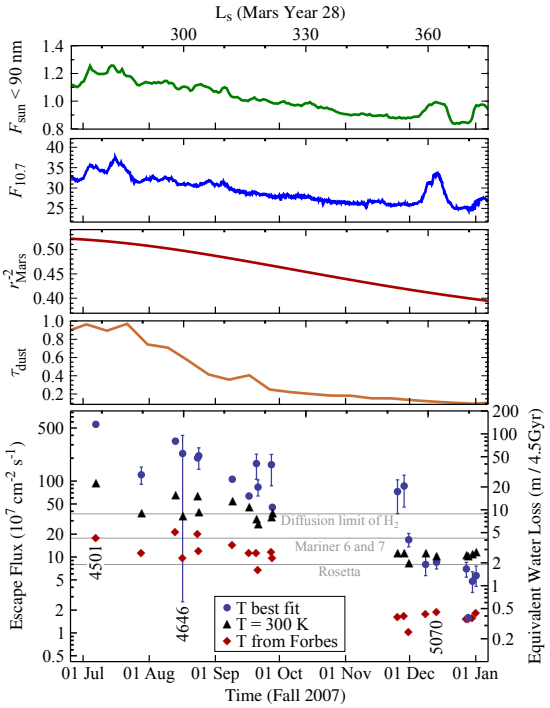

Figure 4.6: Derived H escape flux and potential explanatory parameters across Fall 2007. Bottom panel: H escape flux for all three temperature assumptions. Observations shown in Figure 4.4 are identified by orbit number. Right axis shows amount of water lost if the corresponding H escape flux were constant with time throughout Martian history. Error bars represent derived 95% uncertainties propagated from uncertainties in observed brightness. Where not shown, uncertainties are smaller than point size. Escape flux decline is nearly exponential with time, independent of temperature assumptions. Gray lines indicate three prior estimates of H escape flux. Other panels: potential explanatory parameters. From top: total solar flux less than 90 nm in units of W cm^{-2}; Solar decimetric radio flux (in 10^{-22} W m^{-2} Hz^{-1}); Inverse square of Mars-Sun distance in AU^{-2}; and optical depth of lower atmospheric dust measured by THEMIS. Correlation of escape flux with solar indices is due to distance-scaling of these indices to Mars. Decline of escape flux is well-correlated with Mars-Sun distance and lower atmospheric dust opacity but not with short-timescale solar forcing.

The escape rates observed in Fall 2007 encompass all prior estimates for H escape at Mars, indicating a smooth variation which tracks both season and dust abundance in the atmosphere. On the basis of the 2007 dataset alone, the unique cause of the variation cannot be determined, as the two potential forcing mechanisms are completely coincident. A broader study of the SPICAM dataset was undertaken to determine whether a unique cause could be determined.

4.2 SPICAM data processing

SPICAM divides their data by observation mode: nadir, limb, stellar occultation, and technical observations (referring to observations gathered to constrain the behavior of the detector rather than the behavior of Mars). We downloaded the entire SPICAM dataset from NASA's Planetary Data System and searched all limb-tagged observations, obtaining the range of pointing altitudes and the date of each observation. The results of this process are shown in Figure 4.7, which also displays the Mars solar longitude of the observations.

Due to the large density scale height of hydrogen at coronal temperatures ($\sim$ 900 km at a 200 km exobase and 300 K), observations which cover a large altitude range at high altitude are most useful for constraining the H corona. The full set of SPICAM limb observations was narrowed to those observations that cover an altitude range of at least 500km, with the upper altitude above 2000km (Figure 4.8).

Unfortunately, the useful observations cover the Martian year only sparsely, with the sampling of southern summer particularly poor. Southern summer observations occur almost completely in Fall 2007, the year of a global dust storm. Because southern summer is only sampled during a dust storm in 2007, determine the cause of the behavior observed then using the rest of the SPICAM dataset is difficult.

Data from high altitude, large altitude range observations were reduced from PDS level 0 ".dat" files following standard SPICAM wavelength and intensity calibration procedures, which are documented on the PDS. At the time when this work began, the calibrated level1a files now hosted on the PDS were unavailable. Wavelength calibration is less important for this work than for much

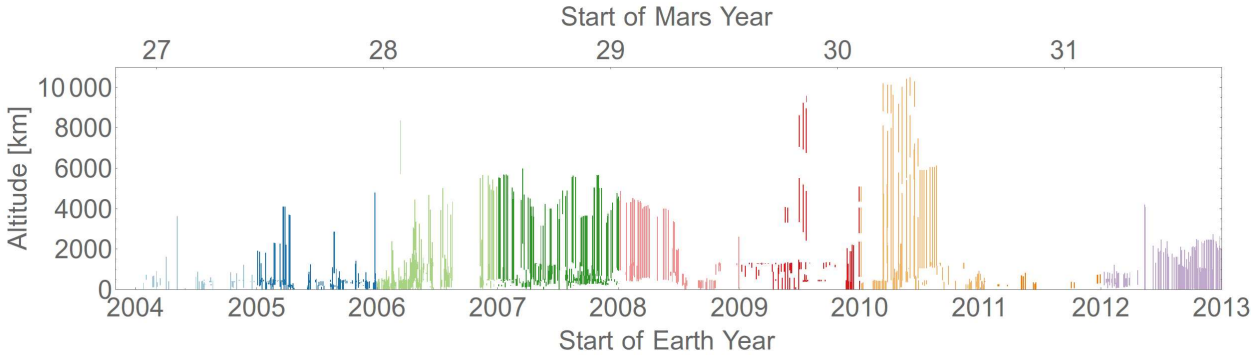

Figure 4.7: SPICAM data availability, as a function of pointing altitude and time. Colors indicate Earth year of observation.

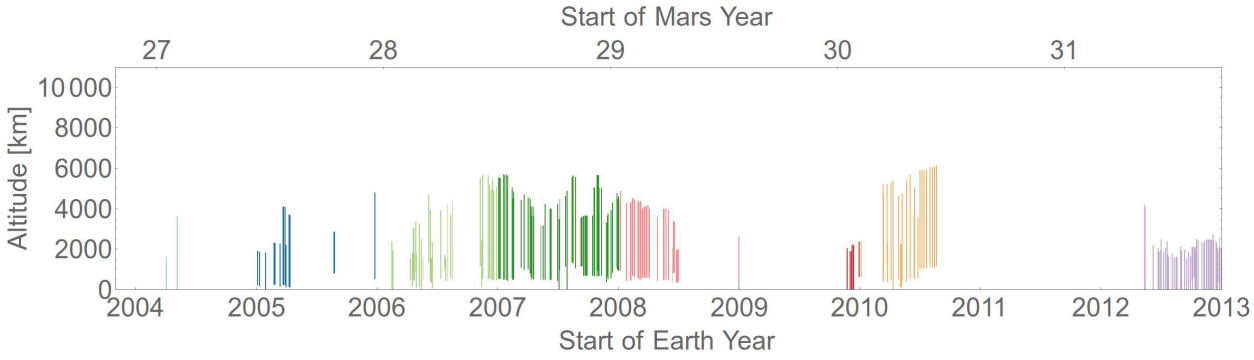

Figure 4.8: As above, for data that cover more than 500 km altitude and have a maximum altitude greater than 2000 km, useful for H coronal science. These data poorly sample the second half of the Martian year, with most observations covering southern summer made in 2007.

of the work done by SPICAM, as we target the brightest emission in the SPICAM FUV bandpass and are only interested in the intensity of this single line. Absolute intensity calibration is especially important for our work, however, for at least two reasons: (1) we propose to generate absolute escape rates of atomic H from the atmosphere of Mars, so that our escape rate uncertainty is inherently at least as large as that in the intensity calibration; and (2) the optically thick nature of the H corona, with typical $\tau \sim 1 - 10$, means that small changes in the absolute column brightness are associated with larger changes in the retrieved column density, with nonlinear effects on the density and temperature retrieved. Some discussion of the absolute calibration of SPICAM is therefore in order.

UV-bright stars were used to calibrate SPICAM during its cruise to Mars, first against reference measurements made by Hubble and later against absolute stellar measurements by SOHO/ SOLSTICE [Snow et al., 2013]. The SOLSTICE absolute calibration was performed at NIST using ultraviolet synchrotron light. SOLSTICE and Hubble agree within 10% on a set of stars observed by both experiments, and so SPICAM agrees with the SOLSTICE absolute calibration as well [Snow et al., 2013].

Stellar observations define the response of SPICAM to a point source, but the observations made at Mars fill the slit, requiring this point-source calibration to be extended to diffuse measurements. This was accomplished from first principles, using the solid angle each pixel subtends on the sky as a conversion factor. To verify the calibration, measurements of the interplanetary hydrogen were compared with STIS and found to agree, confirming that consistent geometrical factors had been used by each instrument to calibrate diffuse observations [Bertaux et al., 2006].

The instrument calibration at Lyman alpha can be checked for consistency with the model by introducing an additional free parameter into the fit that represents an absolute intensity scaling. This approach was taken by Chaufray [Chaufray et al., 2008], who found that the best fit to observations required that SPICAM intensities be scaled by a factor of 0.9, at the edge of his allowed 10% uncertainty in the absolute calbration. After validating the correction factor on the present dataset, this factor of 0.9 was adopted in the current work.

After selecting only large altitude range, high altitude observations from the SPICAM dataset, a total of 258 observations were available for constraining the H corona. These observations consist of H Lyman alpha intensity observed along a particular line of sight along the spacecraft orbit at one time across the 10-year dataset.

Both stray light and anomalous high-voltage detector noise plague the SPICAM data. For the current analysis, these phenomena were excluded from the analyzed dataset using the assumption that large, sharp excursions from a smooth radial profile were caused either by stray light or by detector high voltage problems. Each limb scan was checked by hand for the presence of stray light or detector noise, and scans with no credible Lyman alpha signal were discarded. This left just under fifty limb scans useful for constraining the H corona.

Each scan, consisting of typically thousands of integrations, was binned into approximately 100 bins. In each bin outliers were excluded, replacing all values more than three median absolute deviations from the median value with the median. This procedure effectively excluded large excursions in both the light and dark integrations where the profiles were characteristicly smooth, while only minimally affecting the distribution in regions with a large amount of noise. The assumption that there are no sharp excursions in H coronal profiles is a good one, as the density scale height of H at 200 km altitude is measured in hundreds of kilometers, with intensity scale heights even higher due to optical depth effects. In many cases, the SPICAM data are so noisy that even this outlier exclusion does not remove all of the artifacts; in these cases affected altitude ranges were identified and manually excluded from the data. We consider it unlikely that any real signal from the H corona could be masked by this exclusion process. A typical profile before and after outlier removal and averaging is shown in Figure 4.9.

4.3 Results for the entire SPICAM dataset

The methodology of the case study on 2007 data was extended over the entire SPICAM dataset. Some of the analysis done for the earlier study was not repeated for the complete dataset. In particular, the sensitivity analysis on the effect of exobase temperature determined that the

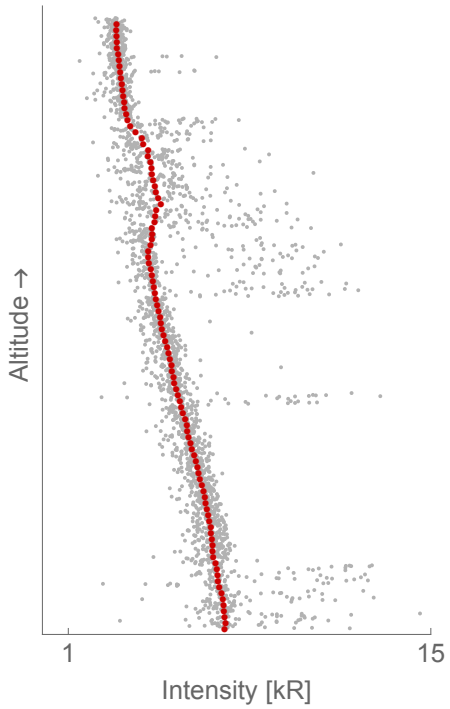

Figure 4.9: Example of a relatively clean SPICAM coronal profile. Data (in gray) are often affected by spurious high signal caused by malfunctioning detector electronics. Removing outliers before averaging results in a profile (red) which fixes some but not all of these problems, requiring manual exclusion of data in some altitude ranges.

temperature assumed for the exospheric retrieval did not significantly affect the relative escape rates of hydrogen across the dataset. While absolute escape rates are dependent on the temperature assumed, relative variations can be extracted without absolute knowledge of the temperature. A single temperature analysis is therefore capable of establishing the relative variability of the corona at different seasons, and we adopt this approach below.

SPICAM data and best fits for the analyzed dataset are shown in Figure 4.10, indicating the excellent agreement between the model and the data for these observations.

Forty-nine profiles are shown, representing much of the cleanest SPICAM data gathered on the Mars H corona. Many of the profiles exhibit characteristics of the high-voltage detector noise; these are visible as high-magnitude spikes in intensity, which were excluded from the model fitting. Some observations of the corona (for example, that from MEX orbit 7936)have intensities that increase with altitude; this counter-intuitive shape results from observations embedded in the corona and from shadowing and extinction effects resulting from the optically thick corona, underscoring the need for a full model to interpret the data. Both observed and modeled profiles exhibit high coronal intensities only in 2005 and 2007, when Mars was near southern summer solstice. In nearly every other case, observed coronal intensities are lower at all altitudes. The large decrease in observed intensities occurring in the corona in 2007 in southern summer is visible at the beginning of the top row and continuing across the second row. A similar trend is not evident anywhere else in the dataset, indicating that the corona is less variable at other seasons, when the planet is farther from the Sun and the atmosphere is less active.

Extracted model parameters are shown for each limb scan in Figure 4.11, where they are compared with historical observations. Most observations made during northern hemisphere summer, cluster in the temperature, density, and escape rate range expected on the basis of prior observations, $n_H \sim 10,000 - 50,000$ cm^{-3}, $T_H \sim 170 - 400$ K. Some observations, including those made in 2005 during early southern spring, and those made in 2007 during southern summer, show large excursions in temperature and therefore escape rate. The high best fit temperatures required to fit the coronal profiles observed in 2007 and 2005 approach or exceed the region where a Jeans formulation

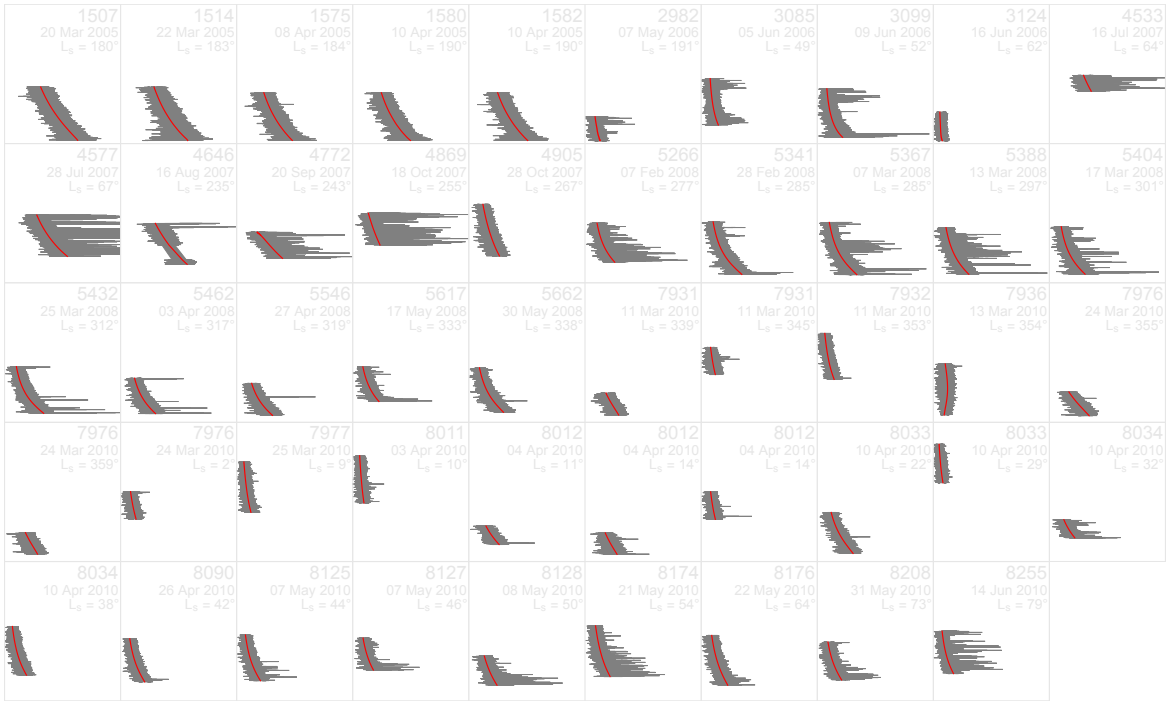

Figure 4.10: SPICAM data and model fits, identified by orbit number, date, and mars solar longitude. All plots share the same altitude and intensity range, from $0-10000$ km and $0-15$ kR. Gray shows 3σ range of reported SPICAM data. Red shows fitted model, which in most cases does a satisfactory job of fitting the data.

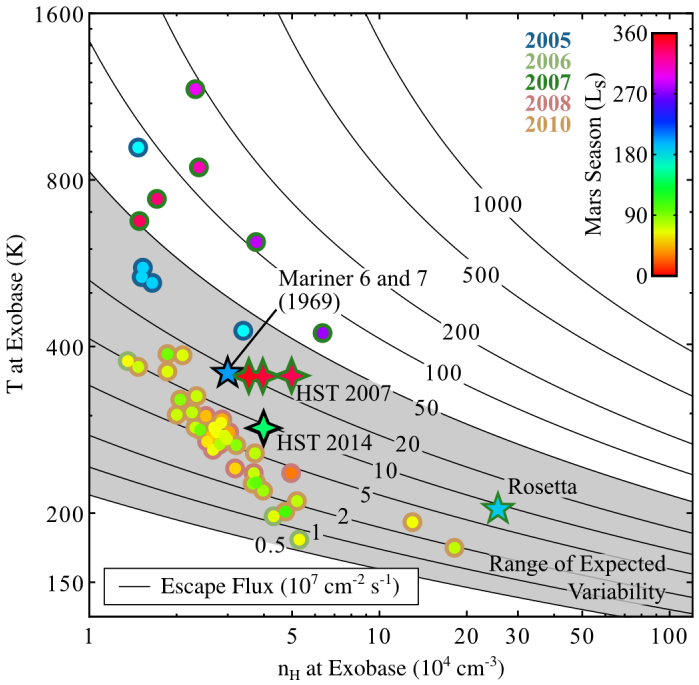

Figure 4.11: SPICAM retrieved model parameters. As Figure 4.5, with parameters shown only for best fit temperatures. Circles show SPICAM measurements, with inner color matched to Mars solar longitude and border identifying the year of the observations. Diamonds show HST observations of the corona with the same coding. Rosetta and Mariner observations also shown.

of is appropriate: if these represent true thermal temperatures then the hydrogen in the atmosphere at these times would be approaching a state of hydrodynamic blowoff, with a consequent large feedback on the lower atmosphere. It is unlikely that this is the true state of the atmosphere, but the high intensities observed in the coronal profiles demand temperatures this high for a satisfactory fit. The temperatures retrieved are reminiscent of the hot hydrogen temperature discovered at Venus, but both the signature and the source of a similar component at Mars is difficult to reconcile with the present state of knowledge about the atmosphere. As discussed in Chapter 2, the low gravity of the planet masks any hot hydrogen signal under the bright thermal corona. In addition, models of the atmosphere incorporating known ionospheric and solar wind physics struggle to produce a substantial hot hydrogen component [Nagy et al., 1990]. Without independent measurements of the H temperature or extremely high altitude measurements of the corona, the confusion over these temperatures may persist indefinitely.

The shape of the ensemble of all best fit parameters is reminiscent of the degeneracy present in the chi-squared parameter space for a single fit (Figure 4.3), making it tempting to incorrectly conclude that there is no real variation in escape rates. While many observations from northern summer fall along nearly identical chi-squared tracks and may all be consistent within the uncertainties in brightness, observations from 2005 and Fall 2007 demonstrate a real change in the state of the corona. This is apparent in Figure 4.5, which shows a range of best-fit densities at different assumed exobase temperatures, including the best-fit temperature shown here. The highest escape rates fall on a separate chi-squared track than the majority of observations from the SPICAM dataset, and are inconsistent with measurements at these lower escape fluxes, indicating that the corona really was different during these observations. The likely underestimation of SPICAM uncertainties or their non-Gaussian nature derived from detector high-voltage fluctuations makes it difficult to establish this with certainty using the formal parameter uncertainties: more sophisticated Monte Carlo parameter fitting techniques must be brought to bear on this dataset to determine whether statistically credible variations in the corona are present during northern summer.

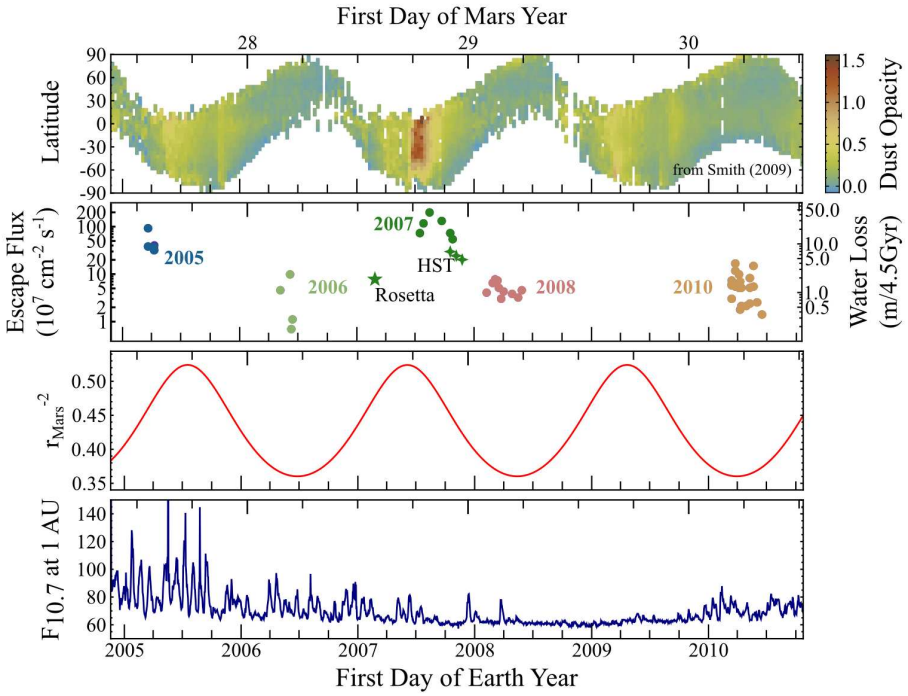

Figure 4.12: SPICAM-derived escape rates and potential explanatory parameters as a function of time. Escape rates are shown in the second panel from the top, in terms of escape flux at the exobase and integrated water loss assuming a constant escape rate. HST and Rosetta retrievals are also shown. Bracketing the escape rates are two potential controlling parameters. Top panel shows the zonal mean dust retrievals as a function of latitude from Smith et al. (2009), with the retrieval area modulated by the orbit of Mars Odyssey. Third panel shows the inverse-square of Mars-Sun distance. Bottom panel shows solar decametric flux $F_{10.7}$ measured at Earth, an indicator of solar activity. The 2007 observations occurred near perihelion during southern summer and a global dust storm.

Figure 4.12 shows potential explanatory parameters for the changes observed. Most escape rates obtained are low, with elevated escape in 2005 and 2007. The 2007 observations by SPICAM and HST coincide with southern summer during a dust storm, a time of high near-surface temperatures induced by dust warming and consequent intense mixing of the lower atmosphere [Zurek et al., 1992]. This greater mixing evidently results in transport of H-bearing species to the middle and upper atmosphere, enhancing H escape. This lower atomspheric effect complements the upper atmospheric warming expected at the same times due to the enhanced EUV flux impinging on the upper atmosphere as a result of Martian perihelion. A similar, though smaller enhancement in escape rates is seen in 2005 during the approach to southern summer, during the declining phase of the Solar Cycle 23. The difference in lower atomspheric dust content and solar cycle between 2005 and 2007 makes a direct comparison problematic, although the similar Mars-Sun distance and escape rate during 2005 and the end of the 2007 measurements suggests a seasonal dependence. Interpretation of the change as seasonal is complicated by the Rosetta measurement in early 2007, at the same phase of the Martian year as the SPICAM 2005 measurements.

4.4 Interpretation

The escape rates presented in this work span five years, cataloging the brightness of the Martian corona across a longer timespan than any previous investigation of the corona, with better sampling across the timespan reported than any other set of observations. These measurements indicate that the H corona is highly variable as a function of time, influenced by Martian season and solar flux, with dust storms potentially enhancing the transport of H from the lower to the upper atmosphere and driving escape. The large range of escape rates derived here span two orders of magnitude. This stands in contrast to modeling studies of the history of H escape, which predict near-constant escape rates resulting from a long-lived molecular hydrogen buffer [Lammer et al., 2003, 2012, Zahnle et al., 2008].

This work calls into question the classical hypothesis that the H escape rate is controlled by and closely tracks the O escape rate over geologic time [Parkinson and Hunten, 1972, McElroy, 1972].

In 2007 large changes in the H inventory of the exosphere are best fit by a factor of $50-100$ increase in the H escape rate. This increase is not coincident with excursions in the solar extreme ultraviolet flux sufficient to enhance O escape by the same amount. Measurement of the differential escape of these species at the times of enhanced H escape would be extremely valuable. However, the large amount of scattered light and detector noise in the SPICAM observation makes a direct comparison of H and O escape over the time span of our analysis is difficult. Simultaneous measurement of H and O escape will be performed by instruments on MAVEN, addressing the question of stoichiometric escape that underpins so many attempts to reconstruct the history of Martian water loss.

Our measurements strongly suggest that water, not molecular hydrogen, is the principal carrier of water to the upper atmosphere during times of enhanced escape. Both the magnitude and the timing of the H enhancement are suggestive: water is more abundant than H_2 in the atmosphere by a factor of at least 100, and could supply the large enhancement we observe if it is preferentially carried to the upper atmosphere during enhanced escape periods. Large escape rates are principally observed in southern summer, a time of greater insolation and atmospheric mixing, particularly as a result of the global dust storm in 2007. Challenging this conclusion are the measurements made by Mariner 6 and 7 and Rosetta, which according to this explanation should have seen large escape rates, but did not. Mariner 9 observed the H corona during the large dust storm of 1971, but an analysis of the H corona independent of the work performed on Mariner 6 and 7 has never been performed.

If water is the major carrier of H to the upper atmosphere at times of greater water abundance and atmospheric mixing, this has large implications for an early wet Mars, which by definition would have had a much larger water abundance at high altitudes. While our derived escape rates do not remove a significant fraction of the water column over the course of our observations, the integrated escape rate implied by our largest measurement implies a loss of 50 m over Martian history, a substantial fraction of the likely total. Keeping in mind that the atmosphere today is likely much drier than it was on average in the past, this upper limit from our present-day measurements is likely to be near the lower limit of the total water lost by Mars to space.

Chapter 5

Photochemistry

The large escape rates and variability found in SPICAM data analysis suggest that a diffusion-limited H_2 source for the escaping hydrogen is insufficient. Water provides a potential additional source for escaping H, and in early planning for the Mariner 9 UV spectrometer it was suggested that seasonal interchange of water between the polar caps and the atmosphere might provide a significant source for escaping H [Hord et al., 1970]. Soon afterward, early models of the Martian atmosphere found that low atmospheric temperature at altitude trapped water too close to the surface for it to provide a significant direct source for H in the upper atmosphere [Hunten and McElroy, 1970]. The conclusion was that H escaping from the atmosphere was extremely well buffered by long-lived molecular hydrogen, which is light and volatile enough to escape the cold trap and penetrate into the upper atmosphere. Contradicting these models, water has recently been discovered at high altitudes through SPICAM/IR observations made in solar occultation. These measurements, described in detail by Maltagliati [Maltagliati et al., 2013], demonstrate the existence of water vapor at altitudes between 40-100km, inconsistent with current general circulation models of the atmosphere and in some cases above the saturation vapor pressure for water (Figure 5.1).

Prior to these observations, most models of the Mars atmosphere assumed that water vapor would instantly condense if it reached saturation, at altitudes varying between $15 - 25$ km with occasional excursions as high as 50 km during dust storms [Jakosky, 1985]. At Earth, water vapor is often found in supersaturation in the upper troposphere [Gettelman et al., 2006]; finding supersaturation at Mars extends the common situation in the terrestrial atmosphere to another planet. The

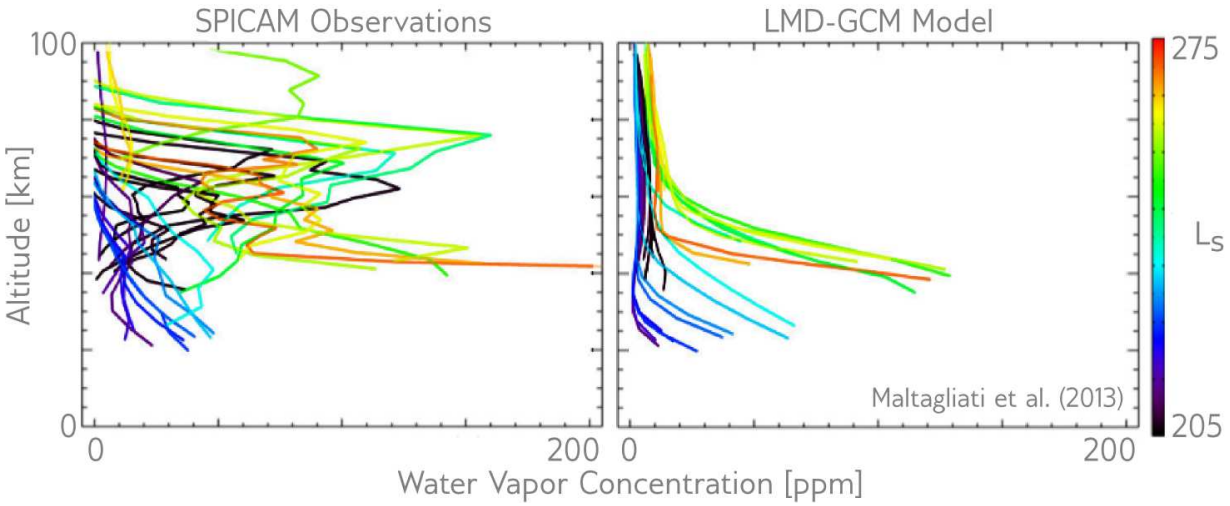

Figure 5.1: Water vapor observations of Maltagliati. SPICAM observations of the Southern hemisphere show enhanced and in some cases supersaturated water vapor in Southern hemisphere summer ($L_s \sim 200 - 270$), but the Laboratoire de Météorologie Dynamique General Circulation Model (LMD-GCM) does not.

supersaturation ratios observed at Mars (1-10) often greatly exceed those found at Earth (1-1.2): evidently condensation at Mars is more effectively suppressed. With a more detailed microphysical parameterization of cloud formation, the Laboratoire de Météorologie Dynamique General Circulation Model (LMD-GCM) forms high altitude water layers comparable to those found by SPICAM [Navarro et al., 2014], but the extent and prevalence of these layers is parameterization dependent.

One mechanism capable of rapidly producing high altitude water layers is localized heating of dust. In a modeling study by Spiga [Spiga et al., 2013], concentrated dust is lofted to high altitudes as a result of its increased opacity, which allows it to absorb sunlight and covert it to heat. The dust expands and rises, resulting in a feedback loop that drives dust plumes upward at several meters per second. This feedback mechanism has been proposed as the source of SPICAM-observed deteched dust layers [Heavens et al., 2014] in the $50-60$ km region of the atmosphere. It is natural to suppose that these dust layers carry water with them as they rise, providing a pathway for water to reach the middle atmosphere.

To determine whether the SPICAM/IR observations are consistent with SPICAM/UV observations of enhanced atmospheric escape, I performed a photochemical modeling study of H production and transport resulting from these high altitude water layers.

5.1 Model description

A completely new 1D time-dependent photochemical model was built for the purpose of modeling the transport of H-bearing species to the upper atmosphere. In the model, the continuity equation

$$\frac{\partial n}{\partial t} + \frac{\partial \Phi}{\partial z} = P - L$$

is solved for fourteen species using operator splitting, implicit finite difference transport, and first-order Gear chemistry. The methods used are standard, and thoroughly described by Jacobson [Jacobson, 2005]. Fluxes are computed at each timestep using the same diffusion equation as is

used in the coronal model:

$$\Phi = -(D+K)\frac{dn}{dr} - \left[D\left(\frac{1}{H} + \frac{1+\alpha_T}{T}\frac{dT}{dr}\right) + K\left(\frac{1}{H_a} + \frac{1}{T}\frac{dT}{dr}\right)\right] n,$$

with definitions as given above in Chapter 3. The production and loss operators P and L resulting from the chemical reaction network are computed as analytic expressions in an initialization step and then used to update densities at each timestep using Newton's method and the analytic network Jacobian, also computed during initialization. Species evolution is modeled using the absolute density of each constituient, rather than with mixing fraction. Each species is tracked on an altitude grid from 0 to 200 km, with a spacing of 5 km.

The model is implemented in Julia [Bezanson et al., 2014], a fast language with metaprogramming features. The chemical differential equations and Jacobian of the reaction network are programmatically generated at runtime from an arbitrary chemical reaction network. Because of this, the model does not depend on the Kinetic Pre-Processor [Damian et al., 2002], a package which is widely used for programmatic generation of chemical reaction network analysis code. The Julia code written for this thesis is comparable in speed to state-of-the-art photochemical models implemented in FORTRAN, being slower by a factor of only 1.5-2 despite the much higher level of the language in use. The entire photochemical model is less than 1000 lines long, with most of the space occupied by code specifying the reaction network and loading photochemical cross-sections from file.

Reaction rates, cross-sections, and quantum yields were drawn from a wide cross-section of the photochemical literature, based on work performed by Justin Deighan [Deighan, 2012]. Most of these data are compiled by JPL [Sander et al., 2011], but some small differences arising from more accurate measurements or calculations not reviewed there were incorporated. These new rates and cross-sections do not have a significant impact on the atmospheric chemistry. Similarly, a recent proposal [Lu et al., 2014] that CO_2 photodissociation can directly produce O_2 has a negligible effect on the chemistry of the Mars atmosphere, because the quantum yield of this pathway is near 5% and the wavelengths required to access it are shorter than 112 nm.

For some simple molecular species such as H_2, photodissociation cross sections were taken from `http://phidrates.space.swri.edu` [Huebner and Mukherjee, 2015], as Sander does not tabulate cross sections for these species. The reaction network and reaction rates are listed in Table 5.1.

Boundary conditions are summarized in Table 5.2. For those species not listed, a zero-flux boundary condition was assumed at the top and bottom boundary of the model. At the top of the atmosphere, the only species with an escaping boundary condition are O and O_2, assumed to escape at a fixed rate as a result of near-constant photochemical escape, and hydrogen, with a fixed velocity boundary condition corresponding to the effusion velocity of Jeans escape at the exobase assuming a 300K temperature (see chapter 3).

Important model inputs are shown in Figure 5.2 and discussed below. The temperature of the atmosphere is defined with a spline fit to the surface temperature (211K), adiabatic lapse rate of the troposphere (-1.4 K km^{-1}), altitude of the tropopause (50 km), and lower boundary of the isothermal exosphere (300 K at 200 km).

The Eddy and molecular diffusion profiles were taken from Krasnopolsky [Krasnopolsky, 1993] and Hunten [Hunten, 1973], respectively. No adjustments to the eddy or binary diffusion profiles were made.

The input water profile as a function of altitude is the major parameter explored by this study, and so is not self consistently computed with the other species, but acts as an input on their concentration. Our standard water profile is well-mixed in the lower troposphere, follows the saturation vapor pressure profile [Washburn, 1924] as a function of temperature in the upper atmosphere to a minimum concentration, and is fixed to this minimum value at higher altitudes. Total precipitable water vapor in the standard model case is 6.94 μm.

In the current work, we do not self-consistenly model the ionosphere, but adopt fixed ionospheric concentrations from the work of Matta [Matta et al., 2013], the most important of which (for the purpose of H chemistry) is CO_2^+, which converts molecular H_2 to atomic H in the ionosphere. The large differences in the topside ionosphere composition found by Matta as a result of different molecular hydrogen concentrations do not affect our main conclusions, as we are interested

Table 5.1: Reaction network used in the present work.

Reaction			Rate
$CO_2 + h\nu$	$\rightarrow$	$CO + O$	computed
	$\rightarrow$	$CO + O(^1D)$	
$O_2 + h\nu$	$\rightarrow$	$O + O$	
	$\rightarrow$	$O + O(^1D)$	
$O_3 + h\nu$	$\rightarrow$	$O_2 + O$	
	$\rightarrow$	$O_2 + O(^1D)$	
	$\rightarrow$	$O + O + O$	
$H_2 + h\nu$	$\rightarrow$	$H + H$	
$OH + h\nu$	$\rightarrow$	$O + H$	
	$\rightarrow$	$O(^1D) + H$	
$HO_2 + h\nu$	$\rightarrow$	$OH + O$	
$H_2O + h\nu$	$\rightarrow$	$H + OH$	
	$\rightarrow$	$H_2 + O(^1D)$	
	$\rightarrow$	$H + H + O$	
$H_2O_2 + h\nu$	$\rightarrow$	$OH + OH$	
	$\rightarrow$	$HO_2 + H$	
	$\rightarrow$	$H_2O + O(^1D)$	
$O + O + M$	$\rightarrow$	$O_2 + M$	$1.8 \times 3.0 \times 10^{-33}(300/T)^{3.25}$
$O + O_2 + N_2$	$\rightarrow$	$O_3 + N_2$	$5 \times 10^{-35}\exp(724/T)$
$O + O_2 + CO_2$	$\rightarrow$	$O_3 + CO_2$	$2.5 \times 6.0 \times 10^{-34}(300/T)^{2.4}$
$O + O_3$	$\rightarrow$	$O_2 + O_2$	$8.0 \times 10^{-12}\exp(-2060/T)$
$O + CO + M$	$\rightarrow$	$CO_2 + M$	$2.2 \times 10^{-33}\exp(-1780/T)$
$O(^1D) + O_2$	$\rightarrow$	$O + O_2$	$3.2 \times 10^{-11}\exp(70/T)$
$O(^1D) + O_3$	$\rightarrow$	$O_2 + O_2$	1.2×10^{-10}
	$\rightarrow$	$O + O + O_2$	1.2×10^{-10}
$O(^1D) + H_2$	$\rightarrow$	$H + OH$	1.2×10^{-10}
$O(^1D) + CO_2$	$\rightarrow$	$O + CO_2$	$7.5 \times 10^{-11}\exp(115/T)$
$O(^1D) + H_2O$	$\rightarrow$	$OH + OH$	$1.63 \times 10^{-10}\exp(60/T)$
$H_2 + O$	$\rightarrow$	$OH + H$	$6.34 \times 10^{-12}\exp(-4000/T)$
$OH + H_2$	$\rightarrow$	$H_2O + H$	$9.01 \times 10^{-13}\exp(-1526/T)$
$H + H + CO_2$	$\rightarrow$	$H_2 + CO_2$	$1.6 \times 10^{-32}(298/T)^{2.27}$
$H + OH + CO_2$	$\rightarrow$	$H_2O + CO_2$	$1.9 \times 6.8 \times 10^{-31}(300/T)^2$
$H + HO_2$	$\rightarrow$	$OH + OH$	7.2×10^{-11}
	$\rightarrow$	$H_2O + O(^1D)$	1.6×10^{-12}
	$\rightarrow$	$H_2 + O_2$	6.9×10^{-12}
$H + H_2O_2$	$\rightarrow$	$HO_2 + H_2$	$2.8 \times 10^{-12}\exp(-1890/T)$
	$\rightarrow$	$H_2O + OH$	$1.7 \times 10^{-11}\exp(-1800/T)$
$H + O_2$	$\rightarrow$	HO_2	$k_0 = 2.0 \times 4.4 \times 10^{-32}(T/300)^{-1.3}$
			$k_\infty = 7.5 \times 10^{-11}(T/300)^{0.2}$
$H + O_3$	$\rightarrow$	$OH + O_2$	$1.4 \times 10^{-10}\exp(-470/T)$
$O + OH$	$\rightarrow$	$O_2 + H$	$1.8 \times 10^{-11}\exp(180/T)$
$O + HO_2$	$\rightarrow$	$OH + O_2$	$3.0 \times -11\exp(200/T)$
$O + H_2O_2$	$\rightarrow$	$OH + HO_2$	$1.4 \times 10^{-12}\exp(-2000/T)$
$OH + OH$	$\rightarrow$	$H_2O + O$	1.8×10^{-12}
	$\rightarrow$	H_2O_2	$k_0 = 1.3 \times 6.9 \times 10^{-31}(T/300^{-1.0}$
			$k_\infty = 2.6 \times 10^{-11}$
$OH + O_3$	$\rightarrow$	$HO_2 + O_2$	$1.7 \times 10^{-12}\exp(-940/T)$
$OH + HO_2$	$\rightarrow$	$H_2O + O_2$	$4.8 \times 10^{-11}\exp(250/T)$
$OH + H_2O_2$	$\rightarrow$	$H_2O + HO_2$	1.8×10^{-12}
$HO_2 + O_3$	$\rightarrow$	$OH + O_2 + O_2$	$1.0 \times 10^{-14}\exp(-490/T)$
$HO_2 + HO_2$	$\rightarrow$	$H_2O_2 + O_2$	$3.0 \times 10^{-13}\exp(460/T)$
$HO_2 + HO_2 + M$	$\rightarrow$	$H_2O_2 + O_2 + M$	$2 \times 2.1 \times 10^{-33}\exp(920/T)$
$CO + OH$	$\rightarrow$	$CO_2 + H$	$k_0 = 1.5 \times 10^{-13}(T/300)^{0.6}$
			$k_\infty = 2.1 \times 10^{9}(T/300)^{6.1}$
	$\rightarrow$	$HOCO$	$k_0 = 5.9 \times 10^{-33}(T/300)^{-1.4}$
			$k_\infty = 1.1 \times 10^{-12}(T/300)^{1.3}$
$HOCO + O_2$	$\rightarrow$	$HO_2 + CO_2$	2.0×10^{-12}
$CO_2^+ + H_2$	$\rightarrow$	$CO_2 + H + H$	8.7×10^{-10}

Table 5.2: Model boundary conditions. Units: $[n] = \mathrm{cm}^{-3}$, $[\phi] = \mathrm{cm}^{-2}\ \mathrm{s}^{-1}$, $[v = \phi/n] = \mathrm{cm}\ \mathrm{s}^{-1}$.

Boundary	Species	Condition
lower	CO_2	$n = 2.1 \times 10^{17}$
	Ar	$n = 4.2 \times 10^{15}$
	N_2	$n = 2.1 \times 10^{17}$
upper	O	$\phi = 1.2 \times 10^{8}$
	H_2	$v = 3.4 \times 10^{1}$
	H	$v = 3.1 \times 10^{3}$

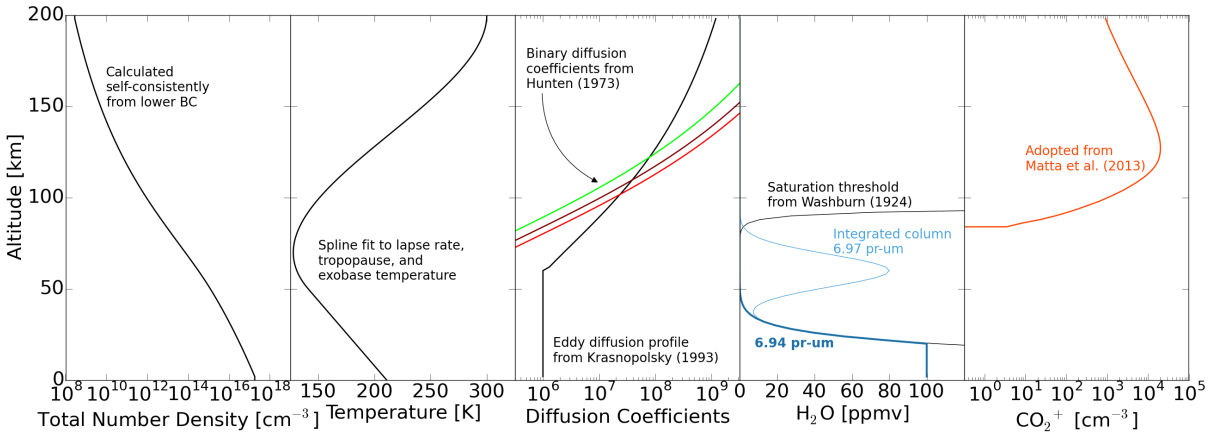

Figure 5.2: Overview of major model inputs.

in neutral escape at 200km, where the ionospheric variability is small.

The solar UV flux is taken from the Whole Helosphere Interval [Woods et al., 2009], which is accurate for quiet sun conditions, and scaled to the distance of Mars. The solar actinic flux is self-consistently attenuated from the top of the atmosphere to the surface, with diffuse scattering assumed negligible.

To validate the performance of the model, we used as initial conditions for the species profiles identical in shape to the neutral CO_2 profile, but scaled by the bulk atmospheric abundance found in a previous study by Nair [Nair et al., 1994]. After running the model for ten years with a timestep of one hour, the resulting atmosphere (Figure 5.3) replicates prior work on the photochemistry of the Martian atmosphere, establishing the stability of the model over the time range of interest to this study (months-years).

Having validated the model under standard water conditions, we performed a series of numerical experiments to determine the sensitivity of the atmosphere to the water vapor profile assumed. Prior work by Krasnopolsky [Krasnopolsky, 2006] explored the seasonal effect of a changing water column, but did not consider large, potentially supersaturated concentrations of water at high altitude, the target of our study. To explore the effect of high altitude water layers, we modified our fixed standard water profile through the addition of a Gaussian parcel of water at a variable relative concentration and altitude. All parcels had a fixed one sigma width of 12.5 km, chosen to roughly match Maltagliati's observed profiles. A comparison of observed and input water vapor profiles is shown in Figure 5.4.

5.2 Time-evolution

First, we characterized the equilibrium response of the atmosphere to a Gaussian parcel of water vapor at an altitude of 60 km and a concentration of 80 ppm, similar to concentrations observed by Maltagliati on MEX Orbit 6857, which observed Southern mid-latitudes in summer ($L_s \approx 250$). Running the enhanced water vapor profile to photochemical equilibrium, we obtained the atmosphere shown in Figure 5.5. The absolute enhancement in total atmospheric water from

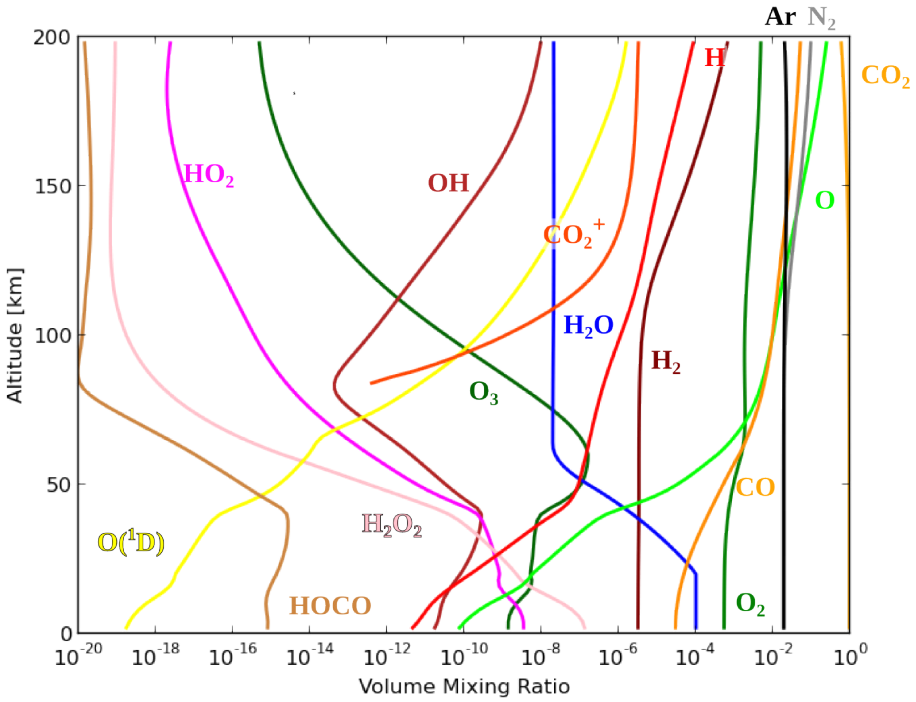

Figure 5.3: Photochemical model standard water case output. All model species are shown as a fraction of the total atmosphere at all model altitudes. The model reproduces the well-known photochemistry of the Mars atmosphere for a standard water profile. Long lived species such as H_2 have constant mixing ratios in the well-mixed lower atmosphere and follow their own scale height above the homopause.

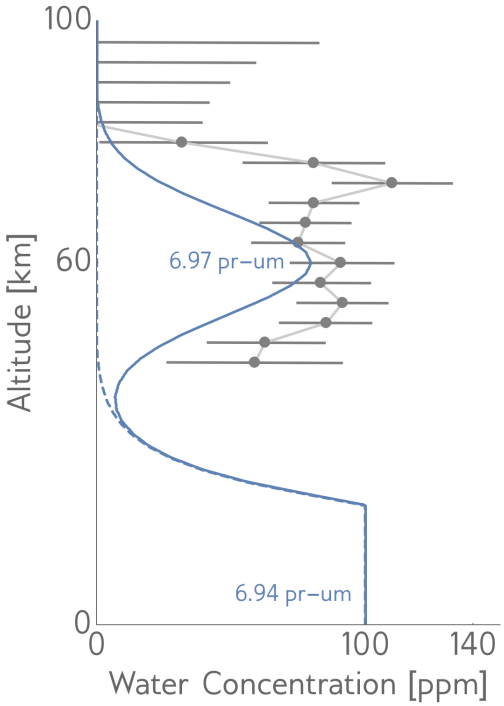

Figure 5.4: Comparison of observed and input water profiles. Gray points show SPICAM observations from Maltagliati. Blue curves show the model water vapor profile for standard photochemistry (dashed) and the high-altitude water case (solid).

our 6.94 pr-μm standard water profile to our 6.97 pr-μm high-altitude enhanced water profile is 0.03 precipitable microns, a change of less than one percent. Nevertheless, the water-enhanced atmosphere shows several notable differences from the standard atmosphere, discussed below in the context of our time-dependent experiments.

To determine the timescale of the atmospheric response to the introduction or removal of this high-altitude parcel, we switched the assumed water vapor profiles in our standard and high-water equilibrium atmospheres, and tracked the evolution of the atmosphere over the subsequent ten years. The results are shown for important H- and O-bearing species in Figure 5.6.

Upon introduction of the parcel, a large increase in the hydrogen concentration develops at the altitude of the water enhancement as a result of local photodissociation. Over the next thirty days, the extra hydrogen makes its way to the upper atmosphere. Meanwhile, enhanced CO_2 recombination occurs at the altitude of the water bulge, decreasing the O and CO concentrations there and producing an excess of molecular hydrogen, the byproduct of the odd H cycle. After 10 years, the hydrogen species come into equilibrium throughout the atmosphere, with molecular hydrogen enhanced relative to its initial state. By the time equilibrium is reached, the H density at 200 km has increased by a factor of fifty, which results in a factor of 50 increase in H escape resulting from the new water profile. Most of this enhancement occurs in the first fifty days as a result of the direct production of H from water at high altitude, with only a small increase between 30 days and 10 years after introduction of the water layer due to the increase in the molecular hydrogen concentration. By contrast, the atomic and molecular oxygen concentrations throughout the atmosphere are not as strongly affected at any time or altitude other than the location of the water escape, so that the increase in H escape is not balanced by a corresponding increase in O escape, at least within the ten-year timespan reported on here. Previous studies, including that by Nair [Nair et al., 1994], indicate that O_2 equilibrates much more slowly, acting to balance the absolute escape rates of H and O on geologic timescales (Figure 5.7).

The reverse process of removing the water enhancement at altitude restores the initial conditions of the standard water equilibrium atmosphere on the same months-long timescale, resulting

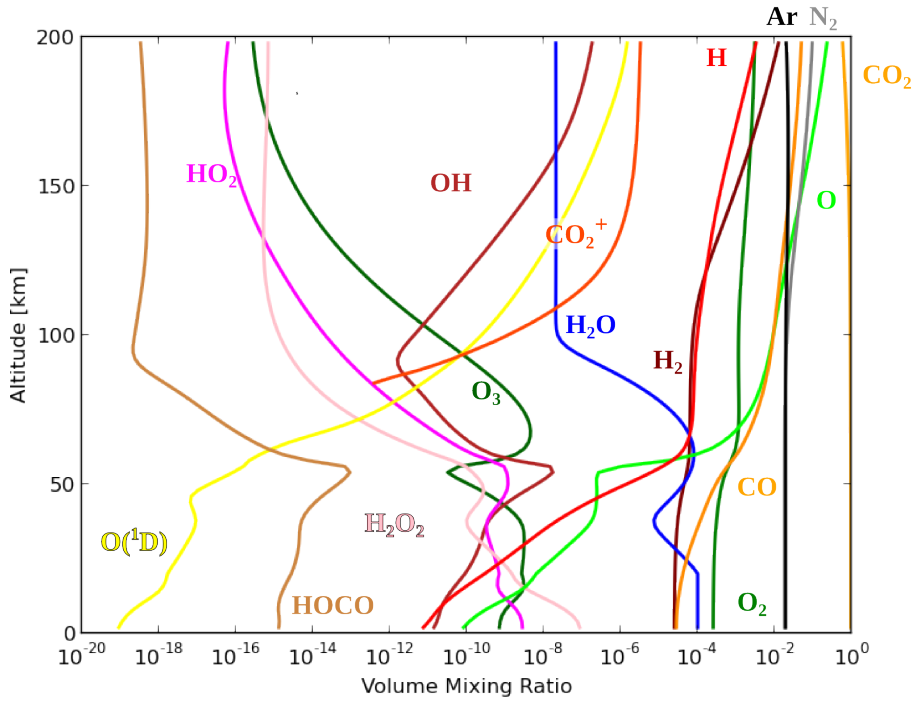

Figure 5.5: Photochemical model high water case output. With the introduction of a detached water layer (blue), catalysis of CO_2 recombination at high altitude is enhanced, as demonstrated by a higher peak in the intermediate recombination species HOCO. Compared to the standard model shown in Figure 5.3, the abundance of atomic and molecular hydrogen resulting from water breakdown increases throughout the atmosphere. At the upper boundary, the H mixing fraction in the atmosphere has increased by over an order of magnitude, with a consequent enhancement of H escape. In the middle atmosphere, O and O_3 are depleted relative to the standard water case, while the odd hydrogen species OH and HO_2 are enhanced.

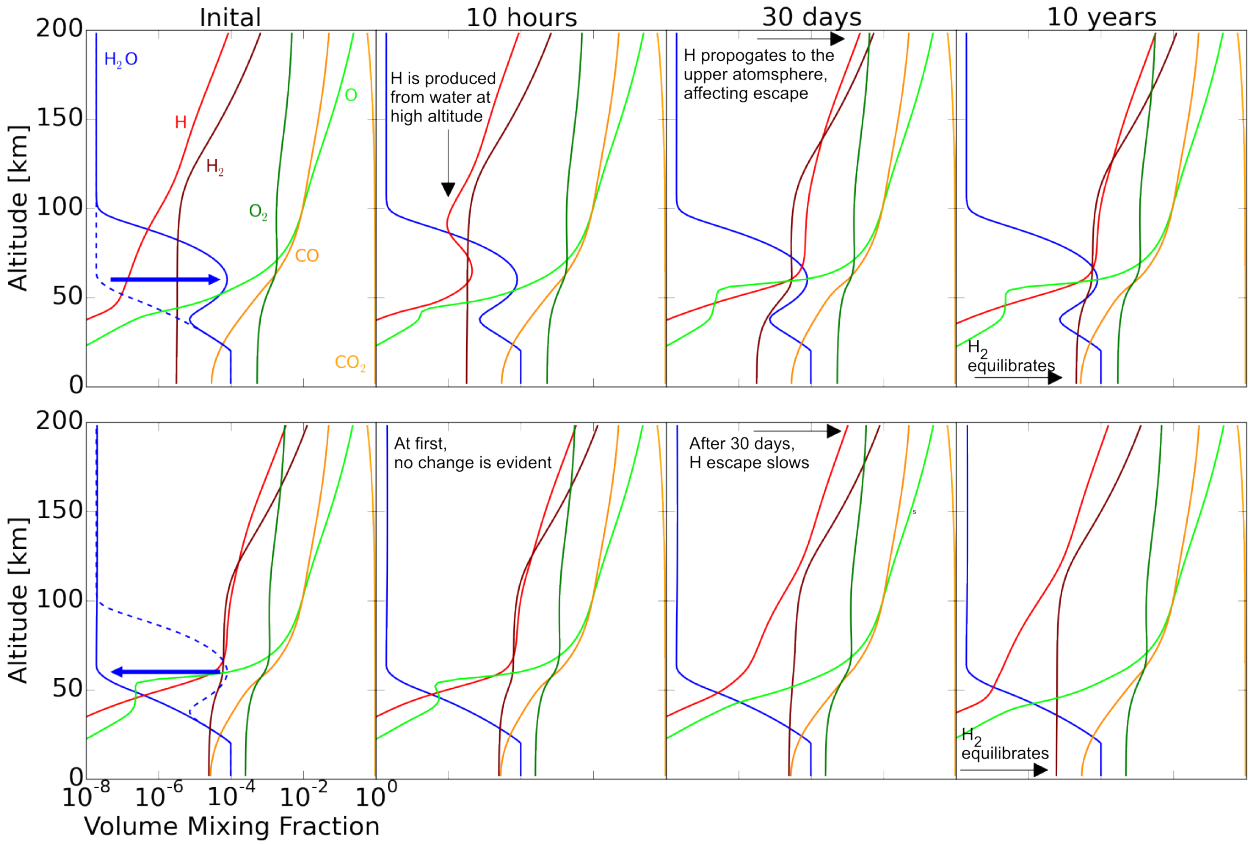

Figure 5.6: Time-response of atmosphere to water parcel introduction or removal. (top row) Response of the standard atmosphere to instantaneous introduction of a high-altitude water layer. (bottom) Response of the equilibrium high-altitude water model to the removal of the water layer.

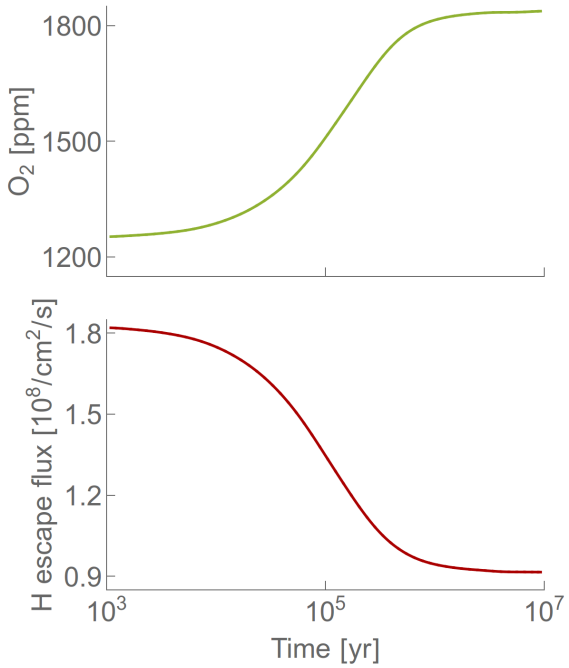

Figure 5.7: Effect of a factor 2 reduction in the O escape rate at $t = 0$. (top) Atmospheric O_2 concentration; (bottom) H escape flux, both shown over the ten million years following the change. This model assumes that molecular hydrogen is the source of the escaping H, an invalid assumption if high-altitude water layers exist.

first in a factor of ~ 10 decrease in H density at the upper boundary and H escape and the reintroduction of O at middle altitudes thanks to less efficient CO_2 recombination in the absence of water. Molecular hydrogen is a source of hysteresis in the system, as the large concentrations built up due to the enhanced water profile take ten years to escape from the atmosphere and return to normal.

These results demonstrate that introduction of water vapor into the atmosphere at a high altitude can greatly enhance H escape. This H escape enhancement occurs without a corresponding change in O escape on the same timescale. The factor of fifty change in escape is similar to that seen in SPICAM observations in 2007, indicating that this mechanism is capable of producing the escape changes observed.

5.3 Sensitivity to input water profile

Having established that the atmosphere can respond to the introduction of high altitude water on the timescale of observed H escape variations and with the same magnitude, we mapped out the response of the atmosphere to a wide range of introduced water profiles. Input water vapor profiles and the response curves of H escape over the subsequent year are shown in Figure 5.8.

Because we add water as a fraction of the total atmosphere, the absolute amount of water added is altitude-dependent. As a result, the proximity of the water added to the upper boundary and the total amount of water added are anticorrelated. This couples two of the input variables, but this coupling is not physically implausible: the mechanisms which act to add water at high altitudes in the Martian atmosphere are likely to produce a similar result.

For a given mixing ratio perturbation, increasing the altitude of the parcel reveals competing effects. At first, the higher altitudes permit easier photodissociation of the water vapor into odd H species, enhancing escape. As the altitude of the parcel gets larger than 80 km, the decreasing density of the bulk atmosphere (and hence the smaller size of the perturbation in absolute terms) overrides the increasing ease of photodissociation and transport to the escape region, and the H escape response of the atmosphere decreases. Regardless of the magnitude of the change in escape, water introduced at higher altitudes affects escape rates more quickly.

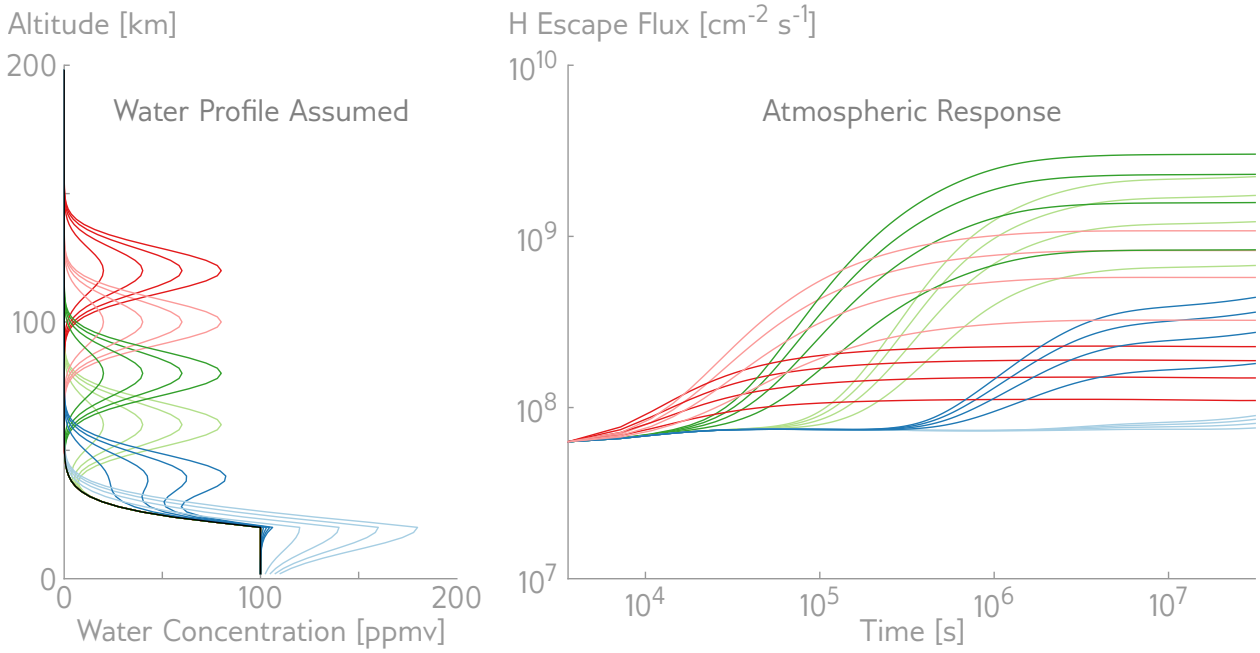

Figure 5.8: Sensitivity of atmospheric response to altitude and magnitude of water parcel injected. (left) Water vapor profiles instantaneously introduced into the standard water photochemistry, colored by altitude of injection. (right) Response of atmospheric escape to layer introduction. Within each altitude group, magnitude of response is intuitive: more water injection results in a larger impact on escape rates.

In our studies, H escape is mostly insensitive to large changes in lower-atmospheric water vapor on year-long timescales, in accordance with previous work. These low altitude changes represent the largest absolute changes in water concentration in our studies, with the majority of the enhancement below the kink in the eddy diffusion profile at 60km. Variations in the H escape as a result of these large changes in the water profile are less than a factor of two, minimally affecting escape from the atmosphere.

By contrast, water introduced in the vicinity of 80 km drastically affects H escape on a timescale of weeks, increasing hydrogen loss by over an order of magnitude. High-altitude water layers are thus a plausible source for the variations in atmospheric escape observed by SPICAM in Fall 2007. The absolute amount of water vapor added to the atmosphere by these changes is extremely small, on the order of one percent of the total integrated column. Small changes in the altitude profile of water vapor are therefore capable of greatly affecting atmospheric escape rates, making understanding the formation of these water layers in the Martian atmosphere a priority not only for Martian climatology but also for reconstructing the long-term history of water loss. The large enhancements observed by SPICAM in 2007 indicate that if these layers are present less for than 2% of the Martian year, they can still dominate H escape from Mars, overriding the constant source of H escape provided by molecular hydrogen, and potentially requiring significant revisions to the idea that diffusion-limited stoichiometric escape is occurring on Mars.

5.4 Additional observables

If water at altitudes of 40-100 km is driving the enhancements observed in H escape, as seems likely, the large perturbations in the H and O chemistry resulting from water vapor at these altitudes may be observable. OH increases from its background levels by an order of magnitude at the altitude of the introduced water layer, and O and O_3 are depleted by a similar amount. Despite these large changes, observations of these effects will likely prove challenging due to the low altitudes at which they occur. Of the available observation methods, stellar occultations will likely have too much extinction to perform useful retrievals. UV airglow observations will have to contend

with stray light from the bright limb and with high altitude dust, which may accompany the water. Solar occultations to be performed by ESA's Trace Gas Orbiter offer the most promise, due to the combination of high signal and high dispersion the orbiter's instruments will obtain. Submillimeter observations of the atmosphere are also sensitive to water at these altitudes, and could supplement measurement of water breakdown products with a direct measurement of the parent species.

Chapter 6

MAVEN IUVS

The Mars Atmosphere and Volatile EvolutioN mission (MAVEN) is dedicated to understanding the upper atmosphere of Mars [Jakosky et al., 2015]. MAVEN explores the interaction of the atmosphere with the space, determining how the atmosphere is being lost to space today and how the loss rate depends on solar activity. The loss rates and their dependencies will be used to extrapolate the loss of the Martian atmosphere backward in time, determining the extent to which the atmosphere and water have been stripped away from the planet over Martian history.

Particularly important for reconstructing the history of Martian volatile loss is an accurate measurement of the contemporary loss rate of neutral hydrogen from the atmosphere. Neutral hydrogen is most easily measured by MAVEN's Imaging Ultraviolet Spectrograph (IUVS), which observes H in scattered Lyman alpha sunlight, as does SPICAM on Mars Express. IUVS measurements of the H corona of Mars are the most extensive ever made, providing a high-quality dataset that allows detailed comparison against existing and future models of the corona.

The H corona of Mars revealed by IUVS has significant three dimensional structure and is poorly fit by a Chamberlain exosphere model. In contrast to the SPICAM data, which were broadly scattered in both space and time, the high-cadence measurements of IUVS provide a dataset that can be used to refine our understanding of the H corona beyond a spherically-symmetric model. In addition, unique high-altitude observations designed for MAVEN's insertion orbit have produced the highest-quality image of the H corona of Mars ever made, revealing a potential signature of non-thermal processes which may be populating the corona and dominating the escape rate.

A brief description of the IUVS instrument and its ongoing calibration issues is given below, followed by a description of IUVS H corona results gathered so far from three datasets: observations made during MAVEN's 35-hour insertion orbit, coronal scans similar to those made by SPICAM, and apoapsis disc maps. A discussion of necessary future efforts concludes the chapter.

6.1 IUVS capabilities and calibration

IUVS is an extremely capable instrument, designed to mitigate instrumental artifacts that affected previous Mars UV instruments [McClintock et al., 2014]. It minimizes crosstalk between far-ultraviolet (FUV, 110-190 nm) and mid-ultraviolet (MUV, 180-340 nm) channels by imaging FUV light in second order and MUV light in first order onto separate detectors. The instrument has two fields of regard that are separately baffled to minimize stray light (Figure 6.1). The instrument is mounted on an articulated payload platform (APP) and has a controllable scan mirror, allowing orientation of the instrument field of view independent of the spacecraft orientation. This enables high-cadence measurement of the H corona across all altitudes accessible to the spacecraft. In addition to its standard resolution mode, IUVS carries an echelle channel intended to observe D as well as H. When the interplanetary Lyman alpha line is sufficiently Doppler-shifted (more than $\sim$ 12.5 km s^{-1}) from the Mars line, this channel also independently measures the coronal and interplanetary line, enabling robust IPH background subtraction.

Figure 6.2 shows an example of IUVS data from the FUV channel.
This spectral image was gathered during MAVEN's first orbit around Mars, capturing the disk and limb of the planet and extending far into the corona. As in most spectra taken by IUVS, Lyman alpha is the most conspicuous and brightest feature in the FUV. The shape of the Lyman alpha line is well fit by a Voigt profile (Figure 6.3), allowing the brightness of Lyman alpha to be extracted from all IUVS spectra.

The absolute calibration of IUVS on diffuse sources remains unknown. During the cruise to Mars, dedicated stellar observations were used to calibrate the instrument against SOLSTICE stellar reference spectra [Snow et al., 2013]. Upon arrival at Mars, measured intensities of airglow emissions

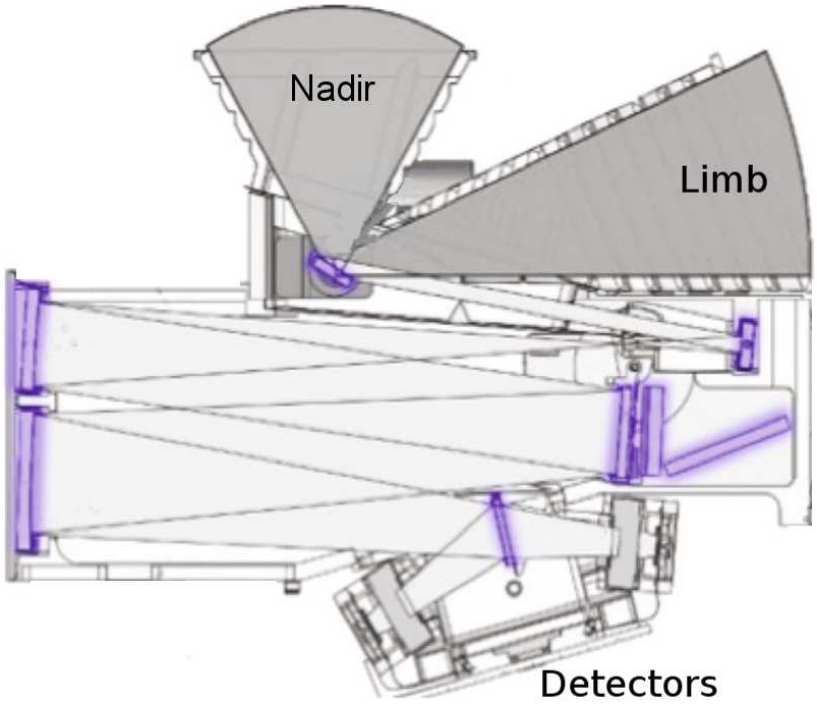

Figure 6.1: Diagram of the IUVS instrument. Light enters through separately baffled nadir and limb fields of regard at the top of the image, and is directed by a scan mirror toward the telescope, slit, and spectrometer. FUV and MUV light is separated by a beamsplitter and imaged onto distinct detectors at the bottom of the image.

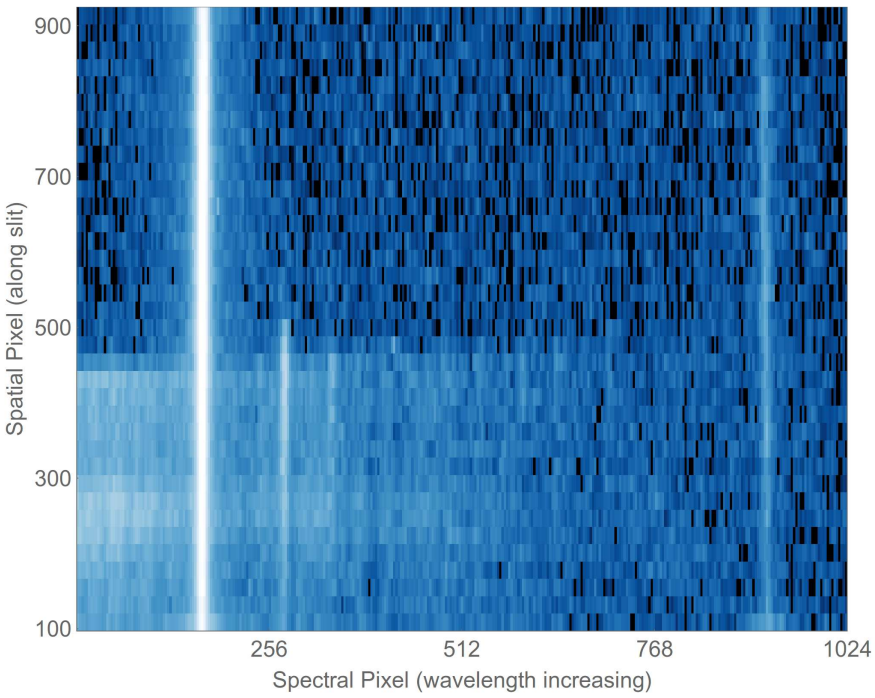

Figure 6.2: IUVS detector image. Wavelength runs horizontally, with short wavelegths at the left. Lyman alpha is conspicuous as the bright feature near pixel 200, followed by oxygen emission at 130.4 nm and 135.6 nm near pixel 256. Position along the instrument slit runs vertically, with the disk of Mars filling the lower half of the field of view with first-order MUV light unintentionally imaged onto the 2nd-order FUV detector. Only a portion of the full detector is shown. Oxygen and hydrogen emissions extend far above the limb of Mars, which appears as the dropoff in broadband intensities below spatial pixel 500. At far right, Lyman alpha appears in third order. Color scale is arbitrary and logarithmic.

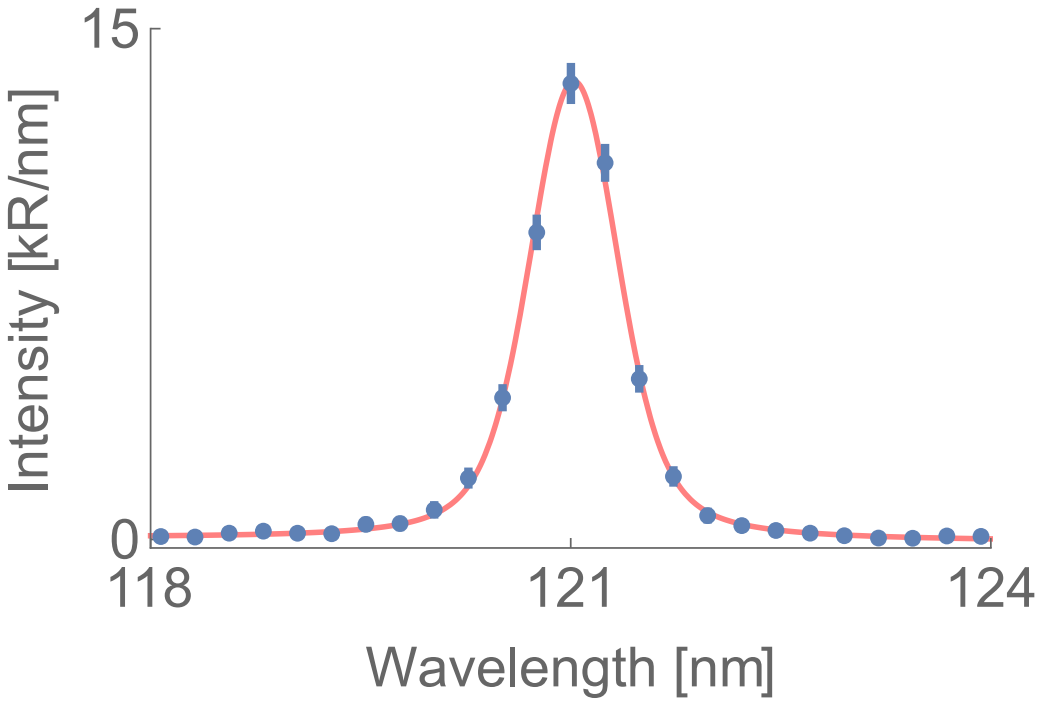

Figure 6.3: Example fit to IUVS data. Blue points represent instrument data and derived one sigma uncertainties. Red curve shows Voigt function fit to these data.

in both the FUV and MUV were brighter than all previous observations of the Mars airglow, including those made by SPICAM, Rosetta, and Mariner. Even accounting for the differences in observation geometry and solar activity, the IUVS observations are brighter than expected by a factor less than two, likely close to 1.6. The cause of the discrepancy remains unknown; candidates include undiagnosed nonlinearity in the detector, vignetting of starlight relative to airglow, or an incorrect geometrical factor used to transform from the point calibration on the stars to the continuum measurement of the airglow. None of these seems likely, and the problem remains unsolved.

Even if the calibration at longer wavelengths is known, it is difficult to calibrate at Lyman alpha. Interplanetary and interstellar hydrogen produce strong extinction at this wavelength in the interstellar medium, so that even bright stars have their spectrum completely extincted in the core of the line. With no standard candles, instrument calibration at Lyman alpha is usually determined by interpolation across the line rather than directly measured. This can sometimes result in miscalibration, as was the case for Cassini UVIS: the detector was overexposed to interplanetary hydrogen, which resulted in a loss of sensitivity at Lyman alpha but not at adjacent wavelengths [UVIS Team, 2014]. Given the modest exposure of the IUVS detector to the IPH and the care taken to avoid detector saturation, we do not expect degradation at Lyman alpha to affect IUVS intensities. Nevertheless, significant difficulty has been encountered when attempting to converge on a uniform calibration at Lyman alpha across instruments; SOHO/SWAN and MESSENGER/MASCS were unable to agree on the absolute brightness of the IPH to better than 40%, owing to difficulties in the calibration of one or both instruments [Quémerais et al., 2013].

To determine absolute escape rates of H from measurements of coronal brightness, an accurate instrument calibration is extremely important. Because H Lyman alpha is optically thick, small variations in observed brightness translate to large variations in column density along the line of sight and in turn to large variations in the derived escape flux of hydrogen. For example, in the coupled Chamberlain and radiative transfer model employed in this work, a 10% variation in the brightness of emission implies a factor of two variation in the escape flux from the planet. This

nonlinearity is an inescapable consequence of the optical depth of the corona, and affects all H escape flux measurements made with scattered Lyman alpha.

IUVS observations of the corona in Lyman alpha are too bright to be plausible, unless the hydrogen temperature is so large that it is hydrodynamically escaping ($T > 1500$ K). With the uncorrected intensities, no density or temperature in the precomputed model parameter space $n_{\rm exo} = 1 \times 10^4 - 7 \times 10^5$ cm^{-3}, $T_{\rm exo} = 100 - 1600$ K is bright enough to match the observations. In addition, near-simultaneous observations of the corona by IUVS and the Hubble Space Telescope reveal nearly identical intensities despite IUVS observing a region of the corona predicted to be perhaps 2 times dimmer (Figure 6.4). In these observations, which occurred in October 2014 near the close encounter between Comet Siding Spring and Mars, IUVS observations from a platform embedded in the corona and observing toward the nightside have intensities similar to those obtained from Hubble observations through the entire corona across the dayside of the planet.

The large and likely miscalibrated IUVS brightnesses prevent comparison with the model, unless a scaling factor is applied to the data. For the work of this thesis, a scaling factor of 1.6 has been used to correct the model upward for comparison with IUVS brightnesses. When IUVS intensities are displayed, they are displayed as the instrument reports them, including the anomalously high calibration. All modeled values displayed are scaled up to match the likely anomalous calibration of the instrument. Because obtaining an absolute calibration at Lyman alpha is challenging with any spectrograph, a correction factor of a similar nature and a value of approximately 1.1 was employed in analyzing data from SPICAM in order to obtain a better fit between the model and the data. This indicates that as with IUVS, SPICAM was likely underestimating the instrument sensitivity at Lyman alpha.

IUVS observations of the H corona benefit from simultaneous observations of the solar brightness at Lyman alpha made by MAVEN's Extreme Ultraviolet Monitor (EUVM). Instead of extrapolating the solar flux measured at Earth to Mars, a dedicated photodiode measures the broadband solar flux at Lyman alpha on a one second cadence, allowing the line center flux at Mars to be computed and used in the radiative transfer. These MAVEN/EUVM observations will enable mea-

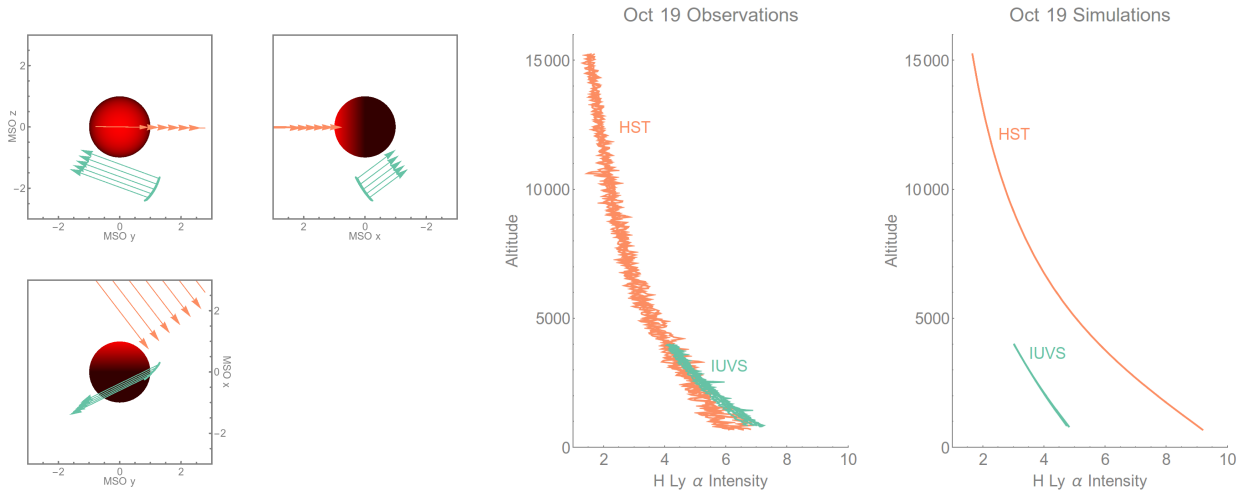

Figure 6.4: Comparison of HST and IUVS observations of the corona on October 19, 2014. At left, observation geometry in MSO coordinates, with IUVS sightlines (green) originating at the arc representing the spacecraft orbit and HST sightlines (orange) originating at infinity. Middle panel shows calibrated HST and uncorrected IUVS intensities (in kR) for these lines of sight. At right, model predictions of the intensity from the coupled physical and radiative transfer model, demonstrating that the HST profiles are predicted to be roughly twice the brightness of the IUVS observations.

surements at Mars and extrapolations from Earth to be compared for the first time, revealing (and hopefully verifying) the accuracy of all previous attempts to estimate the solar flux at Mars from Earth data. For plotting and comparison purposes only, changes in solar brightness have been removed from all plots shown by scaling coronal observations to the same incident solar flux, chose arbitrarily from observations in October near the beginning of the mission and avoiding flares, which can perturb the solar spectral irradiance at Lyman alpha by less than 10%. The solar flux at Lyman alpha can vary by nearly 10% of percent across a solar rotation; this change represents the physics of the Sun and not the Mars corona. When not displayed graphically, all model comparisons are done with measured and uncorrected coronal brightnesses and solar flux.

6.2 35-hour insertion orbit observations

MAVEN's 35-hour insertion orbit had an apoapsis near 14 Mars radii (r_M), potentially allowing unprecedented observations of the distant corona. To maximize power and communication, during the insertion orbit the spacecraft antenna was continuously pointed at Earth, with the solar panel axis in the plane of the solar system (see Figure 6.5). These constraints allowed a single remaining choice about the spacecraft orientation: whether to point the IUVS field of view toward celestial north or south.

Analysis of the predicted geometry of the insertion orbit led to the conclusion that orienting upward would allow Mars to transit the instrument field of view near the spacecraft apoapsis (Figure 6.6). A 35 minute long repetitive mapping sequence was designed to capture spectral information from both fields of regard, mapping the disc of the planet and the corona to distances of more than $10\,r_M$.

MAVEN stayed in its insertion orbit for three cycles before beginning maneuvers to reach its mapping orbit. During this time, the intensity of Lyman alpha was measured from the spacecraft along over 580,000 lines of sight through the corona.

To combine data gathered in all three orbits into a single image and avoid contamination from observations gathered near Mars while deeply embedded in the corona, instrument data gathered

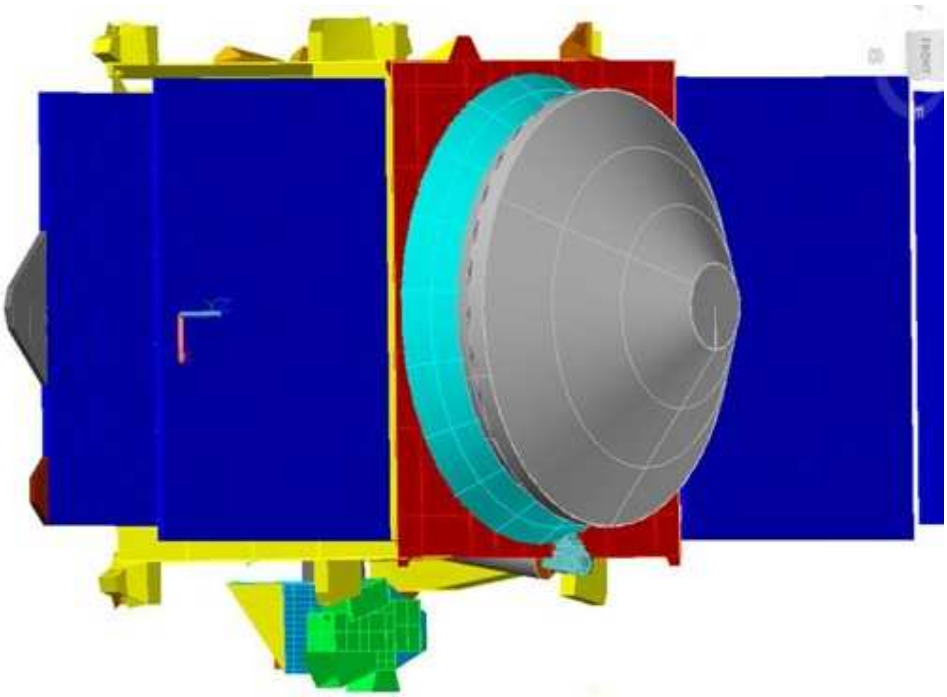

Figure 6.5: MAVEN spacecraft in cruise configuration, with booms stowed. During the insertion orbit, the high-gain antenna (gray) way pointed at Earth with the solar panels (blue) in the plane of the solar system. This left one choice for IUVS (green): whether to be oriented toward or away from celestial North.

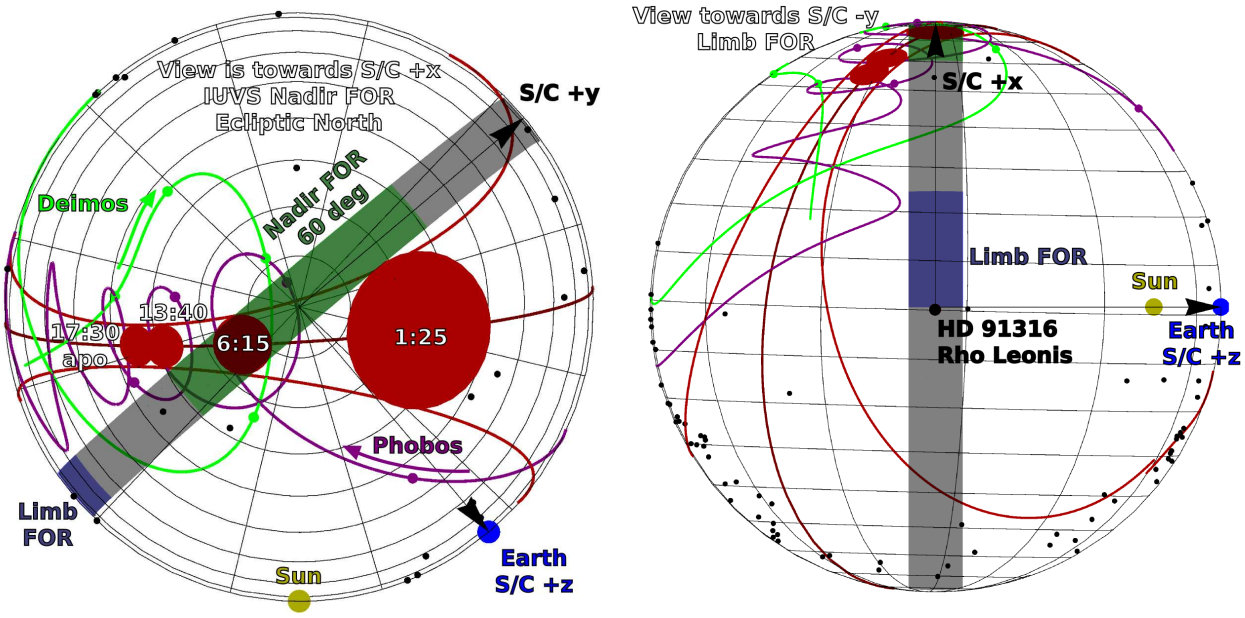

Figure 6.6: Planning diagrams for IUVS observations during MAVEN's 35-hour insertion orbit around Mars. Spacecraft (S/C) +z axis/ high gain antenna is oriented toward Earth, with the solar panels in the plane of the solar system. Mars begins to transit the IUVS Nadir field of regard 1h25m after Mars orbit insertion, and exits at 13h40m. Deimos and Phobos also transit the field of view, with dots on their orbital tracks at the same times as Mars is shown. The IUVS limb field of view looks into interplanetary space, capturing the UV-bright star Rho Leonis.

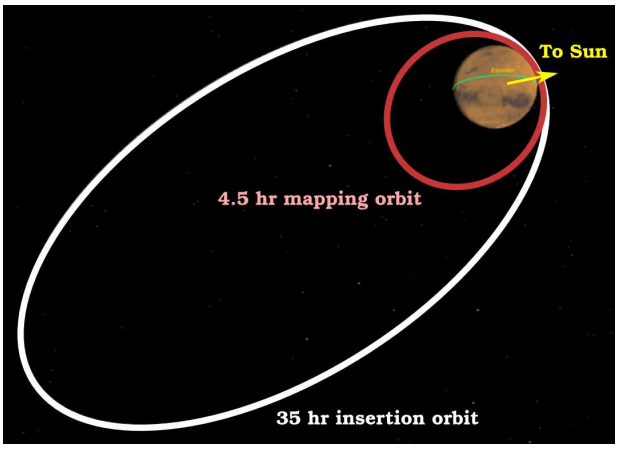

Figure 6.7: Geometry of 35-hour insertion orbit, to scale with Mars. At apoapsis in the 35 hour orbit (white), MAVEN is above the 3AM meridian near $-60°$ latitude, at a distance of $13r_M$.

at a radial distance of more than $10\,r_M$ were selected. Each line of sight was binned in a two-dimensional angular coordinate system centered on Mars, with one angular axis toward the Sun. Angular bin sizes were set at $r_M/20$, using the angular size of Mars appropriate to each spacecraft location. Binned intensity values were then averaged. The result of this process is shown in Figure 6.8, which represents an angular map of the sky as seen by MAVEN during its insertion orbit. At apoapsis during the insertion orbit, Mars subtended just over 10° on the sky, and the spacecraft was below the ecliptic on the night side of the planet, looking up toward the dawn terminator (Figure 6.7).

In the image, the upper portion of the corona was viewed out of the IUVS nadir port, and the lower portion through the limb port. The center of the nadir port captured the disk of Mars just before apoapsis, with Mars in the field of view for approximately 12 hours out of every 35. The best sampled region of the image is at the outer edge of the upper field, observed out of the nadir port at apoapsis. Coarser on board data binning in the nadir port results in a more sparesly sampled corona at those locations, introducing small data gaps.

The high altitudes achieved by MAVEN during its insertion orbit will not be obtained by MAVEN again. These observations therefore represent a unique opportunity to probe the high-altitude corona of Mars without the geocoronal foreground that complicates observations from Earth-orbiting telescopes.

At the highest altitudes in the Mars corona, far less scattering occurs, easing interpretation of the data. In the IUVS map, intensities peak near the sunward portion of the limb at slightly less than 13 kR, fading to near 1 kR at the edges of the image. Typically, Lyman alpha is optically thick for intensities greater than about 1 kR, depending on the brightness of the Sun, so that the Mars corona observed by IUVS is almost everywhere optically thick. If IUVS is miscalibrated by a factor of about 1.6, as we suppose, then the outer edges of the corona from MAVEN's apoapsis are optically thin.

To understand whether the corona in these images is well-fit by a Chamberlain exosphere, the coupled physical and radiative transfer model was fit against all 580,000 lines of sight gathered

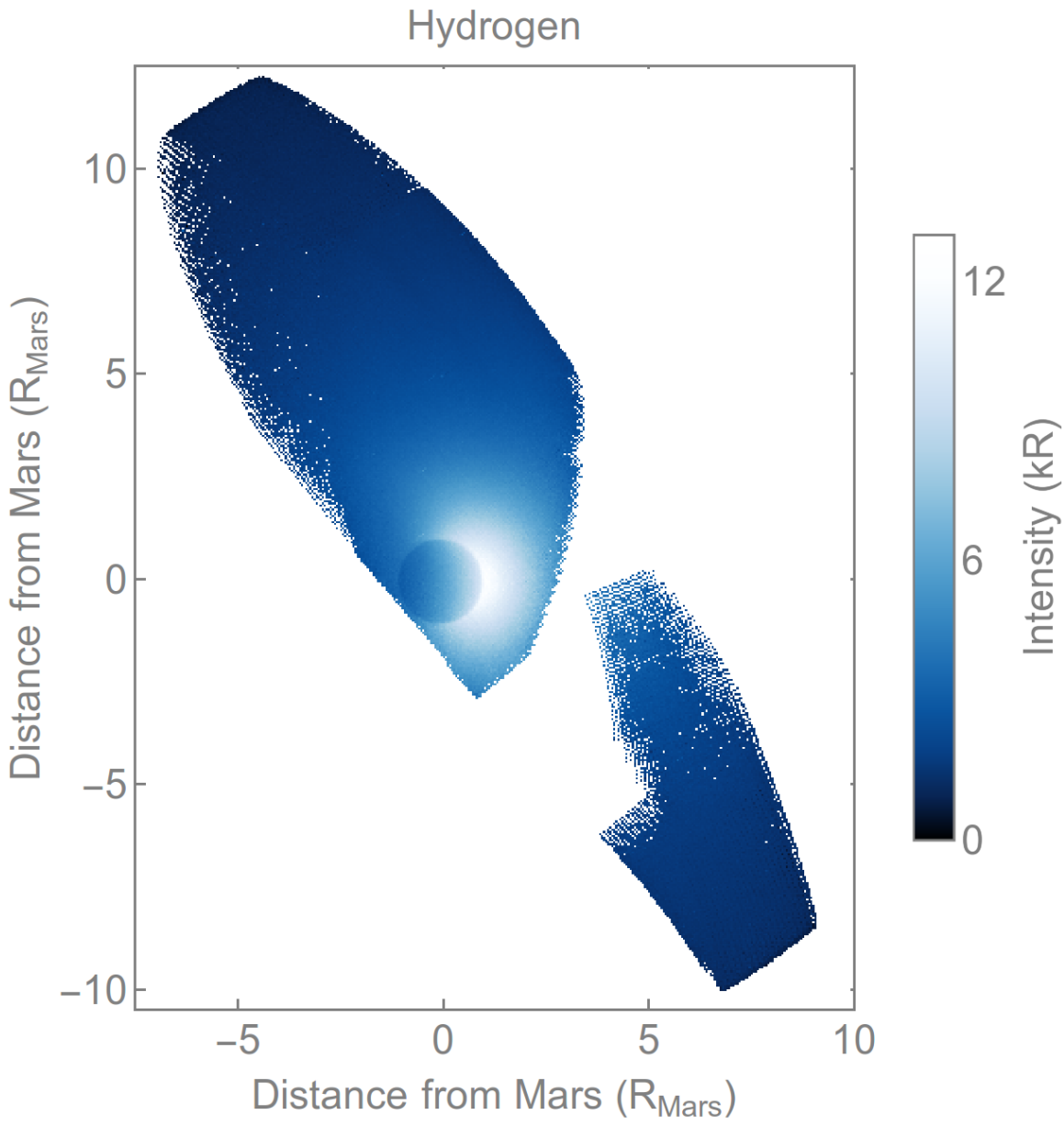

Figure 6.8: IUVS map of the Mars H corona made during its insertion orbit. This figure represents an angular map on the sky, in terms of the angular radius of Mars. Intensities pending final calibration, as discussed in text.

in all three orbits simultaneously. The best fit was obtained by chi-squared minimization of the model with respect to the intensity observed along every line of sight, incorporating estimated uncertainties in the data. Because the observations cover such a wide region on the sky, the slowly-varying structure of the IPH is imprinted below that of the corona. This is modeled with the fully integrated interplanetary hydrogen background model, computing the IPH intensity observed along the spacecraft line of sight and the extinction imposed by the corona, incorporating the Doppler shift of Mars and the spacecraft relative to the line of sight IPH velocity. After fitting, the resulting best fit model is a simulated dataset with the same size and geometrical sampling as the observations. In order to compare the model and the data and guard against potential artifacts, the best fit was processed identically to the original data, resulting in an image of the model corona.

The best fit model and its deviation from the data are shown in Figure 6.9. Notably, the structure of the model corona is significantly different from that of the data, being more confined in radius. The brightness structure typical of a Chamberlain exosphere is not shared by the data, which appears more concentrated or collimated in the sunward direction than the model. Increasing the temperature does not change this characteristic shape (Figure 6.10). The best fit density and temperature for this model are $n = 2 \times 10^5$ cm^{-3} and $T = 200$ K respectively, far colder than historical fits to hydrogen density and temperature resulting from coronal scans on previous missions, save Rosetta. The temperature is far closer to that expected for the neutral CO_2 atmosphere than earlier fits. The Jeans escape rate for this set of exobase conditions is 4×10^7 cm^{-2} s^{-1}, in family with the majority of the SPICAM results but lower than Mariner and the SPICAM observations gathered in southern summer.

The escape flux computed by the model is only accurate if the model fit is good. However, the relative deviation of the model and the data reveals several difficulties with the fit. First, the modeled disk intensities are too low, likely due to inaccuracies in the model thermosphere diffusion or transport of hydrogen, which should be adjusted to match the observations. Second, the model corona is too bright near the planet and too dim far away, indicating that the model is balancing deviations from the data near the planet against those that are gathered farther away. This indicates

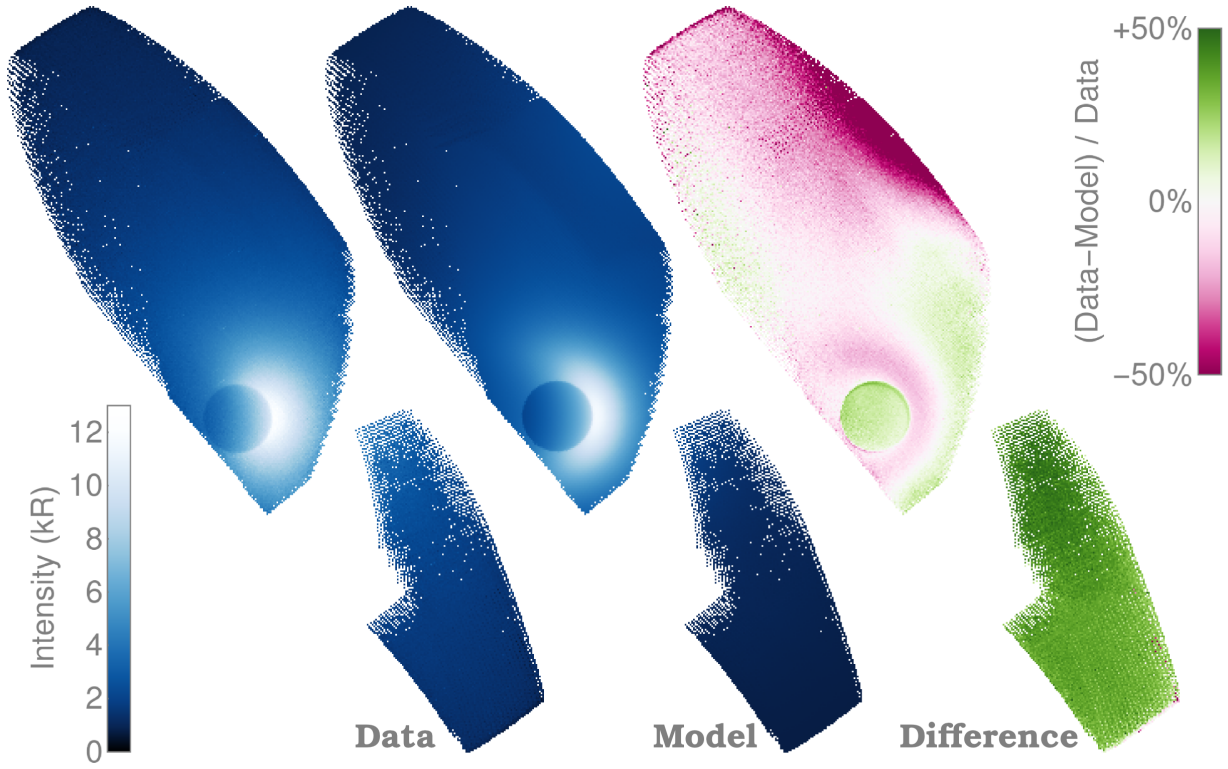

Figure 6.9: Comparison of observed and model corona. Intensities pending final calibration.

Figure 6.10: Reproduction of Figure 3.6, showing simulated coronal brightness for Chamberlain exospheres at different temperatures. As the temperature increases, the corona grows brighter and more extended but the shape is unchanged.

that the data would be better fit with two populations: one that dominates near the planet and another that dominates farther away. This requirement for two populations is a clear argument for either spatial temperature asymmetries in the corona (for example, between the day and night side) or the existence of a global hot hydrogen population at Mars. Both explanations are incompatible with the current Chamberlain exosphere physical density model: more detailed modeling is required to capture the physics of the corona, and is described at the end of the chapter. Finally, the excess of the model relative to the data at the top of the image indicates that the IPH model is not accurately reflecting the background intensities, and must also be investigated. It is worth noting that the large relative deviations shown in the map represent small absolute variations at the large distances from the planet where the IPH contribution is significant: inaccuracies in the IPH model are less important close to the planet, where MAVEN gathers its mapping data.

6.3 Coronal scans

In coronal scan mode, IUVS observes the corona across the spacecraft orbit on the outbound and inbound leg of the orbit (Figure 6.11). The observations are made in the same inertial direction, so that the instrument observes the same interplanetary hydrogen intensity through the corona. Because the corona is optically thick, these observations cannot be usefully subtracted, but they can be modeled simultaneously.

Coronal scans from the first four months of MAVEN operations are shown in Figure 6.12. IUVS gathers H coronal scans every fourth spacecraft orbit, when the instrument has control of the APP orientation and the instrument is in low-resolution mode. The MAVEN orbit was designed to precess around Mars so that in situ instruments can sample a wide range of solar latitudes and longitudes at periapsis. For this reason, coronal scans made along the sides of the orbit also sweep through different locations in the corona with time. At the beginning of the MAVEN mission in late 2014, IUVS coronal scans looked toward the night side of the planet across the evening terminator in the Southern hemisphere. Over the next six months, these scans swept around Mars as seen from below, passing south of the subsolar point. By the beginning of March 2015, the coronal scans were

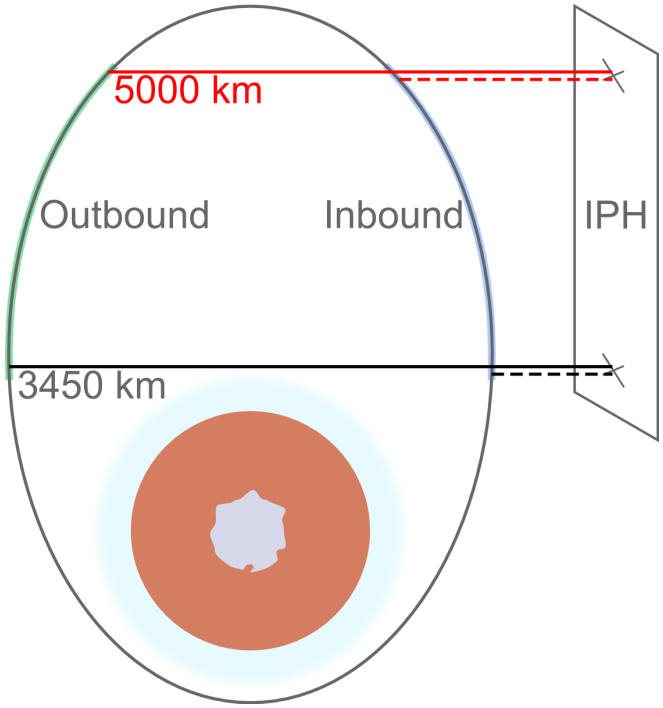

Figure 6.11: Geometry of MAVEN coronal scans. Observations are made across the corona on the outbound leg of the spacecraft orbit and out of the corona on the inbound leg. Both have the same inertial look direction and the same IPH brightness.

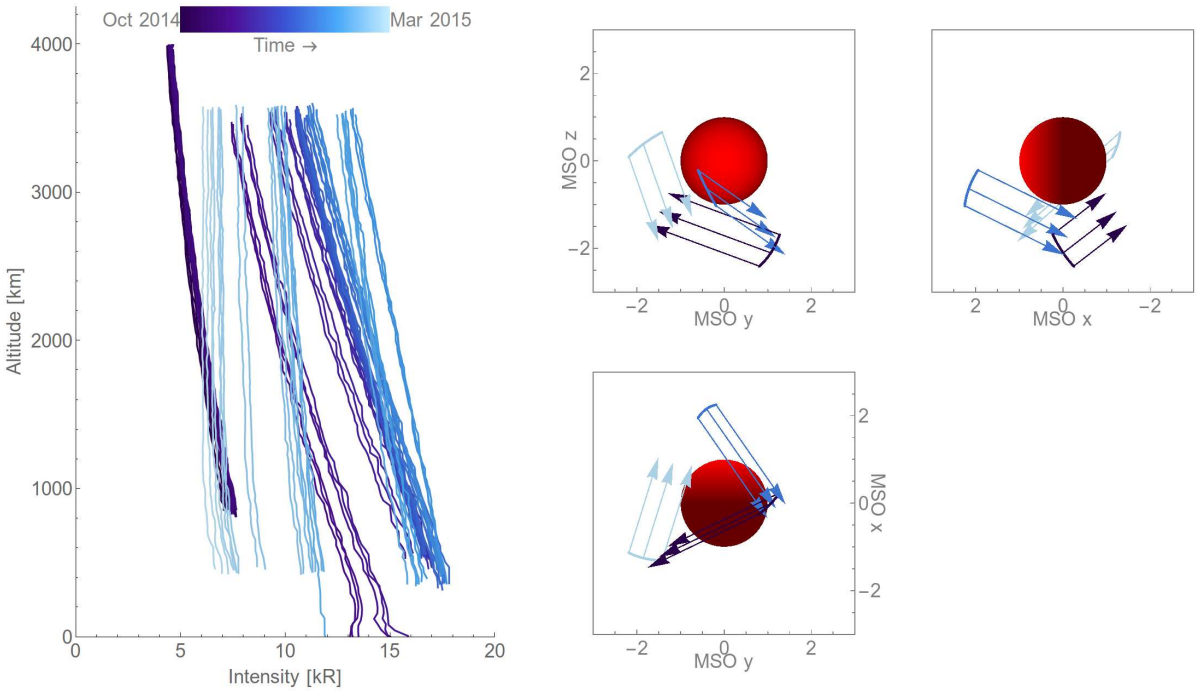

Figure 6.12: MAVEN coronal scans, Oct 19, 2014-March 1, 2015. (left) IUVS reported intensity of Lyman alpha as a function of tangent altitude, pending final calibration. Color indicates relative time of observation, as indicate at top left. (right) Spacecraft orbit and observation direction for three coronal scans, colored to match the time of the observation. Arc represents spacecraft location and arrows observation look direction.

oriented toward the Southern dayside across the dawn terminator.

The brightness observed in the coronal scans is commensurate with the portions of the corona observed, increasing in brightness as the instrument line of sight moves into the dayside corona, with the brightest observations occurring near the subsolar point in the middle of the observation set. After the peak brightness, observed intensities get dimmer but the profiles get increasingly shallow, with nearly vertical intensity profiles at the end of the observation period when the instrument is looking across the dawn terminator.

To aid interpretation of these profiles, two model case studies were computed. First, the coupled physical and radiative transfer model was fit to the earliest coronal profiles, taken in October. The best fit parameters for these profiles are $n = 7.7 \times 10^4$ cm^{-3} and $T = 320$ K, similar in temperature but twice the density of Mariner observations, implying an escape rate roughly twice that observed by Mariner. These parameters were used to compute theoretical intensities for the observation geometry of all other coronal scans. This simulation set tests the null hypothesis that there is no spatial or temporal variability in the state of the corona. Second, the model was used to determine the best fit parameters for each observation independently. This case study can identify temporal but not spatial variation, as the underlying physical density model is spherically symmetric. This second test determines whether the coronal profiles can be fit with a time-varying exosphere only, or if spatial variation is also required.

The results of the model case studies are shown in Figure 6.13. The steady state model does an adequate job of fitting the earliest observations by design, but for later observations the fit is increasingly poor, with the worst fit near the subsolar point on the dayside. The slopes of the model on the dayside are uniformly shallower than the data, a problem that is only exacerbated for the latest observations, where the model profile shapes are qualitatively incorrect[1]. This indicates that there is substantial temporal or spatial variability in the corona not reflected by a steady-

[1]These shapes, which increase in intensity at middle altitudes, are not wrong. While density decreases monotonically with altitude, the optically thick nature of the corona and the fact that the spacecraft is embedded deep in the corona means that the intensities can increase with tangent altitude as the spacecraft views more illuminated regions.

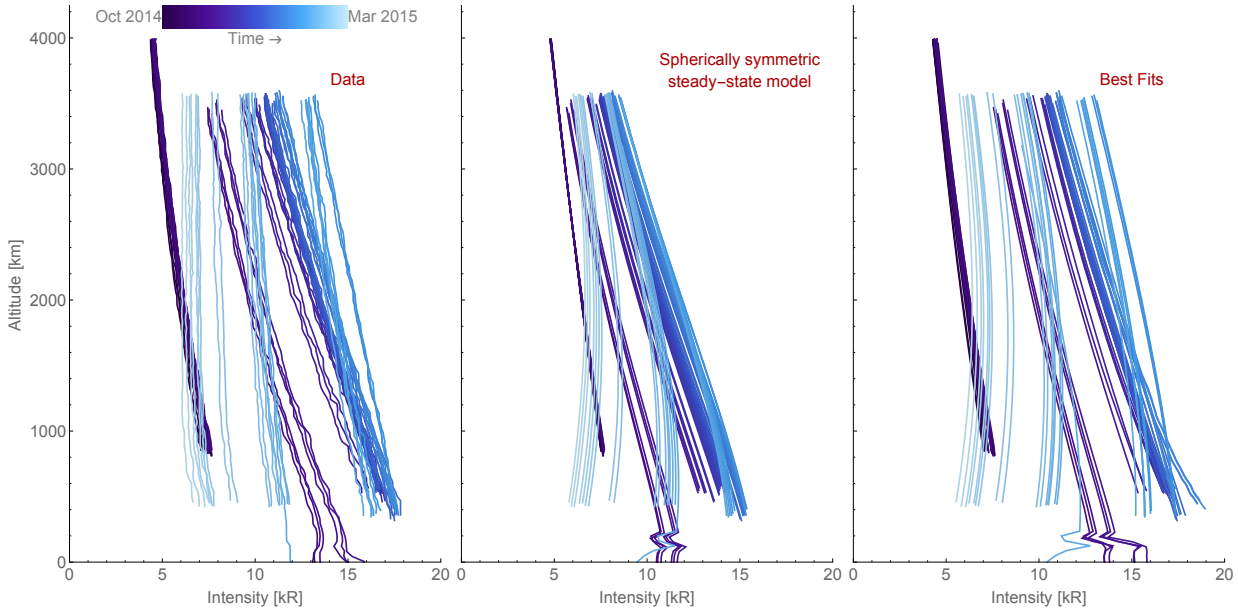

Figure 6.13: Comparison of coronal scan data and model case studies. At right, IUVS data (pending final calibration) as shown in Figure 6.12 above. Center, theoretical intensities resulting from a fit of a steady-state model to the earliest observations. Right, best fit model intensities for each observation.

state model. One possibility is the seasonal variation uncovered by HST and SPICAM, discussed in Chapters 2 and 4, which affects the extent of the corona on seasonal timescales. A second possibility is the dayside contribution of hot hydrogen to the exospheric profiles, which would act to inflate the scale height on the dayside only, with a maximum effect near perihelion when solar forcing is strongest. As with the 35-hour orbit model comparison, below 200 km the model values do not reflect the data, indicating that some aspects of thermospheric physics have been neglected.

Allowing the model to perform a best fit to each observation improves the match to the data, greatly increasing the scale heights on the dayside near the midpoint of the observations. The model still does a poor job of fitting the shape of the profiles for the latter half of the observations, predicting convex profiles while the data are extremely shallow and concave. This indicates that temporal variability alone is not enough to explain the observations: the underlying model is incorrect, and escape rates computed from the model do not reflect reality. The model deficiency is likely due to the assumption of spherical symmetry of the hydrogen density distribution. The shallow slopes observed looking across the dawn terminator indicate either that there is much higher escape occurring at dawn, or that this region is a location of significant transport from the remainder of the atmosphere. Either would act to increase the density and therefore brightness of the corona at high altitudes relative to low altitudes.

Simulations of the 3D distribution of hydrogen in the upper atmosphere provide context for this result. Using a general circulation model of the thermosphere and ionosphere, Chaufray [Chaufray et al., 2015] simulated the density and temperature distributions of hydrogen at the exobase at several times over the Martian year. In part, this study compared density profiles of coronal hydrogen resulting from the from the 3D model with Chamberlain models using local conditions (Figure 6.14).

The one dimensional calculations using the local hydrogen density and temperature track the three dimensional hydrogen distribution below 1000 km, but depart significantly at higher altitude. In the highest regions of the corona the three dimensional simulations are isotropic: at these altitudes the hydrogen in the corona is sourced from the entire thermosphere, and tracks the mean

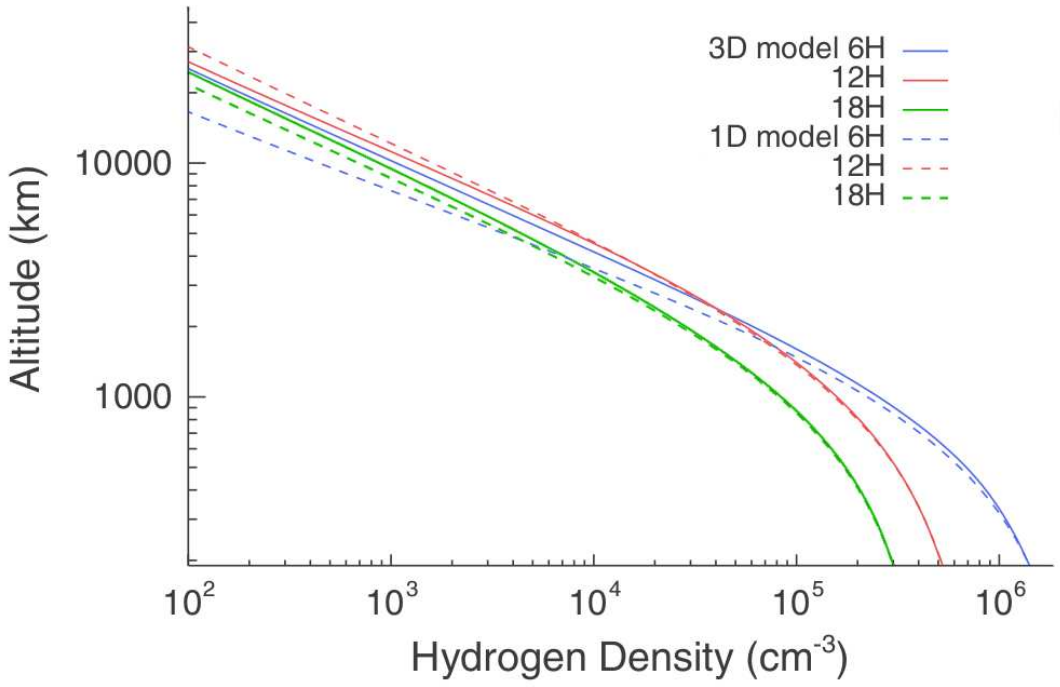

Figure 6.14: Predictions of the three-dimensional structure of the Mars H corona at equinox, from Chaufray et al. (2015). Dashed lines show one dimensional Chamberlain exosphere density profiles for the local density and temperature at three local times. Solid lines represent the density in the 3D model.

thermospheric density and temperature. At lower altitudes, the temperature of each region has more of an effect, resulting in a density enhancement at dawn.

In Chaufray's simulations, the location of the density enhancement varies with season, based on the prevailing thermospheric winds (Figure 6.15). At equinox, a large enhancement at dawn is produced, but near solstice the bulge is concentrated on the night side. The IUVS coronal scans observed the dawn limb in February of 2015, just after the Southern summer solstice. At this season, the thermosphere model predicts that no H bulge should be present at the terminator. The extended near vertical shapes observed by IUVS and the relative brightness of the data at the lowest altitudes compared to the model suggest that a bulge may be present, in contradiction of the model prediction. With a one-dimensional profile, it is difficult to be sure; luckily IUVS observes the whole disk of the planet every apoapsis.

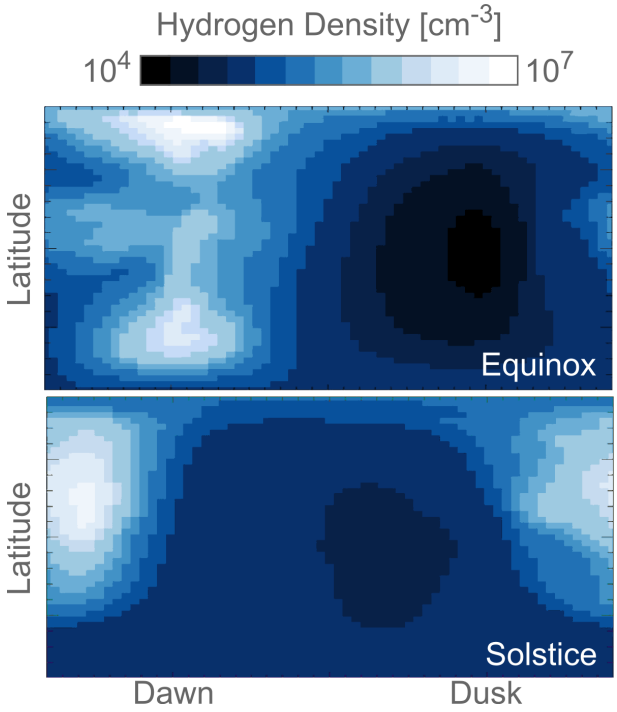

Figure 6.15: Models of hydrogen exobase density distribution, adapted from Chaufray et al. (2015). Each panel shows density of hydrogen in geographic latitude and solar longitude for two seasons: Southern spring equinox (top) and Southern summer (bottom).

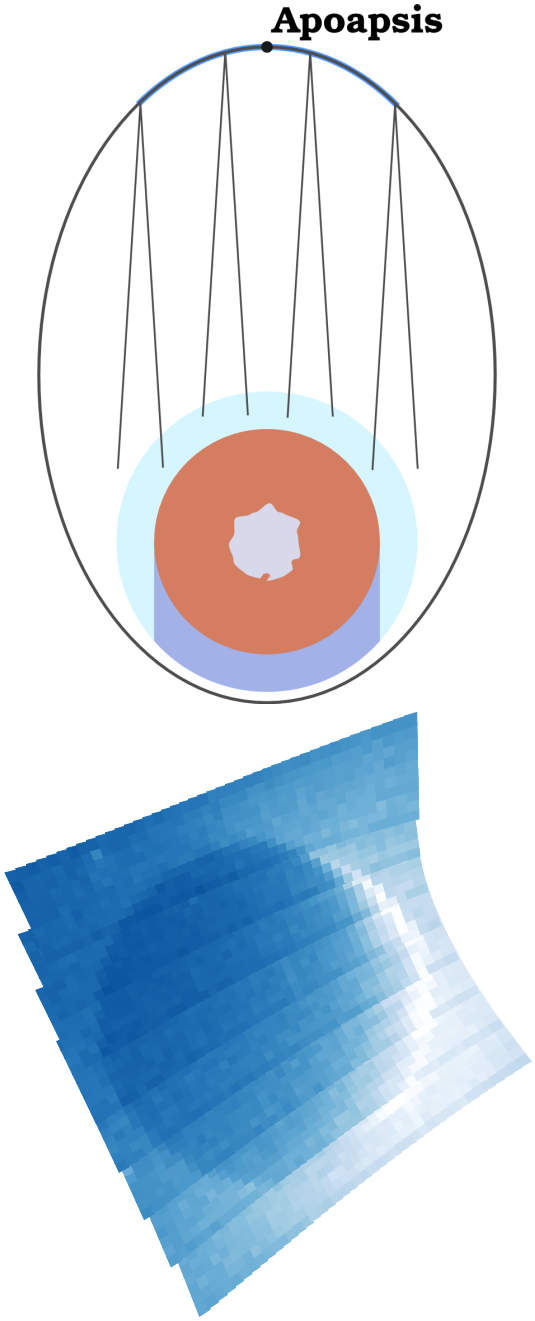

Figure 6.16: Geometry of MAVEN apoapsis disk maps and sample apoapsis data. Swaths have been rotated and overlaid, assembling an image of the planet with the Sun to the right.

6.4 Apoapsis maps

Apoapsis disc maps complete the means IUVS has of constraining the H corona. At the top of its orbit, IUVS is oriented downward toward the planet and the instrument field of view is scanned across the disc in two dimensions. One dimension is mapped by the instrument scan mirror, and the second covered with spacecraft drift. In total, eight passes across the planet are made, referred to as swaths. The data gathered near apoapsis can be transformed into a Mars-centric frame and overlapped; a circular planet image results (Figure 6.16).

IUVS gathers apoapsis images in each orbit around MAVEN, at four times the cadence of the coronal scans for hydrogen. These scans are limited in their ability to assess the full H corona, because Mars subtends more than 40° even when the spacecraft is farthest from the planet, and because the instrument is still deeply embedded in the corona at its $3r_M$ apoapsis. Nevertheless, disk and near-limb science can be performed with these images, whose greatest tangent distance from Mars approaches 1000 km.

Figure 6.17 shows an apoapsis observation set from near the beginning of the mission. In these images and in all subsequent apoapsis sets all of the data are viewed at once, with all swaths side-by-side. This results in some regions of the corona appearing multiple times.
As always with the H corona, the specifics of the observation geometry are important and comparison with a model is essential for interpretation of the optically thick emission. For this observation, apoapsis was below the planet on the night side, looking up at the Southern hemisphere. The model is the best-fit possible within the precomputed parameter space. Stripes in the data and residuals between swaths are due to variation in the instrument sensitivity along the slit, and do not indicate true variation in the corona.

Similar diagrams for a subset of apoapsis datasets spanning the mission so far are shown in Figure 6.18, showing the evolution of the MAVEN orbit and the data gathered. Over the first four months of the mission, MAVEN's apoapsis circled the planet's south pole. The dayside of the planet was imaged in January of 2015 near southern hemisphere summer solstice; these maps exhibit the

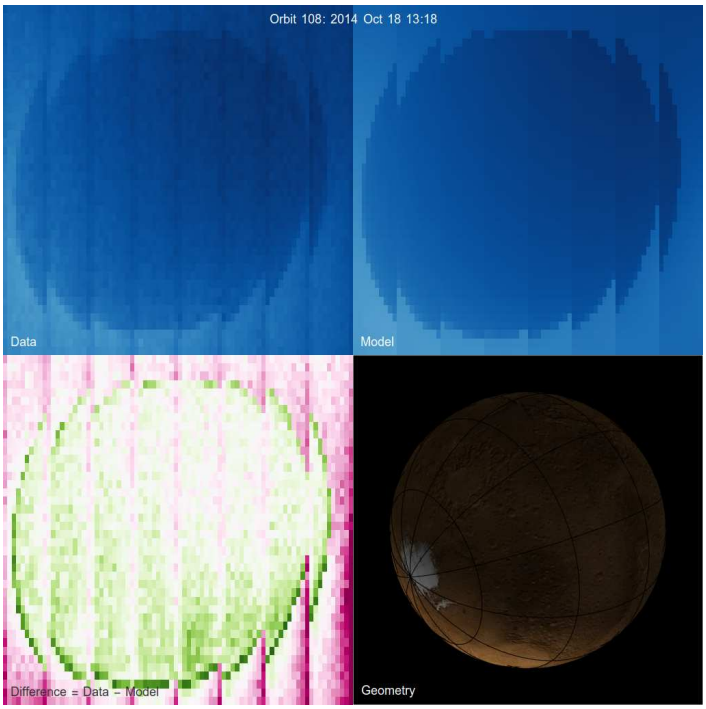

Figure 6.17: Example MAVEN apoapsis image set. Orbit number and UTC time given at top of image. (top left) IUVS data gathered during apoapsis. In these images, white represents 15 kR (pending final calibration); the scale is linear, with black representing 0. (top right) Best-fit model, scaled identically with data. (bottom left) Relative deviation of model and data, on the same scale as Figure 6.9, with red indicating that the best-fit model overpredicts the data by 50% and green indicating underprediction. (bottom right) Observation geometry, for this map set looking up at the Southern hemisphere dawn terminator.

largest brightness in the dataset. Coronal scans exhibiting extended, near vertical profiles were gathered in mid-February; images from these dates appear one row above the bottom, where the terminator bisects the planet.

In the earliest images gathered, at the top of the page, the model is striking a balance between disk and coronal intensities. This indicates that the population supplying the corona is not the same as that imaged on the disk: a likely consequence of supply by the hotter dayside contributing more to coronal densities at high altitude.

When the dawn terminator is on the limb as seen from apoapsis (row 3), the model underpredicts near limb intensities. The data shows a diffuse prominence that the model does not share, supporting the idea that transport or local production of hydrogen is affecting densities at the dawn terminator. The feature is persistent for weeks, and is visible as long as the dawn terminator is aligned with the limb. This suggests that the bulge results from long-lived processes operating in the atmosphere, such as seasonal thermospheric circulation.

The model is particularly bad at fitting images that contain the night side of the planet (top and bottom rows). In these cases the observations may be sensitive to the likely density imbalance between the day and night side of the planet, resulting from the thermospheric general circulation. A density imbalance between the hemispheres would force the model to select an intermediate value, between those actually present on the dayside and the nightside. This is particularly noticeable in the image sets gathered in late February and early March 2015, parts of which image near North polar night, the focus of hemispheric circulation and downwelling at this time of the Martian year. This circulation acts to increase the density of hydrogen in the polar night, resulting in model underprediction (green) of the densities towards the North pole.

To illustrate the inadequacy of a spherically symmetric model more clearly, enlargements of two image sets are shown in Figure 6.19. These two images illustrate the deviation between the spherically symmetric model and the data for the dawn bulge observed in apoapsis and coronal scan data, and the potential concentration of hydrogen in the Northern hemisphere winter night by thermospheric circulation.

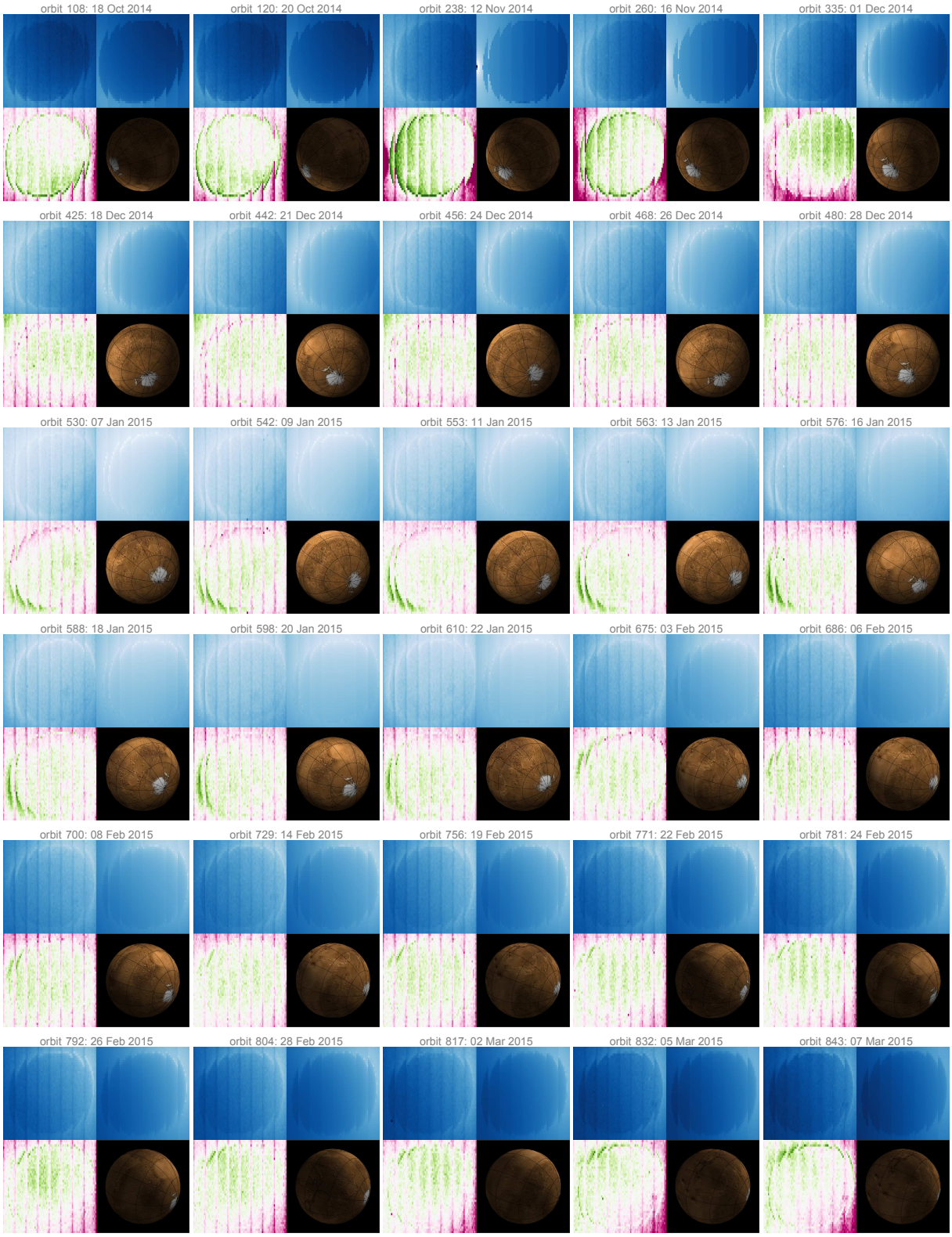

Figure 6.18: Mosaic of apoapsis image sets in the style of Figure 6.17. All data and models share the same scale.

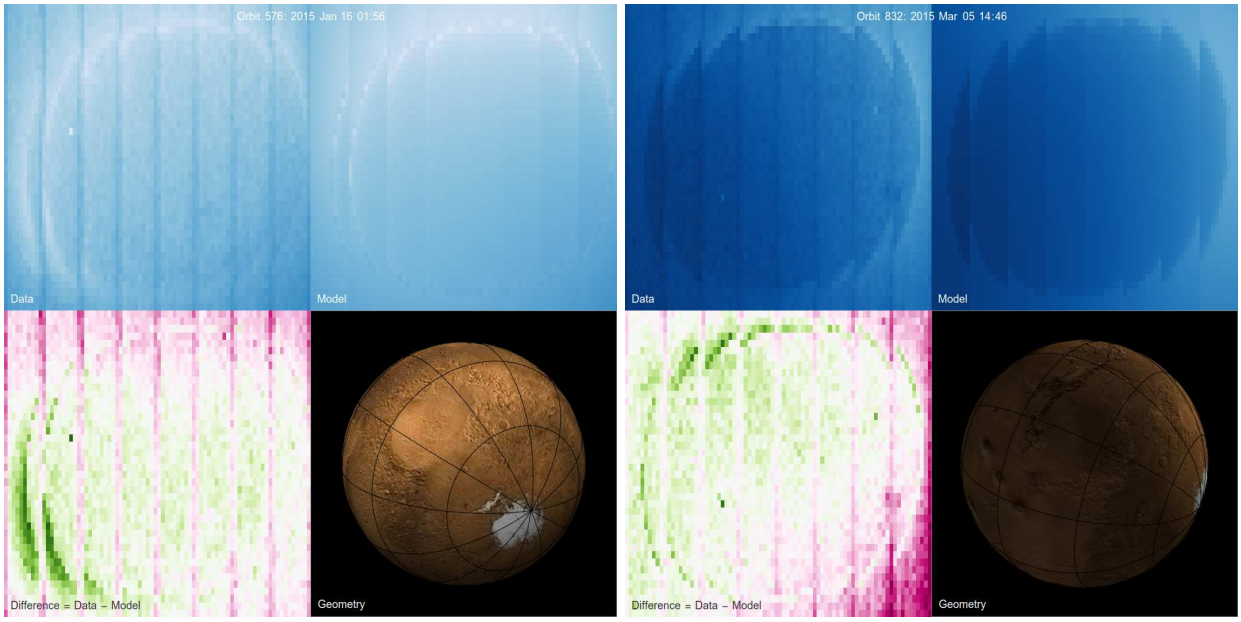

Figure 6.19: Enlarged image sets for particular orbits. (left) Illustration of dawn intensity bulge. (right) Model underprediction of Northern hemisphere nighttime densities.

6.5 Preliminary conclusions

The MAVEN data sample the Mars H corona more completely than any previous mission or observational campaign. For the first time, the high cadence and broad geographical coverage of these data enable a comprehensive overhaul of models for neutral H escape at Mars, demonstrating that a single-temperature Chamberlain exosphere model is insufficient to support the observations. Inconsistent intensities in the near and far corona observed in MAVEN's 35-hour insertion orbit, together with anomalous intensity values observed near the dawn terminator and across the nightside suggest that there are significant non-thermal and non-spherically symmetric pheonomena affecting the population of the corona and affecting the escape rate of hydrogen to space. Interestingly, these asymmetries appear different than those predicted from 3D thermosphere-exosphere simulations. While a Chamberlain model fitted to the observations produces coronal parameters and escape rates in family with previous retrievals at Mars, more sophisticated modeling tools will need to be brought to bear on the observations to interpret them correctly.

6.6 Future work

To analyze the MAVEN data properly, more sophisticated models of the physical density and potentially the radiative transfer will be required. The corona MAVEN is seeing cannot be fit by a spherically symmetric single-temperature Chamberlain model: it is therefore natural to discuss the future development of the model and what changes may be required to bring it into closer correspondence with the data.

In MAVEN's insertion orbit, the current model with one population overpredicts intensities in the inner corona but significantly underpredicts them in the outer corona, suggesting that adding an additional population at a different temperature may greatly improve the fidelity of the fit. As a first approximation, we could introduce an independent population at a different temperature and density from the bulk atmosphere, increasing the number of model parameters from two to four. This would allow for the possibility of a cold, dense corona augmented by a lower density hot

population that could enhance or dominate intensities at high altitude.

Adding a hot component to the model threatens to break the consistency of the physical model and the radiative transfer, or significantly increase the complexity of the radiative transfer model. At present, the model assumes Gaussian line shapes at a constant width everywhere in the thermosphere and exosphere. This assumption is only strictly valid in the collisional atmosphere below the exobase (assuming a constant thermospheric temperature), but gets increasingly poor as altitude increases and the coronal velocity space consistent with departure from the exobase gets increasingly small. Nevertheless, the departure from Gaussian is small even at the highest altitudes MAVEN probes, so that with a single temperature the radiative transfer can be treated with a Gaussian line shape. For a two-temperature model, a Gaussian shape at a single temperature will fit the velocity distribution poorly, particularly in the transition region where the cold population diminishes relative to the hot. With a variable line shape as a function of altitude, the Thomas model discussed in Chapter 3 cannot be used without significant modification. To account for radially-varying temperatures, the model must be extended to incorporate partial frequency redistribution. Methods for doing this in the framework of the current spherically-symmetric theory have been developed [Bush and Chakrabarti, 1995], but the degree to which they are competitive with Monte Carlo radiative transfer models is unclear, especially given the additional complications analysis of the MAVEN data is likely to require.

While intensities observed in the MAVEN insertion orbit may be better fit with two spherically symmetric exospheric populations at different temperatures, it is likely that the asymmetries in thermospheric H density observed with IUVS coronal scans and apoapsis maps could also resolve the model/data discrepancies. Most of the insertion orbit image views the night side of the planet; the inconsistency of the inner and outer corona observed may be due to transport of atoms to high altitudes from the hotter dayside.

Spherical asymmetries appear to dominate the deviations of the model from the data in the coronal scans and apoapsis images sets: these asymmetries will need to be included in the model to reproduce the observed brightness variations. Variations in temperature as a function of location

at the exobase raise the same concerns as were discussed for adding a spherically symmetric hot population above, and would require significant modification to the radiative transfer, including most likely the adoption of a Monte Carlo photon scattering code. Variations in density as a function of exobase position are simpler to accommodate from a radiative transfer perspective, but any spatially-varying exobase parameters require a more detailed treatment of the physical distribution of atoms in the corona. Some extensions to non-uniform models have been made analytically [Vidal-Madjar and Bertaux, 1972], but for complete freedom the physical model must be treated particle-by-particle in 3D, using a physical Monte Carlo model.

Outside the physical and radiative transfer model, more sophisticated methods are required to fully account for the degeneracy present in the model parameter space when fitting the model to the data. While chi-squared analysis can reveal the best-fit coronal parameters regardless of the uncertainties assumed for the data, the large chi-squared values and substantial parameter covariance present in the coronal model/data comparison indicate that a more subtle approach is required. In particular, the formal parameter uncertainties calculated using the $\Delta\chi^2 = 1$ contour cannot be trusted to reveal the actual range of model parameters consistent with the data. A better approach is to explore the model parameter space using a monte carlo approach, which does not assume the best-fit surface can be locally approximated by a parabola. This approach has the potential to explore the model parameter distribution directly, producing more robust estimates on the likelihood of the underlying parameters and their confidence region.

It is natural to ask on the basis of the MAVEN observations whether anything has been revealed that requires substantial reevaluation of the SPICAM data analysis. Especially striking is the degree to which the SPICAM data are well-fit by a spherically symmetric model, when the MAVEN data exhibit clear evidence of an aspheric corona. While IUVS has revealed the corona as three-dimensional, the SPICAM data are unlikely to profit much from reanalysis, for at least two reasons. First, the three-dimensional structure present in the corona seen by IUVS is a secondary effect, superseded by temporal effects. This is clearly seen in MAVEN's coronal scans, where 50% intensity changes due to temporal variability are present as compared to perhaps $10-15\%$ changes

in intensity due to the model assumption of spherical symmetry. Second, the SPICAM data may simply be too noisy and poorly sampled to record the spatial asymmetries observed by IUVS. In our analysis of the 2007 data, we found physically implausible that any asymmetry could account for the factor of 2 change in brightness we observed across all SPICAM viewing geometries. This too indicates that if the SPICAM data record asymmetries, these may be intelligible in retrospect, after the MAVEN data have been understood.

Exploring the space of additional parameters required by the model to obtain a satisfactory fit to the data will constitute the majority of the MAVEN data analysis. With its high-cadence and high-quality data, MAVEN's IUVS will constrain the structure of the corona and its variability more fully than ever before.

Chapter 7

Perspectives

This thesis has presented a review of the current state of knowledge of the Mars H corona, which has been studied for more than forty years. Recently, the volume of data has been greatly expanded through MAVEN IUVS observations of Mars at a higher cadence than ever before.

The work presented here on the SPICAM dataset greatly expands the range of coronal scans used to constrain the Mars atmosphere, revealing large and unexpected changes in the escape rate of hydrogen from the atmosphere of Mars. These changes in the escape rate are not predicted if molecular hydrogen serves as a long-lived buffer on the escape rate of hydrogen, suggesting that water may provide a second source of hydrogen to the upper atmosphere, enhancing escape rates.

When water can penetrate to higher altitudes, photochemical modeling predicts that it will act as a strong source of escaping hydrogen. Water layers at eighty kilometers can enhance escape rates by a factor of one hundred in several weeks, with a return to lower escape rates on the same timescale once the layer is removed. Water layers similar to those needed to enhance escape rates have been observed by SPICAM in solar occultation; the modeling work performed for this thesis therefore explains and integrates prior observations of high altitude water and enhanced hydrogen escape, providing a plausible explanation for the inflated corona observed by HST and SPICAM in 2007.

MAVEN data are constraining the seasonal behavior and three dimensional structure of the corona better than ever before. Observations with IUVS during the MAVEN insertion orbit, across the limb with coronal scans, and from apoapsis disk maps reveal that there are substantial regions

of the corona that are not well-fit by the spherically symmetric single temperature model that performed so well on SPICAM data. Work is already underway to extend the physical density model and radiative transfer to incorporate these effects and use the data to constrain 3D coronal models. Initial analysis suggests that the circulation models do not correctly predict the transport of hydrogen across the dawn terminator near the Southern summer equinox. Extending the coronal retrievals into 3D to interpret the substantial dataset provided by MAVEN will enable coronal tomography at Mars for the first time, constraining coronal structure and the present-day escape rate of hydrogen than ever before.

Understanding the corona of Mars will enable better estimates of the amount of water Mars has lost over the course of its history. Mars is unique among terrestrial planets in the solar system: unlike Earth, it has lost a large fraction of its initial water inventory, but unlike Venus, it still retains substantial inventory of water at its surface. Loss to space throughout time may have removed hundreds of meters of water from the surface of Mars: understanding how these loss rates are controlled today will enable extrapolation of present day loss rates into the past.

Beyond Mars and the planets of the solar system, loss of hydrogen to space may be a common process on planets throughout the universe, potentially controlling the longevity of habitable environments. In addition to removing water from the atmosphere, H escape provides a source of oxidizing power to planetary atmospheres and surfaces when it is unbalanced by loss of oxygen. On planets with substantial H escape, abiotic buildup of oxygen could shift the redox balance toward oxidizing environments, hindering the the development of prebiotic chemistry. Hydrogen atmospheres on planets beyond our solar system have already been detected [Vidal-Madjar et al., 2003]; the subject is no longer purely theoretical. However, the data gathered purely from exoplanetary systems is likely to always be small compared with that provided by objects in the solar system. Understanding how H escape operates at Mars provides ground truth for understanding how atmospheres operate in general: on the exotic worlds found orbiting other stars, the insights gleaned at Mars may prove essential for understanding planetary atmospheric escape and the evolution of habitable environments throughout the universe.

Bibliography

D. E. Anderson. The Mariner 5 Ultraviolet Photometer Experiment: Analysis of hydrogen Lyman alpha data. J. Geophys. Res., 81(7):1213–1216, Mar 1976. ISSN 0148-0227. doi: 10.1029/ja081i007p01213. URL http://dx.doi.org/10.1029/JA081i007p01213.

D. E. Anderson and C. W. Hord. Multidimensional radiative transfer: Applications to planetary coronae. Planetary and Space Science, 25(6):563–571, Jun 1977. ISSN 0032-0633. doi: 10.1016/0032-0633(77)90063-0. URL http://dx.doi.org/10.1016/0032-0633(77)90063-0.

D. E. Anderson, Jr. Mariner 6, 7, and 9 ultraviolet spectrometer experiment: Analysis of hydrogen Lyman alpha data. J. Geophys. Res., 79:1513–1518, 1974. doi: 10.1029/JA079i010p01513.

D. E. Anderson, Jr. and C. W. Hord. Mariner 6 and 7 ultraviolet spectrometer experiment: Analysis of hydrogen Lyman-alpha data. J. Geophys. Res., 76:6666–6673, 1971. doi: 10.1029/JA076i028p06666.

D. E. Anderson, Jr. and C. W. Hord. Correction: "Mariner 6 and 7 ultraviolet spectrometer experiment: Analysis of hydrogen Lyman-alpha data" [J. Geophys. Res., Vol. 76, p. 6666 - 6673 (1971)]. J. Geophys. Res., 77:5638, 1972. doi: 10.1029/JA077i028p05638.

S. I. Babichenko, E. V. Deregusov, V. G. Kurt, N. N. Romanova, V. A. Skliankin, A. S. Smirnov, J. J. Bertaux, and J. Blamont. Measurements in interplanetary space and in the Martian upper atmosphere with a hydrogen absorption-cell spectrophotometer for L-alpha radiation on-board Mars 4-7 spaceprobes. Space Science Instrumentation, 3:271–286, Nov. 1977.

J. Bailey and M. Gruntman. Experimental study of exospheric hydrogen atom distributions by Lyman-alpha detectors on the TWINS mission. Journal of Geophysical Research, 116(A9), 2011. ISSN 0148-0227. doi: 10.1029/2011ja016531. URL http://dx.doi.org/10.1029/2011JA016531.

C. A. Barth, C. W. Hord, J. B. Pearce, K. K. Kelly, G. P. Anderson, and A. I. Stewart. Mariner 6 and 7 ultraviolet spectrometer experiment: Upper atmosphere data. J. Geophys. Res., 76: 2213–2227, 1971. doi: 10.1029/JA076i010p02213.

C. A. Barth, A. I. Stewart, C. W. Hord, and A. L. Lane. Mariner 9 ultraviolet spectrometer experiment: Mars airglow spectroscopy and variations in Lyman alpha. Icarus, 17:457–468, Oct. 1972. doi: 10.1016/0019-1035(72)90011-5.

J. Bertaux. Interpretation of OGO-5 line shape measurements of Lyman-alpha emission from terrestrial exospheric hydrogen. Planetary and Space Science, 26(5):431–447, May 1978. ISSN 0032-0633. doi: 10.1016/0032-0633(78)90065-x. URL http://dx.doi.org/10.1016/0032-0633(78)90065-X.

J.-L. Bertaux. L'hydrogéne atomique dans l'exosphere terrestre. PhD thesis, Univ. of Paris, 1974.

J. L. Bertaux and J. E. Blamont. Interpretation of Ogo 5 Lyman alpha measurements in the upper geocorona. Journal of Geophysical Research, 78(1):80–91, Jan 1973. ISSN 0148-0227. doi: 10.1029/ja078i001p00080. URL http://dx.doi.org/10.1029/JA078i001p00080.

J.-L. Bertaux, J. Blamont, M. Marcelin, V. Kurt, N. Romanova, and A. Smirnov. Lyman-alpha observations of venera-9 and 10 I. The non-thermal hydrogen population in the exosphere of venus. Planetary and Space Science, 26(9):817–831, Sep 1978. ISSN 0032-0633. doi: 10.1016/0032-0633(78)90105-8. URL http://dx.doi.org/10.1016/0032-0633(78)90105-8.

J. L. Bertaux, E. Kyrölä, E. Quémerais, R. Pellinen, R. Lallement, W. Schmidt, M. Berthé, E. Dimarellis, J. P. Goutail, C. Taulemesse, and et al. SWAN: A study of Solar Wind Anisotropies on SOHO with Lyman alpha sky mapping. Solar Physics, 162(1-2):403–439, Dec 1995. ISSN 1573-093X. doi: 10.1007/bf00733435. URL http://dx.doi.org/10.1007/BF00733435.

J.-L. Bertaux, O. Korablev, S. Perrier, E. Quémerais, F. Montmessin, F. Leblanc, S. Lebonnois, P. Rannou, F. Lefèvre, F. Forget, A. Fedorova, E. Dimarellis, A. Reberac, D. Fonteyn, J. Y. Chaufray, and S. Guibert. SPICAM on Mars Express: Observing modes and overview of UV spectrometer data and scientific results. J. Geophys. Res., 111(E10S90):E10S90, Oct. 2006. doi: 10.1029/2006JE002690.

A. Beth, P. Garnier, D. Toublanc, I. Dandouras, and C. Mazelle. Theory for planetary exospheres: I. Radiation pressure effect on dynamical trajectories. arXiv, Feb. 2015a.

A. Beth, P. Garnier, D. Toublanc, I. Dandouras, and C. Mazelle. Theory for planetary exospheres: II. Radiation pressure effect on exospheric density profiles. arXiv, Mar. 2015b.

J. Bezanson, A. Edelman, S. Karpinski, and V. B. Shah. Julia: A Fresh Approach to Numerical Computing. ArXiv e-prints, Nov. 2014.

J.-P. Bibring, Y. Langevin, J. F. Mustard, F. Poulet, R. Arvidson, A. Gendrin, B. Gondet, N. Mangold, P. Pinet, and F. Forget. Global Mineralogical and Aqueous Mars History Derived from OMEGA/Mars Express Data. Science, 312:400–404, Apr. 2006. doi: 10.1126/Science.1122659.

S. W. Bougher, T. E. Cravens, J. Grebowsky, and J. Luhmann. The Aeronomy of Mars: Characterization by MAVEN of the Upper Atmosphere Reservoir That Regulates Volatile Escape. Space Science Reviews, Aug 2014. ISSN 1572-9672. doi: 10.1007/s11214-014-0053-7. URL http://dx.doi.org/10.1007/s11214-014-0053-7.

B. C. Bush and S. Chakrabarti. A radiative transfer model using spherical geometry and partial frequency redistribution. J. Geophys. Res., 100:19627–19642, Oct. 1995. doi: 10.1029/95JA01209.

M. H. Carr and J. W. Head. Martian surface/near-surface water inventory: Sources, sinks, and changes with time. Geophys. Res. Lett., 42(3):726–732, Feb 2015. ISSN 0094-8276. doi: 10.1002/2014gl062464. URL http://dx.doi.org/10.1002/2014GL062464.

G. R. Carruthers, T. Page, and R. R. Meier. Apollo 16 Lyman alpha imagery of the hydrogen geocorona. Journal of Geophysical Research, 81(10):1664–1672, Apr 1976. ISSN 0148-0227. doi: 10.1029/ja081i010p01664. URL http://dx.doi.org/10.1029/JA081i010p01664.

T. A. Cassidy, A. W. Merkel, M. H. Burger, M. Sarantos, R. M. Killen, W. E. McClintock, and R. J. Vervack. Mercury's seasonal sodium exosphere: Messenger orbital observations. Icarus, 248:547–559, Mar 2015. ISSN 0019-1035. doi: 10.1016/j.icarus.2014.10.037. URL http://dx.doi.org/10.1016/j.icarus.2014.10.037.

M. S. Chaffin, J.-Y. Chaufray, I. Stewart, F. Montmessin, N. M. Schneider, and J.-L. Bertaux. Unexpected variability of Martian hydrogen escape. Geophys. Res. Lett., 41(2):314–320, Jan 2014. ISSN 0094-8276. doi: 10.1002/2013gl058578. URL http://dx.doi.org/10.1002/2013GL058578.

J. W. Chamberlain. Planetary coronae and atmospheric evaporation. Plan. Sp. Sci., 11:901, Aug. 1963. doi: 10.1016/0032-0633(63)90122-3.

J.-Y. Chaufray and F. Leblanc. Radiative transfer of emission lines with non-Maxwellian velocity distribution function: Application to Mercury D2 sodium lines. Icarus, 223 (2):975–985, Apr 2013. ISSN 0019-1035. doi: 10.1016/j.icarus.2013.01.005. URL http://dx.doi.org/10.1016/j.icarus.2013.01.005.

J. Y. Chaufray, J. L. Bertaux, F. Leblanc, and E. Quémerais. Observation of the hydrogen corona with SPICAM on Mars Express. Icarus, 195:598–613, June 2008. doi: 10.1016/j.Icarus.2008.01.009.

J.-Y. Chaufray, J.-L. Bertaux, E. Quémerais, E. Villard, and F. Leblanc. Hydrogen density in the dayside venusian exosphere derived from Lyman-α observations by SPICAV on Venus Express. Icarus, 217(2):767–778, Feb 2012. ISSN 0019-1035. doi: 10.1016/j.icarus.2011.09.027. URL http://dx.doi.org/10.1016/j.icarus.2011.09.027.

J.-Y. Chaufray, F. Gonzalez-Galindo, F. Forget, M. Lopez-Valverde, F. Leblanc, R. Modolo, and S. Hess. Variability of the hydrogen in the martian upper atmosphere as simulated by a 3D atmosphere-exosphere coupling. Icarus, 245:282–294, Jan 2015. ISSN 0019-1035. doi: 10.1016/j.icarus.2014.08.038. URL http://dx.doi.org/10.1016/j.icarus.2014.08.038.

R. T. Clancy and H. Nair. Annual (perihelion-aphelion) cycles in the photochemical behavior of the global Mars atmosphere. Journal of Geophysical Research, 101(E5):12785, 1996. ISSN 0148-0227. doi: 10.1029/96je00836. URL http://dx.doi.org/10.1029/96JE00836.

J. T. Clarke, J.-L. Bertaux, J.-Y. Chaufray, G. R. Gladstone, E. Quemerais, J. K. Wilson, and D. Bhattacharyya. A rapid decrease of the hydrogen corona of Mars. Geophys. Res. Lett., 41: 8013–8020, Nov. 2014. doi: 10.1002/2014GL061803.

T. E. Cravens, T. I. Gombosi, and A. F. Nagy. Hot hydrogen in the exosphere of Venus. Nature, 283(5743):178–180, Jan 1980. ISSN 0028-0836. doi: 10.1038/283178a0. URL http://dx.doi.org/10.1038/283178a0.

V. Damian, A. Sandu, M. Damian, F. Potra, and G. R. Carmichael. The kinetic preprocessor KPP-a software environment for solving chemical kinetics. Computers & Chemical Engineering, 26(11):1567–1579, Nov 2002. ISSN 0098-1354. doi: 10.1016/s0098-1354(02)00128-x. URL http://dx.doi.org/10.1016/S0098-1354(02)00128-X.

J. Deighan. The Effect of an Ozone Layer on Ancient Mars. PhD thesis, University of Virginia, December 2012.

L. M. Delves and J. L. Mohamed. Computational Methods for Integral Equations. Cambridge University Press, 1985.

N. N. Dementyeva, V. G. Kurt, A. S. Smirnov, L. G. Titarchuk, and S. D. Chuvahin. Preliminary Results of Measurements of UV Emissions Scattered in the Martian Upper Atmosphere (A 3.5). Icarus, 17:475–483, Oct. 1972. doi: 10.1016/0019-1035(72)90013-9.

T. M. Donahue. Aeronomy of CO_2 Atmospheres: A Review. J. Atmos. Sci., 28(6):895–900, Sep 1971. ISSN 1520-0469. doi: 10.1175/1520-0469(1971)028<0895:aocaar>2.0.co;2. URL http://dx.doi.org/10.1175/1520-0469(1971)028<0895:AOCAAR>2.0.CO;2.

B. L. Ehlmann and C. S. Edwards. Mineralogy of the Martian Surface. Annu. Rev. Earth Planet. Sci., 42(1):291–315, May 2014. ISSN 1545-4495. doi: 10.1146/annurev-earth-060313-055024. URL http://dx.doi.org/10.1146/annurev-earth-060313-055024.

B. L. Ehlmann, J. F. Mustard, S. L. Murchie, F. Poulet, J. L. Bishop, A. J. Brown, W. M. Calvin, R. N. Clark, D. J. D. Marais, R. E. Milliken, and et al. Orbital Identification of Carbonate-Bearing Rocks on Mars. Science, 322(5909):1828–1832, Dec 2008. ISSN 1095-9203. doi: 10.1126/science.1164759. URL http://dx.doi.org/10.1126/science.1164759.

C. Emerich, P. Lemaire, J.-C. Vial, W. Curdt, U. Schühle, and K. Wilhelm. A new relation between the central spectral solar H I Lyman α irradiance and the line irradiance measured by SUMER/SOHO during the cycle 23. Icarus, 178:429–433, Nov. 2005. doi: 10.1016/j.Icarus.2005.05.002.

H. J. Fahr and B. Shizgal. Modern exospheric theories and their observational relevance. Reviews of Geophysics, 21(1):75, 1983. ISSN 8755-1209. doi: 10.1029/rg021i001p00075. URL http://dx.doi.org/10.1029/RG021i001p00075.

P. D. Feldman, A. J. Steffl, J. W. Parker, M. F. A'Hearn, J.-L. Bertaux, S. Alan Stern, H. A. Weaver, D. C. Slater, M. Versteeg, H. B. Throop, N. J. Cunningham, and L. M. FeAnn. Geophys.a. Rosetta -Alice observations of exospheric hydrogen and oxygen on Mars. Icarus, 214:394–399, Aug. 2011. doi: 10.1016/j.Icarus.2011.06.013.

J. M. Forbes, F. G. Lemoine, S. L. Bruinsma, M. D. Smith, and X. O. Zhang. Solar flux variability of Mars' exosphere densities and temperatures. Geophys. Res. Lett., 35(1), Jan 2008. doi: 10.1029/2007GL031904. URL http://dx.doi.org/10.1029/2007GL031904.

J. L. Fox. On the escape of oxygen and hydrogen from Mars. Geophys. Res. Lett., 20(17):1747–1750, Sep 1993. ISSN 0094-8276. doi: 10.1029/93gl01118. URL http://dx.doi.org/10.1029/93GL01118.

A. Galli, P. Wurz, H. Lammer, H. I. M. Lichtenegger, R. Lundin, S. Barabash, A. Grigoriev, M. Holmström, and H. Gunell. The Hydrogen Exospheric Density Profile Measured with ASPERA-3/NPD. Space Sci. Rev., 126:447–467, Oct. 2006. doi: 10.1007/s11214-006-9089-7.

A. Gettelman, E. J. Fetzer, A. Eldering, and F. W. Irion. The Global Distribution of Supersaturation in the Upper Troposphere from the Atmospheric Infrared Sounder. J. Climate, 19(23):6089–6103, Dec 2006. ISSN 1520-0442. doi: 10.1175/jcli3955.1. URL http://dx.doi.org/10.1175/JCLI3955.1.

R. Hartle. Density and temperature distributions in non-uniform rotating planetary exospheres with applications to earth. Planetary and Space Science, 21(12):2123–2137, Dec 1973. ISSN 0032-0633. doi: 10.1016/0032-0633(73)90187-6. URL http://dx.doi.org/10.1016/0032-0633(73)90187-6.

N. G. Heavens, M. S. Johnson, W. A. Abdou, D. M. Kass, A. KleinbÃűhl, D. J. McCleese, J. H. Shirley, and R. J. Wilson. Seasonal and diurnal variability of detached dust layers in the tropical martian atmosphere. Journal of Geophysical Research: Planets, 119(8):1748–1774, Aug 2014. ISSN 2169-9097. doi: 10.1002/2014je004619. URL http://dx.doi.org/10.1002/2014JE004619.

T. Holstein. Imprisonment of Resonance Radiation in Gases. Phys. Rev., 72:1212–1233, Dec. 1947. doi: 10.1103/PhysRev.72.1212.

C. Hord, C. Barth, and J. Pearce. Ultraviolet spectroscopy experiment for Mariner Mars 1971. Icarus, 12(1):63–77, Jan 1970. ISSN 0019-1035. doi: 10.1016/0019-1035(70)90032-1. URL http://dx.doi.org/10.1016/0019-1035(70)90032-1.

W. Huebner and J. Mukherjee. Photoionization and photodissociation rates in solar and blackbody radiation fields. Planetary and Space Science, 106:11–45, Feb 2015. ISSN 0032-0633. doi: 10.1016/j.pss.2014.11.022. URL http://dx.doi.org/10.1016/j.pss.2014.11.022.

D. M. Hunten. The Escape of Light Gases from Planetary Atmospheres. J. Atmos. Sci., 30:1481–1494, Nov. 1973. doi: 10.1175/1520-0469(1973)030<1481:TEOLGF>2.0.CO;2.

D. M. Hunten and M. B. McElroy. Production and escape of hydrogen on Mars. J. Geophys. Res., 75:5989, 1970. doi: 10.1029/JA075i031p05989.

V. V. Izmodenov, O. A. Katushkina, E. Quémerais, and M. Bzowski. Distribution of Interstellar Hydrogen Atoms in the Heliosphere and Backscattered Solar Lyman-α. In Cross-Calibration of Far UV Spectra of Solar System Objects and the Heliosphere, pages 7–65. Springer Science + Business Media, 2013. ISBN http://id.crossref.org/isbn/978-1-4614-6384-9. doi: 10.1007/978-1-4614-6384-9_2. URL http://dx.doi.org/10.1007/978-1-4614-6384-9_2.

M. Jacobson. Fundamentals of Atmospheric Modeling. Cambridge University Press, 2005. ISBN 9780521548656. URL http://books.google.com/books?id=96wWzoyKRMoC.

B. M. Jakosky. The seasonal cycle of water on Mars. Sp. Sci. Rev., 41:131–200, June 1985. doi: 10.1007/BF00241348.

B. M. Jakosky, R. P. Lin, J. M. Grebowsky, J. G. Luhmann, D. F. Mitchell, G. Beutelschies, T. Priser, M. Acuna, L. Andersson, D. Baird, and et al. The Mars Atmosphere and Volatile Evolution (MAVEN) Mission. Space Science Reviews, Apr 2015. ISSN 1572-9672. doi: 10.1007/s11214-015-0139-x. URL http://dx.doi.org/10.1007/s11214-015-0139-x.

J. Jeans. The dynamical theory of gases. University Press, Cambridge, Eng., 1925. URL http://hdl.handle.net/2027/uc1.b4523400.

V. A. Krasnopolsky. Photochemistry of the Martian atmosphere (mean conditions). Icarus, 101: 313–332, Feb. 1993. doi: 10.1006/icar.1993.1027.

V. A. Krasnopolsky. Mars' upper atmosphere and ionosphere at low, medium, and high solar activities: Implications for evolution of water. J. Geophys. Res., 107:5128, Dec. 2002. doi: 10.1029/2001JE001809.

V. A. Krasnopolsky. Photochemistry of the martian atmosphere: Seasonal, latitudinal, and diurnal variations. Icarus, 185:153–170, Nov. 2006. doi: 10.1016/j.icarus.2006.06.003.

V. A. Krasnopolsky. Solar activity variations of thermospheric temperatures on Mars and a problem of CO in the lower atmosphere. Icarus, 207(2):638–647, Jun 2010. ISSN 0019-1035. doi: 10.1016/j.icarus.2009.12.036. URL http://dx.doi.org/10.1016/j.icarus.2009.12.036.

V. A. Krasnopolsky and P. D. Feldman. Detection of Molecular Hydrogen in the Atmosphere of Mars. Science, 294:1914–1917, Nov. 2001. doi: 10.1126/Science.1065569.

J. Kupperian, E. Byram, T. Chubb, and H. Friedman. Far ultraviolet radiation in the night sky. Planetary and Space Science, 1(1):3–6, Jan 1959. ISSN 0032-0633. doi: 10.1016/0032-0633(59)90015-7. URL http://dx.doi.org/10.1016/0032-0633(59)90015-7.

R. Lallement, J. L. Bertaux, and F. Dalaudier. Interplanetary Lyman-alpha spectral profiles and intensities for both repulsive and attractive solar force fields: predicted absorption pattern by a hydrogen cell. Astron. & Astrophys., 150:21–32, Sept. 1985.

H. Lammer, H. Lichtenegger, C. Kolb, I. Ribas, E. Guinan, R. Abart, and S. Bauer. Loss of water from Mars. Icarus, 165(1):9–25, Sep 2003. ISSN 0019-1035. doi: 10.1016/s0019-1035(03)00170-2. URL http://dx.doi.org/10.1016/S0019-1035(03)00170-2.

H. Lammer, E. ChassefiÃÍre, Ã. Karatekin, A. Morschhauser, P. B. Niles, O. Mousis, P. Odert, U. V. MÃűstl, D. Breuer, V. Dehant, and et al. Outgassing History and Escape of the Martian Atmosphere and Water Inventory. Space Science Reviews, 174(1-4):113–154, Nov 2012. ISSN 1572-9672. doi: 10.1007/s11214-012-9943-8. URL http://dx.doi.org/10.1007/s11214-012-9943-8.

J. S. Levine, D. S. McDougal, D. E. Anderson, and E. S. Barker. Atomic Hydrogen on Mars: Measurements at Solar Minimum. Science, 200(4345):1048–1051, Jun 1978. ISSN 1095-9203. doi: 10.1126/science.200.4345.1048. URL http://dx.doi.org/10.1126/science.200.4345.1048.

H. I. M. Lichtenegger, H. Lammer, Y. N. Kulikov, S. Kazeminejad, G. H. Molina-Cuberos, R. Rodrigo, B. Kazeminejad, and G. Kirchengast. Effects of Low Energetic Neutral Atoms on Martian and Venusian Dayside Exospheric Temperature Estimations. Space Sci. Rev., 126:469–501, Oct. 2006. doi: 10.1007/s11214-006-9082-1.

S. Liu and T. Donahue. The regulation of hydrogen and oxygen escape from Mars. Icarus, 28(2):231–246, Jun 1976. ISSN 0019-1035. doi: 10.1016/0019-1035(76)90035-x. URL http://dx.doi.org/10.1016/0019-1035(76)90035-X.

Z. Lu, Y. C. Chang, Q.-Z. Yin, C. Y. Ng, and W. M. Jackson. Evidence for direct molecular oxygen production in CO2 photodissociation. Science, 346(6205):61–64, Oct 2014. ISSN 1095-9203. doi: 10.1126/science.1257156. URL http://dx.doi.org/10.1126/science.1257156.

M. C. Malin and K. S. Edgett. Evidence for Persistent Flow and Aqueous Sedimentation on Early Mars. Science, 302(5652):1931–1934, Dec 2003. ISSN 1095-9203. doi: 10.1126/science.1090544. URL http://dx.doi.org/10.1126/science.1090544.

L. Maltagliati, F. Montmessin, O. Korablev, A. Fedorova, F. Forget, A. MÃďÃďttÃďnen, F. LefÃÍvre, and J.-L. Bertaux. Annual survey of water vapor vertical distribution and water-aerosol coupling in the martian atmosphere observed by SPICAM/MEx solar occultations. Icarus, 223(2):942–962, Apr 2013. ISSN 0019-1035. doi: 10.1016/j.icarus.2012.12.012. URL http://dx.doi.org/10.1016/j.icarus.2012.12.012.

M. Matta, P. Withers, and M. Mendillo. The composition of Mars' topside ionosphere: Effects of hydrogen. Journal of Geophysical Research: Space Physics, 118(5):2681–2693, May 2013. ISSN 2169-9380. doi: 10.1002/jgra.50104. URL http://dx.doi.org/10.1002/jgra.50104.

W. E. McClintock, N. M. Schneider, G. M. Holsclaw, J. T. Clarke, A. C. Hoskins, I. Stewart, F. Montmessin, R. V. Yelle, and J. Deighan. The Imaging Ultraviolet Spectrograph (IUVS) for the MAVEN Mission. Space Science Reviews, Sep 2014. ISSN 1572-9672. doi: 10.1007/s11214-014-0098-7. URL http://dx.doi.org/10.1007/s11214-014-0098-7.

M. B. McElroy. Mars: An Evolving Atmosphere. Science, 175:443–445, Jan. 1972. doi: 10.1126/Science.175.4020.443.

M. B. McElroy and T. M. Donahue. Stability of the Martian Atmosphere. Science, 177:986–988, Sept. 1972. doi: 10.1126/Science.177.4053.986.

D. L. Mitchell, R. P. Lin, C. Mazelle, H. Réme, P. A. Cloutier, J. E. P. Connerney, M. H. Acuña, and N. F. Ness. Probing Mars' crustal magnetic field and ionosphere with the MGS Electron Reflectometer. J. Geophys. Res., 106(E10):23,419, Oct 2001. doi: 10.1029/2000JE001435. URL http://dx.doi.org/10.1029/2000JE001435.

V. I. Moroz. The atmosphere of Mars. Sp. Sci. Rev., 19:763–843, Dec. 1976. doi: 10.1007/BF00173706.

A. F. Nagy, J. Kim, and T. E. Cravens. Hot hydrogen and oxygen atoms in the upper atmospheres of Venus and Mars. Annales Geophysicae, 8:251–256, Apr. 1990.

H. Nair, M. Allen, A. D. Anbar, Y. L. Yung, and R. T. Clancy. A photochemical model of the martian atmosphere. Icarus, 111:124–150, Sept. 1994. doi: 10.1006/icar.1994.1137.

T. Navarro, J.-B. Madeleine, F. Forget, A. Spiga, E. Millour, F. Montmessin, and A. MÃďÃďttÃďnen. Global climate modeling of the Martian water cycle with improved microphysics and radiatively active water ice clouds. Journal of Geophysical Research: Planets, 119(7):1479–1495, Jul 2014. ISSN 2169-9097. doi: 10.1002/2013je004550. URL http://dx.doi.org/10.1002/2013JE004550.

T. D. Parkinson and D. M. Hunten. Spectroscopy and Acronomy of O_2 on Mars. J. Atmos. Sci., 29:1380–1390, Oct. 1972. doi: 10.1175/1520-0469(1972)029<1380:SAAOOO>2.0.CO;2.

W. R. Pryor, G. M. Holsclaw, W. E. McClintock, M. Snow, R. J. Vervack, G. R. Gladstone, S. A. Stern, K. D. Retherford, and P. F. Miles. Lyman-α Models for LRO LAMP from MESSENGER MASCS and SOHO SWAN Data. In Cross-Calibration of Far UV Spectra of Solar System Objects and the Heliosphere, pages 163–175. Springer Science + Business Media, 2013. ISBN http://id.crossref.org/isbn/978-1-4614-6384-9. doi: 10.1007/978-1-4614-6384-9_5. URL http://dx.doi.org/10.1007/978-1-4614-6384-9_5.

E. Quémerais, J.-L. Bertaux, R. Lallement, M. Berthé, E. Kyrola, and W. Schmidt. Interplanetary Lyman α line profiles derived from SWAN/SOHO hydrogen cell measurements: Full-sky Velocity Field. Journal of Geophysical Research, 104(A6):12585, 1999. ISSN 0148-0227. doi: 10.1029/1998ja900101. URL http://dx.doi.org/10.1029/1998JA900101.

E. Quémerais, B. R. Sandel, V. V. Izmodenov, and G. R. Gladstone. Thirty Years of Interplanetary Background Data: A Global View. In Cross-Calibration of Far UV Spectra of Solar System Objects and the Heliosphere, pages 141–162. Springer Science + Business Media, 2013. ISBN http://id.crossref.org/isbn/978-1-4614-6384-9. doi: 10.1007/978-1-4614-6384-9_4. URL http://dx.doi.org/10.1007/978-1-4614-6384-9_4.

G. J. Rottman, T. N. Woods, and W. McClintock. SORCE solar UV irradiance results. Adv. Space Res., 37:201–208, 2006. doi: 10.1016/j.asr.2005.02.072.

S. P. Sander, R. R. Friedl, D. Golden, M. J. Kurylo, G. Moortgat, H. Keller-Rudek, P. Wine, A. R. Ravishankara, C. Kolb, M. J. Molina, B. Finlayson-Pitts, R. E. Huie, and V. L. Orkin. Chemical Kinetics and Photochemical Data for Use in Atmospheric Studies, Evaluation Number 17. Technical report, JPL, 2011.

B. D. Shizgal and G. G. Arkos. Nonthermal escape of the atmospheres of Venus, Earth, and Mars. Reviews of Geophysics, 34(4):483, 1996. ISSN 8755-1209. doi: 10.1029/96rg02213. URL http://dx.doi.org/10.1029/96RG02213.

A. A. Siddiqi and R. Launius. Deep space chronicle: A chronology of deep space and planetary probes 1958-2000. Monographs in Aerospace History, 24, 2002. NASA SP-2002-4524.

M. D. Smith. THEMIS observations of mars aerosol optical depth from 2002-2008. Icarus, 202(2):444–452, Aug 2009. doi: 10.1016/j.Icarus.2009.03.027. URL http://dx.doi.org/10.1016/j.Icarus.2009.03.027.

M. Snow, A. Reberac, E. Quémerais, J. Clarke, W. E. McClintock, and T. N. Woods. A new catalog of ultraviolet stellar spectra for calibration. Cross-Calibration of Far UV Spectra of Solar System Objects and the Heliosphere, pages 191–226, 2013. doi: 10.1007/978-1-4614-6384-9_7. URL http://dx.doi.org/10.1007/978-1-4614-6384-9_7.

A. Spiga, J. Faure, J.-B. Madeleine, A. Maattanen, and F. Forget. Rocket dust storms and detached dust layers in the Martian atmosphere. Journal of Geophysical Research: Planets, 118(4):746–767, Apr 2013. ISSN 2169-9097. doi: 10.1002/jgre.20046. URL http://dx.doi.org/10.1002/jgre.20046.

P. Takacs, A. Broadfoot, G. Smith, and S. Kumar. Mariner 10 observations of hydrogen Lyman alpha emission from the venus exosphere: Evidence of complex structure. Planetary and Space Science, 28(7):687–701, Jul 1980. ISSN 0032-0633. doi: 10.1016/0032-0633(80)90114-2. URL http://dx.doi.org/10.1016/0032-0633(80)90114-2.

G. E. Thomas. Lyman α Scattering in the Earth's Hydrogen Geocorona, 1. J. Geophys. Res., 68: 2639–2660, May 1963. doi: 10.1029/JZ068i009p02639.

UVIS Team. Cassini UVIS User's Guide. Laboratory for Atmospheric and Space Physics (LASP), 1234 Innovation Drive Boulder, CO 80301, 2nd edition, March 2014.

A. Valeille, V. Tenishev, S. W. Bougher, M. R. Combi, and A. F. Nagy. Three-dimensional study of Mars upper thermosphere/ionosphere and hot oxygen corona: 1. general description and results at equinox for solar low conditions. J. Geophys. Res., 114(E11), Nov 2009. doi: 10.1029/2009JE003388. URL http://dx.doi.org/10.1029/2009JE003388.

A. Vidal-Madjar and J. Bertaux. A calculated hydrogen distribution in the exosphere. Planetary and Space Science, 20(8):1147–1162, Aug 1972. ISSN 0032-0633. doi: 10.1016/0032-0633(72)90004-9. URL http://dx.doi.org/10.1016/0032-0633(72)90004-9.

A. Vidal-Madjar, A. Lecavelier des Etangs, J.-M. Désert, G. E. Ballester, R. Ferlet, G. Hébrard, and M. Mayor. An extended upper atmosphere around the extrasolar planet HD209458b. Nature, 422:143–146, Mar. 2003. doi: 10.1038/nature01448.

G. L. Villanueva, M. J. Mumma, R. E. Novak, H. U. Kaufl, P. Hartogh, T. Encrenaz, A. Tokunaga, A. Khayat, and M. D. Smith. Strong water isotopic anomalies in the martian atmosphere: Probing current and ancient reservoirs. Science, 348(6231):218–221, Mar 2015. ISSN 1095-9203. doi: 10.1126/science.aaa3630. URL http://dx.doi.org/10.1126/science.aaa3630.

A. N. Volkov, R. E. Johnson, O. J. Tucker, and J. T. Erwin. Thermally driven atmospheric escape: transition from hydrodynamic to Jeans escape. The Astrophysical Journal, 729(2):L24, Feb 2011. ISSN 2041-8213. doi: 10.1088/2041-8205/729/2/l24. URL http://dx.doi.org/10.1088/2041-8205/729/2/L24.

E. W. Washburn. The Vapor Pressure of Ice and of Water Below the Freezing Point. Monthly Weather Review, 52:488, 1924. doi: 10.1175/1520-0493(1924)52<488:TVPOIA>2.0.CO;2.

T. N. Woods. Solar EUV experiment (SEE): Mission overview and first results. J. Geophys. Res., 110(A1), 2005. doi: 10.1029/2004JA010765. URL http://dx.doi.org/10.1029/2004JA010765.

T. N. Woods, P. C. Chamberlin, J. W. Harder, R. A. Hock, M. Snow, F. G. Eparvier, J. Fontenla, W. E. McClintock, and E. C. Richard. Solar Irradiance Reference Spectra (SIRS) for the 2008 Whole Heliosphere Interval (WHI). Geophys. Res. Lett., 36(1), 2009. ISSN 0094-8276. doi: 10.1029/2008gl036373. URL http://dx.doi.org/10.1029/2008GL036373.

Y. L. Yung and W. B. DeMore. Photochemistry of Planetary Atmospheres. Oxford University Press, USA, 1998. ISBN 9780195344509. URL http://books.google.com/books?id=Q4pHLv9TvksC.

Y. L. Yung, J.-S. Wen, J. I. Moses, B. M. Landry, M. Allen, and K.-J. Hsu. Hydrogen and deuterium loss from the terrestrial atmosphere: A quantitative assessment of nonthermal escape fluxes. Journal of Geophysical Research, 94(D12):14971, 1989. ISSN 0148-0227. doi: 10.1029/jd094id12p14971. URL http://dx.doi.org/10.1029/JD094iD12p14971.

K. Zahnle, R. M. Haberle, D. C. Catling, and J. F. Kasting. Photochemical instability of the ancient Martian atmosphere. Journal of Geophysical Research (Planets), 113(E12):E11004, Nov. 2008. doi: 10.1029/2008JE003160.

J. H. Zoennchen, U. Nass, and H. J. Fahr. Exospheric hydrogen density distributions for equinox and summer solstice observed with TWINS1/2 during solar minimum. Ann. Geophys., 31(3):513–527, 2013. ISSN 1432-0576. doi: 10.5194/angeo-31-513-2013. URL http://dx.doi.org/10.5194/angeo-31-513-2013.

R. W. Zurek, J. R. Barnes, R. M. Haberle, J. B. Pollack, J. E. Tillman, and C. B. Leovy. Dynamics of the atmosphere of Mars. In Mars, pages 835–933. University of Arizona Press, 1992.